The Kuiper belt size distribution: constraints on accretion

by

Wesley Christopher Fraser

BSc, McMaster University, 2004

A Dissertation Submitted in Partial Fulfillment of the
Requirements for the Degree of

Doctor of Philosophy

in the Department of Physics and Astronomy

University of Victoria

Supervisory Committee

Dr. JJ Kavelaars, Supervisor

(Dept. of Physics and Astronomy, University of Victoria)

Dr. Chris Pritchet, Member

(Dept. of Physics and Astronomy, University of Victoria)

Dr. Doug Johnstone, Member

(Dept. of Physics and Astronomy, University of Victoria)

Dr. Florin Diacu, Member

(Dept. of Mathematics, University of Victoria)

Dr. David Trilling, Outside Member (Steward Observatory)

Supervisory Committee

Dr. JJ Kavelaars, Supervisor

(Dept. of Physics and Astronomy, University of Victoria)

Dr. Chris Pritchet, Member

(Dept. of Physics and Astronomy, University of Victoria)

Dr. Doug Johnstone, Member

(Dept. of Physics and Astronomy, University of Victoria)

Dr. Florin Diacu, Member

(Dept. of Mathematics, University of Victoria)

Dr. David Trilling, Outside Member (Steward Observatory)

Abstract

The Kuiper belt is a population of planetesimals outside the orbit of Neptune. The high inclinations and eccentricities exhibited by many belt members, and its very low mass ($M \lesssim 0.1 M_{\oplus}$) present an enigma to planetesimal accretion scenarios: the high relative encounter velocities ($v_{rel} \sim 1$ km s^{-1}), and infrequent collisions of the largest members make the growth of Pluto-sized bodies impossible over the age of the Solar system. Accretion in the early stages of planet-building must have been in a more dense environment allowing large objects to grow before growth was halted.

The current Kuiper belt population is the left-over relic of accretion, which has undergone collisional re-shaping since the epoch of accretion. The shape of the size distribution can provide constraint on the accretion timescale, the primordial Kuiper belt mass, and the collisional processing the belt has undergone. Thus, a measure of the size distribution provides one of the primary constraint on models which attempt to explain the formation of the Kuiper belt.

We have performed a large-scale ecliptic Kuiper belt survey, with an aerial coverage of 3.3 square degrees to a limiting magnitude $m(R) \sim 27$. From these observations, we have discovered more than 100 new Kuiper belt objects. Using this survey we have provided the best measurement of the Kuiper belt luminosity function to-date, from which we have inferred the size distribution. We have found that the size distribution is well described by a power-law for large objects with a steep slope $q_1 = 4.8$, that breaks, or rolls over to a shallower power-law with slope $q_2 = 2$ at object diameter ~ 60 km. The steep large object slope is indicative of a short accretion phase, lasting no more than a few 100 Myr. The large break diameter demonstrates that the Kuiper belt has undergone substantial collisional processing.

We have developed a collisional evolution model which we have used to study the effects of planetesimal bombardment and disruption on the size distribution. We have found that, in the current Kuiper belt, little to no evolution is occurring, or has occurred for the observable Kuiper belt. We conclude that the large break diameter cannot be produced in the current environment over the age of the Solar system. A period of intense collisional evolution in a much more dense, and hence, more massive belt is required. These findings are consistent with accretion models; the typical finding is that growth of the largest Kuiper belt objects over the age of the Solar system requires a much more massive belt than currently observed. These results point to a history in which an initially much more massive Kuiper belt underwent a short period of quiescent accretion producing Pluto size bodies.

Some event then occurred, which dynamically excited the planetesimals, producing an erosive environment which effectively halted planet growth and rapidly depleted the majority of the primordial mass. The remnant of this depletion is the Kuiper belt we observe today.

Table of Contents

List of Tables

List of Figures

Acknowledgements

There are many people I need to thank. The person who I give the highest recognition is my wife, Samantha. She has been with me from the first day of this project. With the love she has always shown me, Sam got me through to the end. With concern and the patience that makes a saint look like a pestilent child, she put up with bad moods, snappy remarks, and moments of insanity. She has been my relief when stressed, my humor when angry, and my steam when all I wanted to do was quit. Countless times, Sam has put me back on track, and helped me think through situations that perplexed me beyond anything in the sky. She made me laugh at myself. Most importantly though, Sam, like no other, possessed the ability to turn my mind away from my work, and point out to me everything else important, fun, and beautiful in life. For that I am ever grateful.

The second person I need to thank, is of course, my supervisor. The man who single-handedly taught me how to write, JJ has been as much a friend and colleague, as a boss and mentor. JJ always let me try and work things out on my own, and only nudged me in the right direction when I was perilously close to the edge of disaster. More than once, he has put up with my moments of stupidity, and always pointed them out with a witty jab. His startling ability to immediately see the correct answer to any problem, made it very easy to get things done, and his constant smile made it very easy to work for him. I owe him a great many thanks for showing me the exciting world of planetary sciences, for dragging me out to beautiful and tepid Victoria, for paying my travel all over the world, and for removing the burning toaster before I set off the observatory's fire-alarm, three times.

I must also thank my family. To my mother, Patricia LePrieur, goes the thanks

of being the firm voice I needed when all I wanted to do was wimp out, and the gratification she gave me when I heard the pride in her voice about my accomplishments. You made me feel special about what I do. I must thank my father Mike Fraser for being the voice of reality. He has always had the ability to talk about things in a way a dumb astrophysicist can understand. He always told me, "You'll get it done!" as his way of reminding me to just chill out. Thanks for helping me make some of the most important decisions I have had to make. To my step parents Bernie, and Tania, you two have been an unexpected, and fortunate part of my support and family over the years.

To my sisters I owe thanks for bringing many smiles to my face. You could never know just how good it made me feel every time I heard "My Brother's an Astrophysicist". Thanks for helping me keep my head on by pointing out how much of an idiot I can be sometimes. Believe me, I have needed it!

A very special thanks goes to my Grandma, Marion Newman. It was your christmas gift, that spurred my love for the night sky. Your newspaper articles on astronomy, and your interest in the things I have studied have been a great inspiration for my research. I only hope you know how much you are responsible for my success both in academia, and in life.

To my friends and groom's men, Nick, Lenny, Craig, Dave, and Paul, thanks for asking so many questions about astronomy. It has always been a great driving force for me to realize that people outside of astronomy are as interested in it as you are.

To Chris Pritchet, thanks for putting up with my questions. You have been an indispensable guiding help in getting through the un-written and confusing rules of the Ph.D. studies. To Doug Johnstone, you always have had a knack for keeping the fire under my ass hot as hell.

Lastly, to all of my friends in the grad department, thanks for putting up with my rants, curses, chest drumming, loud music, whistling, and the many interruptions

in the work day to put up with my senseless babbling. I have you all to thank for helping me get through problems at the school, and in my research. It has been my pleasure to share the same hallways with you, and I hope to do it again some time soon! With out further ado, thank you Chris Bildfell, Kaushi Bandara, Crystal Brasseur, Ashley Chutter, James Clem, Rachel Friensen, Jon Geehan, Aida Ghazvini, Lisa Glass. Melissa Graham, Eric Hsiao, Anudeep Kanwar, Helen Kirk, Ryan Leeman, Aaron Ludlow, Nikola Milutinovic, Rahul Mittal, Ronald Oussoren, Alex Parker, Greg Poole, Sarah Sadavoy, Jeff Stoesz, Karun Thanjavur, Lanlan Tian, Sheona Urquhart, and Brian York.

I dedicate this to my Grandmother Marion...

Chapter 1

Introduction

1.1 The Edgeworth-Kuiper belt: A Primer

The Edgeworth-Kuiper belt, or more commonly, the Kuiper belt, is a population of icy asteroids, or planetesimals in the outer Solar system, with the majority occupying space beyond the orbit of Neptune (semi-major axis $a_N = 30.1$ AU). The first observed member of this population, Pluto, was discovered in 1930, though it was recognized as a planet (*Tombaugh* 1946). The realization that Pluto was a member of a much larger swarm of planetesimals was made when the second known Kuiper belt object, 1992 QB1 was discovered, more than 60 years later (*Jewitt and Luu* 1993). To date there have been more than 1000 Kuiper belt objects (KBOs) discovered (*Bernstein* 2008), revealing the immensity of this population.

Observations have revealed that KBOs are on a variety of orbits from circular, low inclination orbits, to orbits which are highly inclined and eccentric. KBOs have been divided into distinct dynamical groups based on their individual orbital types. The KBOs closest to the Sun are commonly referred to as Centaurs. Adopting the recent classification scheme of Gladman (*Gladman et al.* 2008), Centaurs are objects which exist near the interior "edge" of the Kuiper belt, and are classified as those objects with $a < a_N$. Additionally, to avoid overlap with the parameter space of Jupiter family comets, Centaurs must also have Jupiter-Tisserand parameters, $T_J > 3.05$, and perihelion distances, $q < 7.35$ AU. Thus, Centaurs are objects interior to the orbit of Neptune, who are not strongly scattering off Jupiter.

KBOs who's orbital periods are commensurate with Neptune's and are therefore in mean-motion resonances (MMRs) with the gas-giant, are referred to as resonators. Most resonators are found in low-order resonances (1:1, 1:2, 2:3, etc.), but populations in higher order resonances have been found (*Kavelaars et al.* 2008). Resonators typically have dynamically excited orbits with large eccentricities ($\bar{e} \sim 0.2$ for the 2:3 population).

The scattering population, or scattered-disk population, are those objects who are experiencing large orbital perturbations through gravitational interactions with Neptune, and exist on orbits exterior to Neptune. The detached population, are those objects with large eccentricities, $e > 0.24$ and semi-major axes, $a < 2000$ AU, and are currently not experiencing interactions with Neptune.

The "classical-belt", who's name has arisen from its resemblance to the type of orbits KBOs were initially predicted to have, are non-resonant KBOs with low eccentricities. The inclination distribution of this population has been demonstrated to be bi-modal, with the two components well described as guassians with mean zero and widths of $i \sim 5^o$ (the cold population) and $i \sim 20^o$ (the hot population) (*Brown* 2001). Classical belt objects have a range of eccentricities, with a mean of $e \sim 0.07$ (*Morbidelli et al.* 2008). The population is approximately bounded by the 2:3 ($a = 39.4$ AU) and 1:2 ($a = 47.7$ AU) MMRs with Neptune, and exhibits a sharp decrease in population outside these limits.

The orbital distribution of the Kuiper belt contains a dynamical structure with properties that cannot be accounted for if KBOs under-went quiescent accretion from a Keplerian disk. For example, the large population of resonant objects cannot be explained if Neptune and the Kuiper belt formed in their current locations. Additionally, the large drop in density of KBOs coincident with the 1:2 MMR with Neptune, or the current large relative KBO velocities, of ~ 1 km/s (*Dell'Oro et al.* 2001), are not explained by in-situ formation (*Stern* 1996, *Kenyon and Bromley* 2001). Some past dynamical event(s) must have excited and sculpted the Kuiper belt orbital distribution.

Estimates of Kuiper belt mass range from 0.01 $M_\oplus$ to 0.1 $M_\oplus$ (*Gladman et al.* 2001, *Bernstein et al.* 2004, *Fuentes and Holman* 2008) which is $\sim 1-2$ orders of magnitude smaller than that predicted for the minimum-mass Solar nebula (MMSN) at the distance of the Kuiper belt (*Hayashi* 1981). Accretion models suggest that the primordial Kuiper belt must have been $\sim 2-3$ orders of magnitude larger than currently observed for the largest known objects - Pluto and Eris with $D \sim 2000$km (*Stern et al.* 1997, *Brown et al.* 2006) - to have accreted over the age of the Solar system (see *Kenyon* 2002, for a review of accretion in the Kuiper belt region). Simulations of the current Kuiper belt predict that object growth in the Kuiper belt is no-longer occurring; the large relative velocities cause encounters (collisions) of smaller objects to be disruptive, and encounter lifetimes for the largest objects are of order the age of the Solar system (*Dell'Oro et al.* 2001). Some process has depleted the Kuiper belt mass, and raised relative velocities high enough to effectively halt accretion at a point in the history of the Solar system.

The current state of the Kuiper belt hints at a virulent and dynamic history in which accretion occurred for a short period of time before a large scale orbital excitation (or series of orbital excitations) and mass depletion event dramatically changed the primordial belt. *Stern* (1995) and *Dell'Oro et al.* (2001) have found that the current collision timescales between large, $D \gtrsim 100$ km KBOs are of order the age of the Solar system, thus demonstrating that little collisional evolution has occurred for the Kuiper belt in its current state. This suggests that large KBOs are primordial - they have not been collisionally evolved since the end of accretion - and the current population presents a snap-shot and the end-state of the evolutionary processes that occurred in the early Solar system.

The purpose of this thesis is to measure the size distribution of the Kuiper belt, and as the end-state of processing in the Kuiper belt, constrain the accretionary and collisional processes, as well as the dynamical events responsible for producing the Kuiper belt we see today.

1.2 Accretion in the Outer Solar System: What do we expect?

The modern technique used in accretion modeling of planetesimal growth was introduced by *Safronov and Zvjagina* (1969). In this formalism, particles are distributed in discrete mass and semi-major axis bins, and have a distribution of horizontal and vertical velocities centered on the Keplerian velocity for that semi-major axis bin. Interactions or collisions between particles are calculated on a cross-sectional basis, and the results are determined from the impact kinetic energy - accretion, cratering, or target shattering and dispersal can occur. As objects grow, or shrink, the size distribution evolves with time. The results depend on various model parameters, such as the range of relative velocities, target strengths, and the total mass of planetesimals.

Using this technique, *Stern* (1995) presented a ground-breaking simulation of accretion in the Kuiper belt region. In these simulations, the initial Kuiper belt is assigned power-law density distributions in both semi-major axis and size. That is, the number of objects with heliocentric distance r to $r + dr$ and diameter D to $D + dD$ is $dN(r, D) = D^{-q}r^{-c}dDdr$ where q and c are logarithmic slopes. The planetesimals are assigned a typical orbital eccentricity which is set for the duration of the simulations. They found that, for conditions similar to the observed Kuiper belt, ie. relatively high eccentricity, and low belt mass, objects as large as Pluto could not form in the age of the Solar system, as collisions in the current belt are too infrequent, and typically erosive for all but the most massive objects. For $D > 1000$

km objects to have formed, lower eccentricities *and* a belt with mass 10-50 $M_\oplus$, or several times the MMSN value in the Kuiper belt range are required.

Continuing from his earlier work, *Stern* (1996) presented a set of simulations in which he evaluated the evolution of a massive $10 - 50$ $\mathrm{M}_\oplus$ primordial Kuiper belt. They found that objects would grow from ~ 1 km seeds to as large as ~ 1000 km planetesimals - the diameters of the largest KBOs - in $\sim 10^8$ years, ie. on timescales much shorter than the age of the Solar system, $\sim 4.5 \times 10^9$ yr. They inferred that, at this stage in the evolution, eccentricities must have been increased relatively suddenly by gravitational stirring from Neptune, or viscous interactions in the disk, to halt growth to even larger objects.

One weakness with the simulations by *Stern* (1995) and *Stern* (1996) is the absence of velocity evolution during the evolution. They set the velocity distribution as constant throughout the calculations. It is unreasonable to expect that processes such as dynamical friction, viscous stirring by the largest bodies, and collisional damping would not alter the velocity distribution in both a time and size dependent basis. They address this in *Stern and Colwell* (1997a) where they present a simulation in which a prescription for gravitational friction is assigned to the largest objects that exist at any given time in the simulations. In this way, relative planetesimal velocities remain sufficiently low to promote accretion for a short period of time before being lifted to higher values. In addition, they also consider the effects of object strength - resistance to disruption by collision - on the growth of planetesimals.

The growth of objects in these simulations created a size distribution of large $D > 100$ km objects that is well represented by a power-law with slope, $q \sim 5 - 6$. The size distribution exhibits a roll-over to a nearly constant distribution with size for objects $1 \lesssim D \lesssim 100$ km, and turns back up to a slope $q \sim 3$ for objects $D < 1$ km.

Kenyon and Luu (1998), *Kenyon and Bromley* (2001), *Kenyon* (2002) present a series of simulations using the same technique introduced by *Safronov and Zvjagina* (1969), but calculate and include velocity evolution by gas-drag, viscous stirring, dynamical friction, and collisional damping. From these simulations, a self-consistent picture of the accretion and and an understanding of the size distribution evolution in the Kuiper belt region has developed. In early times, relative velocities remain low, and random collisions between objects result in orderly growth at approximately a constant rate with time. The result is a steep power-law ($q > 6$) size distribution for the largest objects that gradually flattens (reaching $q \sim 3$ on timescales similar to the age of the Solar system) as large objects become more numerous. Also, as objects grow, gravitational focusing becomes important. When the largest objects attain sizes ~ 1000 km, run-away growth occurs. This process can produce Pluto-sized objects in $\sim 100 - 150$ Myr for an initially massive Kuiper belt.

Once objects have attained radii of ~ 100 km, dynamical stirring becomes important, and relative velocities of small planetesimals start to increase. When velocities become large enough such that typical impact energies are sufficient to shatter colliding bodies, collisions between all but the largest planetesimals become erosive. The result is, that below a certain diameter (typically ~ 1 km), objects are rapidly disrupted. This produces a break in the steep power-law size distribution exhibited by the largest ($D \gtrsim 100$ km) objects. At this break size, the slope becomes much shallower ($q \sim 0$). This is the same break or roll-over produced in the simulations from *Stern and Colwell* (1997a). The so-called break diameter - the size at which the turn-over occurs - grows as collisional evolution continues, and is a strong function of the velocity evolution. *Kenyon and Bromley* (2004) performed a set of simulations in which gravitational stirring by Neptune was included. They found that break diameters as large as ~ 50 km could be created for weak objects over the age of the Solar system.

As found by *Stern and Colwell* (1997a) and confirmed by *Kenyon and Bromley*

(2001), *Kenyon* (2002), *Kenyon and Bromley* (2004), at some smaller size, $\sim 10^{-2} - 10^{-1}$ km, the size distribution turns up again. This occurs when the number of disruptive collisions becomes comparable to the fragment production from disruptions of larger objects. This condition is referred to as a collisional cascade, and the slope of the size distribution turns up again when this condition is met. In this quasi-equilibrium state, the slope of the size distribution remains constant with time. Using simple cross-sectional arguments, *Dohnanyi* (1969) demonstrated that a collisional cascade produces a size distribution slope, $q_{cc} = 3.5$. *O'Brien and Greenberg* (2003) demonstrated that the slope is actually a function of how object strength varies with size. They found that the cascade slope is shallower than $q_{cc} = 3.5$ for gravitationally dominated objects ($D \gtrsim 1$ km).

The dynamics of small bodies are dominated by radiation effects, such that these objects are "blown" out of the Kuiper belt region by radiation pressure. The combination of collisional disruption and radiation pressure causes a mass-loss of material for objects $r \lesssim 1$ cm.

To summarize, these results demonstrate that

- The large object size distribution should be a power-law with slope $q \gtrsim 3$. The slope, as well as the largest object size depends on the length of time collisions resulted in accretion in the Kuiper belt region. Steep slopes are indicative of a short accretion time.

- The size distribution should break to a shallower slope for objects smaller than a break diameter, which is determined by the length of time collisions are erosive in the Kuiper belt region and the strength of KBOs.

- The size distribution will reach a state of collisional equilibrium at some smaller size with slope $q \lesssim 3.5$.

The simulations of *Stern and Colwell* (1997a,b), *Kenyon and Bromley* (2001), *Kenyon* (2002), *Kenyon and Bromley* (2004) show that even when velocity evolution is included in the simulations, for objects as large as Pluto to grow over the age of the Solar system requires (i) a massive initial Kuiper belt, (ii) 'strong' KBOs - weak, or easily disrupted material such as loosely bound rubble piles would be collisionally disrupted too rapidly stunting planetesimal growth too early, and (iii) low eccentricity for the first few 10^6 Myr. The typical eccentricity must have been lifted to much higher values to collisionally disrupt objects, and remove sufficient mass from the belt such that accretion no longer occurred.

1.3 The Kuiper belt Size Distribution: What do we already know?

Determining the sizes of objects in the Kuiper belt is all but impossible for most KBOs; only the largest and closest KBOs can be resolved by current telescope facilities, and indirect size measurements from radiometric observations have successfully only observed a few KBOs (*Stansberry et al.* 2007). Additionally, KBO diameters inferred from apparent brightnesses are uncertain because (i) albedos of KBOs are uncertain - observations have demonstrated values as low as 4% and as high as 90% (*Stansberry et al.* 2007), (ii) distances of KBOs measured from surveys with the goal of determining the size distribution are often uncertain to 10% or more. The combination of these uncertainties produces diameter measurements uncertain by as much as the size estimate itself.

A reasonable measurement of the size distribution can be made however, if one assumes that KBOs have similar albedos, and that the size distribution is the same at all distances in the Kuiper belt. We demonstrate in Chapter 2 that, under these assumptions, if the size distribution can be represented as a power-law with slope q, then the luminosity function can be represented by $\Sigma(m) = \alpha \ln(10) 10^{\alpha(m-m_o)}$, where Σ is the number of objects per square degree with magnitude m (inverse logarithmic flux measurement). In this representation, α is the logarithmic slope of the luminosity function and is related to the size distribution slope by, $q = 5\alpha + 1$, and m_o is the magnitude at which the sky density of KBOs is one object per square degree (*Gladman et al.* 2001). Thus, by measuring the slope of the luminosity function, one also infers the slope of the size distribution. In Chapter 2, we discuss the validity of the assumptions made when linking the luminosity function to the size distribution in this way, as well as some of the pitfalls that might occur if some of these assumptions are invalid. We demonstrate that if KBO albedos are dependent on size, then the slope inferred under the assumption that they are independent with size is not the real slope. The likely result is that the slope is slightly steeper than what we have observed. Note: a description of the magnitude system used by astronomers is presented in Appendix A for the reader unfamiliar with this strange flux measure.

The first measurement of the Kuiper belt luminosity function was presented by *Jewitt et al.* (1998). From this large area survey, 13 new objects were discovered with magnitude $m(R) < 22.5$, and exhibited a luminosity function slope, $\alpha = 0.58 \pm 0.05$. A narrow and much deeper survey was presented by *Gladman et al.* (1998). Using a robust maximum likelihood fitting technique, they found a best-fit $\alpha = 0.76 \pm 0.1$ for objects with $m(R) \lesssim 25.9$.

These early surveys demonstrated a surprising result, namely that the Kuiper belt luminosity function has a steep slope $\alpha \sim 0.6 - 0.8$ demonstrating that the size distribution has a large object slope $q \sim 4 - 5$. This implies that, at least for the largest objects, the Kuiper belt did not achieve a state of collisional equilibrium, which has a slope $q_{cc} \lesssim 3.5$. Later surveys from which the luminosity function could be reliably measured confirmed these results, ie. the luminosity function of KBOs in the range $20 \lesssim m(R) \lesssim 26$ is steep, implying a steep size distribution inconsistent with a size distribution in a state of collisional equilibrium (*Gladman et al.* 2001, *Trujillo et al.* 2001, *Petit et al.* 2006).

Bernstein et al. (2004) presented a deep survey to a limiting magnitude $m(R) \sim 28.5$ (*Bernstein et al.* 2006) and found more than an order of magnitude fewer detections than expected from an extrapolation of the steep bright object luminosity function to fainter magnitudes. They concluded that the luminosity function must roll-over at $m(R) \sim 25$ suggesting that the size distribution has a break at $D \sim 50 - 100$ km assuming the roll-over in the luminosity function is caused by a break in the size distribution. This result was surprising, as the inferred break diameter is much larger than that expected from accretion simulations. The results of *Bernstein et al.* (2004) warranted a repeated measurement.

1.4 Thesis Objectives

Knowledge of the size distribution of the Kuiper belt can be used to constrain accretion timescales in the outer Solar system, and provide information on the physical properties of those bodies. Previous measurements have demonstrated that the Kuiper belt has not achieved a state of collisional equilibrium, and that the luminosity function must break at some magnitude to a shallower slope. The questions that have arisen from these works are

- What is the actual large object size distribution slope?
- Is the dirth of faint objects observed by *Bernstein et al.* (2004) real? If so, at what magnitude is the luminosity function no longer consistent with a single power-law?
- Is the observed luminosity function consistent with an underlying size distribution that has a shape predicted from accretion simulations?

The goal of this thesis is to address these questions by measuring the size distribution more accurately and reliably than previously done, and from this, constrain the timescales of accretion and collisional processing in the Kuiper belt. Below we summarize the research we present in the next four chapters, which makes up the body of the research for this thesis.

1.4.1 The Bright KBO Luminosity Function presented in Chapter 2

The break in the luminosity function detected by *Bernstein et al.* (2004) suggested that a deviation from the bright object power-law could be seen at $m(R) \gtrsim 25$. To look for this break, and to more accurately measure the large object slope, we performed a survey of the Kuiper belt which we presented in *Fraser et al.* (2008). Our search method utilized a shift-and-add image search technique (*Gladman et al.* 1998) where motions of moving objects were removed from telescope images by spatially shifting consecutive images of a given field. We improved the search technique by utilizing image subtraction, and created a new image display technique which drastically improved the rate at which data was searched. Using this improved technique, we visually searched 3.0 square degrees of image data of the ecliptic to a limiting magnitude $m(R) \sim 25.6$. From this we found 72 KBOs.

When measuring the luminosity function, we included all past ecliptic surveys which searched for KBOs, and had well calibrated detection efficiencies. We found that, when considering all available data, the luminosity functions of separate surveys were inconsistent. We found that from survey to survey, the inferred large object slopes, α, were consistent, but their density parameters m_o were not. We found however, that by allowing for small shifts in sky density and flux calibrations between surveys, the best-fit luminosity functions could be made consistent.

We improved the Bayesian maximum likelihood technique presented by *Gladman et al.* (1998) to account for possible variations in the apparent luminosity functions from calibration errors, average KBO colour differences, and sky density variations from field to field. Using this new technique, we found that the luminosity function for $m(R) < 26$ was well represented by a power-law and had a best-fit slope $\alpha =$

0.65 ± 0.05. The uncertainty we found for the best-fit slope from our new fitting method is of the same magnitude as that from previous measurements with fewer objects. We concluded however, that the size of the uncertainty was more realistic than those previously obtained, as it took into account effects that previous measures had not.

We also found no evidence for a break in the range of the luminosity function for which we were sensitive. To test at what magnitude a break could occur and still be consistent with our observations, we employed a series of Kolmogorov-Smirnov tests (*Press* 2002) in which we generated a series of artificial observations from a model luminosity function with a bright object slope $\alpha = 0.65$ that broke to a range of shallower slope at a range of break magnitudes. We found that no break could occur for $m(R) \lesssim 24.6$ and still be consistent with our observations. Thus, we concluded that the break observed by *Bernstein et al.* (2004) must occur at fainter magnitudes.

Our observations confirmed the results of previous works. Namely, that the luminosity function slope $\alpha = 0.65 \pm 0.05$ implies that the size distribution slope is $q = 4.25 \pm 0.25$. This steep slope is inconsistent with a collisional cascade equilibrium, but is however, consistent with the slopes produced by large object accretion in the simulations from *Stern and Colwell* (1997a), *Kenyon and Bromley* (2001), and *Kenyon* (2002). If KBOs formed in-situ, this slope implies that accretion could have lasted no more than a few 100 Myr, otherwise the large object slope would be shallower than that observed.

1.4.2 The Luminosity Function from a Broken Power-law Size Distribution presented in Chapter 3

The break from a steep power-law in the KBO luminosity function observed by *Bernstein et al.* (2004) hints that the under-lying size distribution also breaks from a steep power-law at some size. Unfortunately, the functions they chose to describe the luminosity function have no link to an under-lying size distribution, which makes the interpretation of the shape of their results in terms of the KBO size distribution difficult. This inspired the work we presented in *Fraser and Kavelaars* (2008a).

Using the technique presented in *Gladman et al.* (2001) and *Fraser et al.* (2008), we derived the functional form the of the luminosity function that would be observed from a population of planetesimals with a broken power-law size distribution, which we denote the Fraser function. This new functional form allows a direct interpretation of the KBO luminosity function in terms of the size distribution, and describes the luminosity function shape in terms of the size distribution parameters - large and small object slopes, and break diameter - or alternatively, in the luminosity function parameters - bright and faint object slopes, and break magnitude.

Using the maximum likelihood technique we developed in *Fraser et al.* (2008), we fit the Fraser function to the available observations. The best-fit luminosity function corresponds to a size distribution that breaks from slope $q_1 \sim 4.5$ to a slope $q_2 \sim -1$ at break diameter $D_b \sim 40$ km. We found that the uncertainties in the fit were large, and dominated by the lack of data sensitive to the break. We concluded that more observations sensitive to KBOs with $m(R) \sim 27$ were needed before an accurate measure of the size distribution could be made.

1.4.3 The Break in the Luminosity Function presented in Chapter 4

Inspired by the findings of *Fraser and Kavelaars* (2008a), we performed a deep ecliptic KBO survey using Suprime-Cam on the Subaru Telescope (*Miyazaki et al.* 2002a). We surveyed ~ 0.3 square degrees to a limiting magnitude $m(R) \sim 26.8$ and found 36 new KBOs. We fit the Fraser function to all available data with well characterized efficiency functions using the maximum likelihood technique we derived in *Fraser et al.* (2008). We found that the size distribution that matches the best-fit luminosity function has a large object slope $q_1 = 4.8 \pm 0.07$ that breaks to a small object slope $q_2 = 1.9 \pm 0.3$ at a diameter $D_b = 60 \pm 20$ km.

Our findings are in general agreement with the recent results of *Fuentes and Hol-*

man (2008) who performed a similar survey and found that the luminosity function exhibits a break. Their findings however, demonstrate a concerning discrepancy in their observed sky density of objects compared to the that from the data (ours and others) we considered; they observed a factor of ~ 4 more objects than the LF of other surveys predict they should have detected. This difference is well outside the range of uncertainty of the best-fit luminosity function we present and cannot be accounted for by the small calibration errors and sky density variations one would expect from survey to survey. The source of this discrepancy remains unknown.

Bernstein et al. (2004) wished to compare the size distributions of dynamically hot or excited (high eccentricity and inclination) and dynamically cold (low-e/i) KBOs, as certain Kuiper belt formation scenarios predict different size distributions for the hot and cold populations (for example, the Neptune migration scenario of *Levison et al.* 2008, predicts that the hot population will have a size distribution indicative of a more evolved accretion process). As a first glance at this problem, they arbitrarily assigned the hot population as those sources with inclinations, $i > 5^o$ and those with $i < 5^o$ to the cold population. They found that the cold population exhibited a steeper large objects size distribution, but the difference was not statistically significant.

Using all of our survey data, as well as that from past works, we made the same inclination cut as *Bernstein et al.* (2004). We considered only those data with KBO inclinations that could be measured with some accuracy, and found that a luminosity function consistent with the 1-sigma limits of the fit to the hot population, was a statistically satisfactory fit to the cold population. Therefore we concluded that there was no detectable difference between the dynamically cold and hot populations in the data at hand.

1.4.4 Modeling Collisional Evolution in the Kuiper Belt presented in Chapter 5

The observations and results of *Fraser and Kavelaars* (2008b) presented a curious result; the Kuiper belt size distribution is steep for large objects, suggesting a short accretion period, and a large break-diameter, consistent with substantial collisional bombardment. The existence of Pluto sized objects, combined with the short accretion time implies that the primordial Kuiper belt must have been substantially more massive. Something shut accretion off by depleting the mass in the belt, and exciting the objects onto the orbits we see today.

This scenario spurred the question, under conditions similar to the modern-day Kuiper belt (low mass, high relative velocities), could the size distribution evolve to its current state on timescales shorter than the age of the Solar system, or did the collisional evolution occur before the Kuiper belt lost the majority of its mass?

To test this question, we developed a simple collisional evolution model, in which disruptive collision rates are calculated for a belt of planetesimals as a function of size. From this, and the implementation of a reasonable strength and fragmentation model suitable for cold, icy bodies, the size distribution of those planetesimals is tracked as a function of time.

Using non-physical model parameters (size bin-widths, time-steps, etc.) which accurately estimated the size distribution of large objects, we calculated the evolution of the Kuiper belt under a range of densities, with different size distributions compatible with that inferred from the observations of *Fraser and Kavelaars* (2008b). We found that, with KBO densities similar to those currently observed, the observable size distribution (break diameter and break slope) did not evolve on billion year timescales. We found however, that if the KBO density was an order of magnitude larger than observed, substantial evolution of the observable size distribution would occur on timescales $\lesssim 500$ Myr.

We also found that the large objects underwent minimal collisional disruption during our simulations for all KBO densities considered. Thus the large object size distribution was preserved on billion year timescales.

These results suggest a scenario in which, a massive primordial Kuiper belt underwent accretion for long enough to produce the largest observed KBOs and the large object slope observed. At which point, some mass depletion event occurred, which also excited the KBO orbits. Before most of the mass was depleted, enough collisional evolution occurred to produce the current size distribution. Once this process was finished, we were left with a Kuiper belt size distribution that has remained effectively unchanged since the depletion event.

Finally, these simulations demonstrate that collisonal evolution does not produce a power-law size distribution, but a wavy function instead. Surveys which can disentangle KBO sizes and distances will likely detect the signatures of this wave for objects larger than $r \gtrsim 1$ km.

We present a short review and discussion of our findings in Chapter 6, and recommend directions for future work.

Chapter 2

The Kuiper Belt Luminosity Function from $m_R = 21$ to 26.

Wesley C. Fraser, JJ Kavelaars, M. J. Holman, C. J. Pritchet, B. J. Gladman, T. Grav, R. L. Jones, J. MacWilliams, J.-M.Petit

Based on Icarus Volume 195 (2008) 827-843, doi:10.1016/j.icarus.2008.01.014

Abstract

We have performed an ecliptic imaging survey of the Kuiper belt with our deepest and widest field achieving a limiting flux of $m(g')_{50\%} \sim 26.4$, with a sky coverage of 3.0 square-degrees. This is the largest coverage of any Kuiper belt survey to this depth. We detect 72 objects, two of which have been previously observed. We have improved the Bayesian maximum likelihood fitting technique presented in Gladman et al. (1998) to account for calibration and sky density variations and have used this to determine the luminosity function of the Kuiper belt. Combining our detections with previous surveys, we find the luminosity function is well represented by a single power-law with slope $\alpha = 0.65 \pm 0.05$ and an on ecliptic sky density of 1 object per square-degree brighter than $m_R = 23.42 \pm 0.13$. Assuming constant albedos, this slope suggests a differential size-distribution slope of 4.25 ± 0.25, which is steeper than the Dohnanyi slope of 3.5 expected if the belt is in a state of collisional equilibrium. We find no evidence for a roll-over or knee in the luminosity function and reject such models brightward of $m(R) \sim 24.6$.

2.1 Introduction

The study of extrasolar debris and dust disks has revealed that, for at least some of these disks to exist as we see them, there must be a source which is responsible for replenishment of small-grain dust in the disk. Otherwise, due to radiation pressure, the small grain dust would be blown out of their stellar systems on time scales shorter than the age of the star. A disk of planetesimals embedded in the dust disk which is undergoing collisional evolution is a likely source of this dust. Disruptive collisions could produce the necessary influx of dust to extend the lifetime of the disk beyond the dust blow-out time. See *Meyer et al.* (2006) for a current review of debris disks.

The Kuiper belt is analogous to these extra-solar planetesimal disks, and provides an excellent laboratory to study and understand the properties of these planetesimals and the processes that affect them, including collisional processes, tensile strengths, compositions, and the mechanisms by which they formed. Knowledge of the size distribution in the belt can constrain much of this information. The size distribution of small objects provides information on the bulk material properties of the objects, (*O'Brien and Greenberg* 2003, *Kenyon and Bromley* 2004) while the size distribution of large objects can provide information on the conditions under which these bodies formed (*Kenyon* 2002).

We performed a 3.0 square-degree survey of the Kuiper belt to determine the size-distribution of large ($D \gtrsim 50$ km) Kuiper belt objects (KBOs) via a measure of the belt's luminosity function. This is the deepest photometric Kuiper belt survey of this size ever completed.

In section 2 we describe our observations. In section 3 we describe our search technique and data analysis. In section 4, we derive a relation between the size-distribution and the luminosity function. In section 5, we describe the statistical analysis used. We present our results in section 6. In section 7 we discuss the implications of our findings, and in section 8 we present our conclusions.

2.2 Observations

The observations used in our survey were taken with the 3.6 m Canada-France-Hawaii Telescope (CFHT) and the Cerro-Tololo-Interamerican Observatory (CTIO) 4m Blanco telescope. Observations at CFHT were acquired with both the CFH12k (0.33 square degree fov) and MEGAPrime (0.88 square degree fov) mosaic cameras while observations at CTIO were made with the Mosaic2 camera (0.38 square degree fov), providing 0.67, 0.84, and 1.54 square degrees of searchable area respectively for a total of 3.0 square degrees of searchable area. Details of the observations are provided in Tables 2.1 and 2.2.

All of these observations were originally acquired for use in searches for satellites of Uranus and Neptune (*Kavelaars et al.* 2004, *Holman et al.* 2004) and prior to this work, none of these fields had been searched for KBOs. The observations were made when Uranus and Neptune (and all KBOs in each field) were at or near opposition, and covered the projected Hill-spheres of each planet. The CFH12k and Mosaic2 observations excluded the area closer than $3'$ to the planets, to avoid scattered light in the images. These observations all occurred near the ecliptic and are well suited to a deep search for Kuiper belt objects (KBOs).

Approximately 10-20 bright, non-saturated stars (~ 20 mag.) per chip were used as reference stars for the image reductions. The variation in the average reference star magnitudes follow approximately that expected from the varying airmass of the observations (see Fig. 2.1) indicating photometric conditions during the observations. The remaining scatter, $\sim 0.02-0.04$ mag is insignificant as it is significantly less than the shot noise for the brightest objects detected.

2.3 The Data Processing and Image Search

To determine the behavior of KBO size distribution requires the discovery of a large number of faint moving sources. If long exposures are used, then the sources will move far enough (more than the size of the seeing disk) that a trailed image results and no additional depth will be achieved. In our deep searches we have adopted a strategy of taking exposures short enough that trailing losses will be negligible. We then shift the individual exposures to account for the expected sky motions of the objects of interest. These shifted images are then combined together to achieve the depth needed. To account for the various possible sky motions of KBOs, we have shifted the images at a variety of rates and angles and then *visually* examined each of the combined images (stacks), searching for point like sources (see Fig. 2.2).

2.3.1 Data Preprocessing

MEGAPrime: CFHT provides wide field imaging data from the MEGAPrime camera in a 'preprocessed' format, ready for science exploitation. The frames provided have been processed using the CFHT ELIXIR/FLIPS (*Magnier and Cuillandre* 2004) processing system. As part of this processing, unique bias, flat-field, fringe, and scattered light images are produced for each 'camera-run' (typically matching a 14 night dark-run) and applied to all frames acquired during that camera run. Dark runs are broken into multiple camera-runs if a significant change in the camera performance or image characteristics is detected. All the MEGAPrime images used in this project were acquired within a single camera-run and have been 'detrended' with a common set of calibrator images. Standard calibration from CFHT results in a flux conserved image with constant sky level across the image that has a typical variation of ±3%.

CFH12K: These data were originally acquired as part of a search for irregular satellites of Uranus (*Kavelaars et al.* 2004) and are different from the data used for the wide field satellite search presented in *Petit et al.* (2006). Due to the strong time constraints of the imaging, the images were acquired in 'classical' observing mode and not automatically detrended by the CFHT queued service observing team. In November 2004 the Canadian Astronomical Data Center (CADC) acquired the ELIXIR/FLIPS software and calibrators for the CFH12K data and subsequently 'detrended' the entire set of CFH12K images for which global calibrator frames (bias, flats, fringe, scattered light) were available. Part of the re-processing effort included the re-processing of the CFH12K frames used in this project. These reprocessed images were used in this search and provide a sky flatness of typically ±4%.

CTIO: The CTIO images were originally acquired as part of a project to search for satellites of Neptune (*Holman et al.* 2004). Bias frames were acquired on each observing night and a combination of the overscan strip and an average of a dozen bias frames was used to remove the instrumental ADC bias from each frame. During the period of observations, a number (~ 15) of independent fields were observed in order to measure the astrometric positions of some previously-known Kuiper belt objects. These sequences of fields were 'median combined' using the IRAF images.median task with high pixel clipping. These combined images provided an excellent flat-field frame that was divided into the search images using the IRAF (*Tody* 1993) mscred.ccdproc task. This process resulted in images which have flat sky across the entire mosaic with a typical scatter of ±3% in the sky flux level.

The curvature of the focal plane for all instruments used in this project was small enough compared to the spatial shifts applied to the images during image processing, such that spatially flattening the images was unnecessary.

For the MEGAPrime and CFH12k data, zeropoint calibrations were done with the standard Elixir routines and were provided by the CFHT Elixir QSO (*Magnier and Cuillandre* 2004) and were reported to be $Z_{field,g'} = 26.46 \pm 0.02$ mags. and $Z_{field,R} = 26.22 \pm 0.02$ mags. Hence these magnitudes are presented in the Sloan g' (*Smith et al.* 2002) and Kron-Cousins R. For the N10032W3, N11033, NEP0813NW3, and NEP0815NE3 fields, calibration frames were unavailable, and a nominal zeropoint for the CTIO mosaic of $Z_{VR} = 26.0$ was used presenting the magnitudes of the objects discovered in these frames in the VR filter.

2.3.2 Artificial Object Planting

To determine the search efficiency as a function of magnitude, artificial objects representative of KBOs were added (implanted) in the images.

The sky rate of motion ($\dot{\theta}$) of an object on a circular orbit observed at opposition on the ecliptic, at heliocentric distance r can be approximately given by [1]

$$\dot{\theta} \sim 148 \left[\frac{1}{\Delta} - \frac{1}{r^{3/2}}\right] \text{ arcsec. hr}^{-1}. \tag{2.1}$$

We implanted 100-150 moving sources into each CCD image. All sources were added blindly to the data before searching began; the artificial source lists were revealed to the operator only after searching was completed. The rates and angles of motion of the artificial sources (approximately $1.3-4.1$ arcsec. hr^{-1} and $\pm 10^o$ from the ecliptic) were typical of objects on circular orbits at heliocentric distances from $25-100$ AU with inclinations between $0-70^o$. Each implanted source was given a randomly selected flux, equivalent to that of a source between $23-27$ mag. The distribution of artificial sources is shown in Fig. 2.3. Additionally, five artificial sources with flux levels equivalent to 21st magnitude sources were implanted, with zero inclination. These objects have sufficient flux to allow us to flag errors in the image combining

---

[1] A full derivation of this equation is presented in Appendix B

algorithms (failed image subtraction, wrong mask limits, etc.) in advance of searching the data, and provided reference moving sources for computing aperture corrections in the final image combinations.

To account for image-to-image flux variations due to changes in airmass and possible sky transparency, the flux of the planted artificial objects was varied with respect to a reference image (usually the middle image in the list) to match the average flux variation of the reference stars (see Fig. 2.1).

The point spread function (PSF) for each frame was approximated on a per-chip basis using the stellar profile of a single bright isolated star. The PSF variation across individual images was small enough that the use of a PSF that varied with position was unnecessary.

Artificial sources whose sky motion would result in a drift of the centroid of the PSF by more than one pixel during an exposure were represented by a series of fainter sources. The number of faint objects was equal to the number of pixels the source would drift during the exposure. The total flux of all the fainter sources was equal to the flux of the original source. In this way, we fully included trailing effects into the implanted sources, and thus accounted for the effects of trailing in our final search efficiencies.

2.3.3 Image Subtraction

During our previous deep searches (*Gladman et al.* 1998, 2001, *Holman et al.* 2004, *Kavelaars et al.* 2004) we found that the two largest inhibitors to this search method are trails in the combined images (caused by bright stars) and the enormous human effort required to visually examine the broad range of rate/angle combinations needed to ensure detection of KBOs. To combat these issues, we utilize an image subtraction routine to remove most stationary background sources and implement a new image display method which greatly eases the strain on the user during the visual image search. We describe the image subtraction routine, and the image display method here.

A template image was subtracted from each image to remove stationary sources from individual images prior to being stacked, thus improving our ability to detect moving sources. To create the image subtraction template, an artificial skepticism weighted average of all images (*Stetson* 1989), with the artificial moving sources already added, was created. This method creates a per-pixel weighted average, with weights calculated iteratively, and quickly converges on an average which places very little weight on spurious pixels such as cosmic ray hits.

For our image subtractions, we chose to use psfmatch3 developed by one of us (CJP) for the Supernova Legacy Survey (*Pritchet* 2005, *Astier et al.* 2006). This subtraction routine compensates for variations between the image quality of the template image and that of the individual images. Several programs that perform this task already exist (see *Alard* (2000) and references therein). Psfmatch3 has several advantages. The subtraction kernel can have arbitrary form, and does not require representation by a set of basis functions to perform the subtraction. In addition, it can automatically remove both spatial and background variations between images. The result of the subtraction routine, is smooth subtracted images with zero average backgrounds. A detailed description of the method is presented in Appendix C.

While the image subtraction removed any stationary non-saturated sources, cosmic ray spikes and other spurious hot pixels remained. To compensate for this, an image mask was applied, such that if a pixel had a value outside a chosen range, then a 3 pixel by 3 pixel box about that pixel was set to have zero value. The lower limit to the range was chosen to be -5 times the background noise (the average background was set to zero in the image subtraction). The upper limit was chosen to be ~ 25000 counts, such that most saturated regions and cosmic ray spikes were masked out of the data. This procedure masked the centres of the brightest KBO sources. This however, did not hinder the detections of these sources as they were still glaringly obvious even in individual frames.

2.3.4 Image Stacking

The subtracted, masked images containing artificial sources were shifted before they were stacked, such that each subsequent image was spatially shifted to compensate for the predicted motion of KBOs in the frame. Sources whose sky motion was well matched by the shifts applied to the images appear nearly round in the stack (see Fig. 2.2) while any residual flux from stationary sources was trailed.

If a source's rate of motion was not well matched by the spatial shifts applied to the subtracted images, that source appeared extended in the stack. This characteristic trailing provided a very robust means of discriminating between real sources and noise. Noise sources were produced during the shifting and stacking when positive flux regions from different images were caused to overlap by the choice of spatial shifts. These false sources, however, did not show the image shape variation characteristic of a real source; false sources did exhibit trailing, but of a different length and width compared to a real (or artificial) source. As such, false sources were not selected as candidates by the trained operator.

The template image used for the Psfmatch3 subtraction process contains both the real and artificial moving sources. These appear as faint trails in the template image. Subtracting this template from the input images results in a low flux area behind each moving source. This feature only occurs around the positions of real (and artificial) moving sources and provides an additional and robust means of source-noise discrimination (see Fig. 2.2) and was required to be present in order to mark a source as a candidate.

The quality of the image subtraction, and hence the final searchable images suffered from a few effects: bad columns in the CCD, bleeding from saturated stars, and regions of poor subtraction around bright galaxies. These problems were exacerbated by image shifting; the unsearchable area of these regions were expanded, reducing the overall searchable area. Gradients of the background caused by bad image subtraction around bright sources, produced images that were difficult to display, reducing the search efficiency. Our efficiency of detecting artificial, planted sources accounts for all reductions in area as the artificial sources were planted at random locations occupying the full spatial extent of each CCD image.

2.3.5 Visual Search

To search the combined stack of shifted images, the stacks were divided up into ~ 200 image subsections with a 20 pixel overlap between neighboring subsections. One-by-one, a grid of rates and angles like that shown in Fig. 2.2 was displayed for each image subsection. Each grid was searched by eye, and sources were recognized by their characteristic trailing and subtraction wells. We found that a five-by-five grid of shift rates and angles maximized the detection efficiency while minimizing the time spent searching. The low variations in the sky background, resulting from the template subtraction, and an image display tool developed specifically for this searching allowed us to rapidly search many data sets.

The pixel coordinates of potential candidates were recorded along with the rate and angle combination that produced the most circular image. A candidate was selected as a planted object if its marked image location was within 10 pixels of an artificial source location. The list of detected artificial candidates was used to determine the detection efficiency as a function of artificial source brightness. The detection efficiencies for each chip of a given field were averaged together to provide a global, per field, detection efficiency which we then modeled (see Fig. 2.4 and Table 2.3) using the equation [2]

$$\eta\left(m|\eta_{max}, m_{\star}, g\right) = \frac{\eta_{max}}{2}\left[1 - \tanh\left(\frac{m - m_{\star}}{g}\right)\right]. \tag{2.2}$$

---

[2] In Equation 2.2, η_{max} is the peak detection efficiency, $m_{\star}$ is the half peak efficiency magnitude, and g is approximately half the width of the falloff from the peak efficiency to zero.

Our deepest and widest field has a $\eta(m) = 50\%$ threshold at $m(g') = 26.4$ and a sky coverage of 0.84 square degrees. The sky coverage of our combined data is 3.0 square-degrees.

Remaining candidates not marked as artificial source detections were re-examined at a finer grid of 8 rates and 8 angles to further discriminate between real sources and noise. Candidates were rejected as false positives during this process if the variation of their image shape and trailing length with rate and angle did not match that of brighter sources with similar apparent rates of motion, whose detection was more robust. While this approach allowed us to isolate and remove false detections, the artificial sources were treated differently from the real sources, as we did not examine candidates marked as artificial sources in the finer rate and angle grid. The brightnesses of all false positives were found to be faintward of the 50% threshold of their discovery field, when their fluxes were measured in the same way as all real detections. Therefore, below the 50% threshold, our search efficiency was no longer representative of the true search efficiency, and subsequently, sources fainter than the 50% threshold of each field are ignored in our analysis. [NOTE: Here we define the 50% threshold as the point where $\eta\,(m) = 50\%$.]

A series of follow-up images of the MEGAPrime field as well as the NEP0813NW3 CTIO field were obtained one or two nights after the initial discovery images. Using the short first night discovery arcs, we projected the motion of each detection forward to the time of the follow-up observations in order to predict the sky location of the source on the second night's images. For 3 of the 25 sources in the MEGAPrime field, the predicted location placed the sources in the gaps between the CCDs of the MEGAPrime MOSAIC. Aside from these 3 sources, all of our initial detections brighter than the 50% threshold were confirmed. Only the faintest initial detection in the MEGAPrime field was not confirmed on the second night, likely due to poorer average seeing conditions during the second nights observations. All 6 detections in the NEP0813NW3 field were successfully confirmed on the second night.

None of our other search fields had follow-up observations. We were confident, however, that all detections in the other fields brightward of the 50% threshold were real because all detections brightward of the 50% threshold (excluding those that fell on chip gaps) in the MEGAPrime and NEP0813NW3 fields were confirmed, and all fields were processed and searched with identical procedures.

For the range of rates and angles that we planted objects into the data, we found no significant variation in detection efficiency versus rate or angle of motion for any of our fields (see Fig. 2.3). This is important to note because any significant variation in efficiency with rate of motion needs to be included when deriving the size distribution from the observed luminosity function. We did not search for sources with rates of motion consistent with objects at distances further than 100 AU as the search method we employed is not sensitive to sources beyond this distance; such distant objects would not show enough apparent motion over the time-span of our observations to detect the faintest sources, and a degradation of the detection efficiency with distance would occur. Therefore, our determination of the luminosity function only applies to KBOs closer than 100 AU.

2.3.6 Source flux measurements and detection confidence

To measure the flux from each detected source, we stacked the non-subtracted images containing the artificial objects. These images were shifted at the rate and angle that produced the roundest image for the source whose brightness was to be measured. Three sets of stacks were produced, by averaging the images, while using a pixel by pixel cut that threw away pixel values outside 3-sigma of the mean value. Three averages were made from images from the first half, middle half, and last half of the observing period for each field. These average images provided three separate, mostly uncorrelated, measurements of each source's flux. Aperture photometry was performed using the IRAF daophot.phot task, set to use an aperture of 4 pixels radius (close to the size of the FWHM of point-sources in our images). Using the five 21st magnitude planted 'reference' objects, and the mkapfile IRAF routine, aperture corrections were determined for each of the three image combinations (first, middle last) and were used to correct individual flux measurements for each source. The IRAF mkapfile task reported our aperture corrections to an accuracy of $\sigma_{aper} \lesssim 0.03$. The magnitudes, as measured on each exposure set, were averaged for the final reported magnitudes (see Table 2.4). We did not measure the flux in a particular stack for sources that were within a few seeing disks of bright or bloomed stars or galaxies (~ 1 in 10 possible source measurements), in that particular stack.

For two objects in the MEGAPrime data, the measured magnitudes varied significantly more than the uncertainty of each individual measurement, indicating a possible light curve. For these two objects, the magnitudes measured from the first image stack were used in our determination of the luminosity function, as was done in *Bernstein et al.* (2004). The second night's data provided an additional 3 magnitude measurements of any followed-up source. For all but the variable sources, we used the average magnitude measured from all image stacks including those from the second night.

2.3.7 Characterization

As required by the maximum likelihood routine, we parametrize the magnitude uncertainty and detection efficiency of our survey. The scatter between each artificial source's measured and inserted magnitudes was used to determine the precision of our flux measurements.

For background limited sources, the uncertainty of a source's measured magnitude can be represented by

$$\Delta m = \gamma 10^{(m-Z)/2.5} \tag{2.3}$$

where Z is the telescope zeropoint. γ is a function of the background b, the camera gain g, and the on-source integration time, and is fit to the scatter of the artificial source's measured and inserted magnitudes. The fit values of γ for each field can be seen in Table 2.3. The magnitude measurement scatter for each source was then drawn from Eq. 2.3 using these best fit values.

The theoretical value of γ is [3]

$$\gamma^* = \frac{2.5}{\ln 10}\sqrt{\frac{\pi r^2 b}{gtN}} \tag{2.4}$$

where N is the number of exposures. If we use the typical values from our MEGAPrime observations, we expect a value of $\gamma^* = 0.08$. The measured value of $\gamma = 0.27$ is clearly larger. *Newberry* (1991) however, has shown that the noise calculation from Eq. 2.4 is incomplete, and does not fully account for the noise introduced into observations during the data reductions. They found that the noise estimate given in Eq. 2.4 can be too small by a factor of 2. Similarly, source fluxes were measured off of images that were shifted and stacked. If the shifts were slightly different than the source's true motion, the measured magnitude would differ slightly from the true magnitude. Thus we find that the uncertainties measured from the artificial sources are close to the expected values. The net uncertainties used in our luminosity function determinations are the 1-sigma shot-noise, Δm, aperture correction ($\sigma_{aper} \lesssim 0.03$), and calibration uncertainties, added in quadrature.

2.4 The Luminosity Function

The size distribution of the KBOs can be determined directly from their luminosity function. The relation between the luminosity function and the size distribution has been derived previously (see, for example, *Gladman et al.* (2001)). We reproduce the relation and discuss complications due to possible variations of KBO albedos, using

---

[3] A full derivation of this equation can be found in Appendix D

a slightly different approach than that in *Gladman et al.* (2001).

Consider the number of objects N in a survey field, given by

$$N = A \int \int R(r)\, S(D)\, dDdr \tag{2.5}$$

where $R(r)$ and $S(D)$ are the radial and size distribution functions, r and D are object heliocentric distance and diameter, and A is some normalization constant. Here we have assumed that the size distribution is independent of the radial distribution, as there exists no evidence to suggest otherwise. We model the size distribution as $S(D) \propto D^{-q}$. The magnitude m of an object at heliocentric distance r and geocentric distance Δ measured in AU, with diameter D in kilometers, and albedo p_λ, is

$$m = K_\lambda + 2.5 \log_{10}\left(r^2 \Delta^2 D^{-2} p_\lambda^{-1}\right), \tag{2.6}$$

where K_λ and p_λ are wavelength dependent; in R-band, $p_R \sim 4\%$ gives $K_R \sim 18.8$. The smallest observable object at a given distance r in a survey with limiting magnitude m_{max}, has diameter $D_{min} = p_\lambda^{-1/2} r^2 10^{(K_\lambda - m_{max})/5}$ where we have made the approximation $r \equiv \Delta$. Similarly, the largest observed object at distance r will have diameter $D_{max} = p_\lambda^{-1/2} r^2 10^{(K_\lambda - m_{min})/5}$.

Using these limits and integrating, Eq. 2.5 becomes

$$N(m < m_{max}) = A \frac{\left[10^{(1-q)(K_\lambda - m_{min})/5} - 10^{(1-q)(K_\lambda - m_{max})/5}\right]}{1-q} \int \frac{r^{2(1-q)}}{p_\lambda^{(1-q)/2}} R(r) dr \tag{2.7}$$

if $q \neq 1$. Note: this assumes that D_{min}/D_{max} are not the smallest/largest objects in the belt; if this were the case, using D_{min}/D_{max} as the integration limits as we have defined them here is incorrect.

For $q > 1$ and a survey where $(q-1)\left(\frac{m_{max} - m_{min}}{5}\right) \geq 2$, we have $10^{(1-q)(K - m_{min})/5} \ll$

$10^{(1-q)(K-m_{max})/5}$, and the cumulative luminosity function is given by

$$\begin{aligned} N(m < m_{max}) &\simeq A\frac{10^{(1-q)(K-m_{max})/5}}{1-q} \int \frac{r^{2(1-q)}}{p^{(1-q)/2}} R(r)dr \\ &\simeq \frac{A}{(1-q)} 10^{\alpha(m_{max}-K)} \int \frac{r^{2(1-q)}}{p^{(1-q)/2}} R(r)dr \end{aligned} \tag{2.8}$$

where we have substituted $q = 5\alpha + 1$.

The observed cumulative luminosity function is well represented by a power-law of the form

$$N(m) = 10^{\alpha(m-m_o)}. \tag{2.9}$$

which gives the number of KBOs per square-degree, on the belt mid-plane, brighter than magnitude m. Comparing this with Eq. 2.8, reveals that the luminosity function slope α and the size distribution slope q are related by

$$q = 5\alpha + 1. \tag{2.10}$$

From Eqs. 2.8 and 2.10 we see that, for a size distribution that is independent of distance, the choice in radial distribution is not significant and only affects the interpretation of the normalization of the observed luminosity function, not the inferred size distribution slope.

Here we have assumed that the KBO albedos do not vary with distance, or size. If the distribution of KBO albedos varies only with distance, then this will only affect the normalization of the luminosity function.

The albedo of Pluto and Eris ($D \gtrsim 2000km$) are $p_{Pluto} \sim 0.6$ and $p_{Eris} \sim 0.6-0.86$ (*Young et al.* 2001, *Bertoldi et al.* 2006, *Brown et al.* 2006) while smaller objects ($D \sim 100$ km) have been shown to have albedos $p \sim 0.06$ (*Grundy et al.* 2005). These data suggest an increase in albedo with size. We can understand the effects of such a trend on the interpretation of the LF by considering a toy model where KBO albedos vary as $p \sim D^{-\beta}$. This functional form retains the analyticity of Eq. 2.5, and reveals the effects of albedo variations on the inferred size distribution. Under this assumption, Eq. 2.8 becomes

$$N(m < m_{max}) = A \int \frac{r^{\frac{4(1-q)}{2-\beta}}}{1-q} R(r) dr 10^{\frac{(K-m_{max})(1-q)}{2.5(2-\beta)}}. \tag{2.11}$$

Thus the slope of the size distribution is

$$q = 5\alpha \left(1 - \frac{\beta}{2}\right) + 1 \tag{2.12}$$

We see that in the case of constant albedo ($\beta = 0$) we get back Eq. 2.10.

Current albedo data imply $\beta \sim -1$ (*Stansberry et al.* 2007). Thus, an estimate of q which assumes $\beta = 0$ potentially under-estimates the steepness of the intrinsic size distribution. Our knowledge of the relation between albedo and size however, is currently insufficient to constrain β.

The reader is cautioned that the current determinations of the size distribution from the Kuiper belt luminosity function are based on a few poorly constrained estimates of KBO physical properties and the inferred slope q is probably underestimated.

2.5 Maximum Likelihood fits

To determine the optimal values of α and m_o, we use a maximum likelihood method. We extend the maximum likelihood analysis of *Gladman et al.* (2001) to account for observations made in different wave-bands, as well as systematic differences in the normalization, m_o, that may affect the results of combining separate data sets, such as systematic calibration errors, sky density variations, and variations in average colour of the observed KBOs compared to the average colour of all KBOs.

Given that the probability of detecting an individual KBO is independent of detecting the next, the likelihood function for a single survey k takes the form

$$L_k\left(\alpha, m_o|m_1, m_2, ...\right) \propto \exp^{-\tilde{N_k}} \prod_i P_i \tag{2.13}$$

where m_i is the magnitude of detection i, $\tilde{N_k}$ is the number of objects expected to be detected in a given survey, and P_i is the probability of having object i given the underlying luminosity function. $\tilde{N_k}$ is given by

$$\tilde{N_k} = \int dm\ \Omega\ \eta(m)\ \Sigma(m|\alpha, m_o) \tag{2.14}$$

where Ω is the survey area, $\eta(m) = \eta(m|\eta_{max}, m_*, g)$ is the detection efficiency for an object with magnitude m, and $\Sigma(m|\alpha, m_o)$ is the differential density of objects on the sky. P_i and $\Sigma(m|\alpha, m_o)$ are given by

$$P_i = \int dm\ \Sigma(m|\alpha, m_o)\ \epsilon_i(m). \tag{2.15}$$

and

$$\Sigma(m|\alpha, m_o) = \frac{dN(m)}{dm} = \ln(10)\ \alpha\ 10^{\alpha(m-m_o)}, \tag{2.16}$$

where α is the slope of the luminosity function (LF), m_o is the magnitude at which the sky density is 1 KBO per square degree, and $\epsilon_i(m)$ is a functional representation of the photometric uncertainty for object i. A formal derivation of this likelihood function is presented in *Loredo* (2004).

We choose to represent the magnitude uncertainties as gaussian. ie.

$$\epsilon_i(m) = \frac{1}{\sqrt{2\pi\Delta m_i^2}} e^{\frac{-m^2}{2\Delta m_i^2}} \tag{2.17}$$

where Δm_i is the uncertainty in the magnitude measurement of each object. This treatment of uncertainties for faint sources is incorrect, but is a sufficient approximation for detections brightward of the 50% efficiency threshold. Brightward of this threshold, the gaussian approximation will not affect the results of the maximum likelihood inference (*Bernstein et al.* 2004).

For a group of surveys with calibration uncertainties and colour offset variations much smaller than the uncertainty in the flux measurements of the brightest objects detected, the net likelihood resulting from combining multiple surveys together is the product of the likelihoods of each individual survey. In reality, photometric calibration and colour offset uncertainties are not insignificant, and therefore, need to be considered when combining different surveys.

Additionally, the apparent sky density of KBOs and, hence, m_o are strong functions of latitude and longitude (*Kavelaars et al.* 2008). When combining separate surveys, differences in the flux-limited sky densities will skew the inferred slope of the LF.

We account for these effects with the addition of two new parameters for each survey, the colour parameter C_k, and the density parameter $\Delta m_{o,k}$. Eqs. 2.14, 2.15, and 2.16 become

$$\tilde{N_k} = \int dm\ \Omega\ \eta(m|\eta_{max}, m_*, g)\ \Sigma_k(m - C_k|\alpha, m_o, \Delta m_{o,k}), \tag{2.18}$$

$$P_i = \int dm\ \Sigma_k(m - C_k|\alpha, m_o, \Delta m_{o,k})\ \epsilon_i(m), \tag{2.19}$$

and

$$\Sigma(m - C_k|\alpha, m_o, \Delta m_{o,k}) = \ln(10)\ \alpha\ 10^{\alpha(m - C_k - (m_o - \Delta m_{o,k}))}. \tag{2.20}$$

As can be seen, for the case of a power-law LF, the parameters C_k and $\Delta m_{o,k}$ are degenerate. For a non power-law model however, C_k and $\Delta m_{o,k}$ are no longer degenerate, and need to be treated separately. As we consider non power-law LFs in this manuscript, we choose to treat C_k and $\Delta m_{o,k}$ as different parameters when evaluating the likelihood.

This treatment substantially increases the number of parameters in the fit, while not providing any new information about the shape of the LF. Thus we treat these additional parameters as nuisance parameters, and marginalize (integrate) the likelihood equation over the expected ranges of each parameter. The final likelihood equation when combining $\mathcal{N}$ surveys is

$$\begin{aligned} &L(\alpha, m_o, C_1, C_2, ..., C_{\mathcal{N}}, \Delta m_{o,1}, \Delta m_{o,2}, ..., \Delta m_{o,\mathcal{N}}) \\ &= \prod_{k=1}^{\mathcal{N}} \int \int L_k(\alpha, m_o, C_k, \Delta m_{o,k}) dC_k d\Delta m_{o,k}. \end{aligned} \tag{2.21}$$

2.6 Results

Each detection in our survey is listed in Table 2.4 along with estimated barycentric distance and inclination determined from fit_radec (*Bernstein and Khushalani* 2000). The fit_radec routine determines a set of orbital parameters that best fit the observations in a least-squares sense. Because of the large degeneracies between orbital parameters for short-arc observations such as those presented here, fit_radec initially assumes that the objects are near perihelion, and are on bound, nearly circular orbits, near the ecliptic plane. The routine determines 2-sigma uncertainties, which contain 95% of the orbits which are consistent with the measured positions of the objects. In this survey, we have detected 72 KBOs, 53 of which are brightward of the 50% threshold of our search, and these 53 detections are used in our maximum likelihood analysis.

As the UNE and UNW fields are close on the sky, observed together through the same filter/telescope, and the skies were photometric during those observations, we combine the two fields for the maximum likelihood fits. Similarly, we treat the N10033 and N10032W3 and the NEP0815NW3 and NEP0815NE3 fields in the same fashion. We refer to these combined fields as the UN, CTIO01, and CTIO02 fields. The CTIO01 and CTIO02 fields were not combined together, as they were observed in separate years.

To extend our results, we include the observations from other surveys that have well-measured efficiency functions for each field in the survey. We define the F08 sample as those objects detected in the surveys from *Jewitt et al.* (1998), *Gladman et al.* (1998), *Chiang and Brown* (1999), *Gladman et al.* (2001), *Allen et al.* (2002), and *Petit et al.* (2006), as well as those detected in the UN, CTIO01, and CTIO02 fields.

In the F08 sample we also include all on ecliptic detections in *Trujillo et al.* (2001) (T01) in fields with detection efficiencies classified as 'good' or 'medium'. Because the T01 images cover a large range of latitudes, longitudes, and detection efficiencies, we divided the survey into smaller "sub-fields" to avoid large density variations from field to field. Each sub-field spans ~1 - 1.5 hrs. RA. We do not include any of the high-latitude data from T01 as the KBO latitude distribution is not sufficiently understood to be able to predict the density of KBOs at high latitudes and we are thus unable to provide a reasonable estimate of $\Delta m_{o,k}$ for the high-latitude fields. We avoid complications due to detection efficiency variations by further sub-dividing the data from T01 into separate groups based on the good and medium detection efficiencies defined in that work. We do not consider any T01 fields with detection efficiencies classified as 'poor'. The sub-field divisions listed by field ID (see Table 2 in Trujillo et al. 2001) are presented in Appendix E.

We include all fields from the above surveys, even those with few or no detections in the F08 sample. This is the sample on which all our LF analysis was performed.

We chose to exclude the data from *Bernstein et al.* (2004) as the intent of this work is to determine the shape of the bright end of the luminosity function.

When computing our LF estimate, we ignored all detections fainter than the

$\eta(m)$ = 50% detection threshold of each individual survey, and truncated ("cut") the detection efficiency to zero faintward of that threshold. Correctly determining the efficiency function at low levels is notoriously difficult and prone to error. Effects such as Eddington and Malmquist-bias further complicate detection efficiency measurements, at low brightnesses.

To test for a bias in the fits caused by an efficiency truncation, we ran a series of Monte-Carlo realizations that simulated the observation of a luminosity function from a single survey. We also performed this analysis using a set of surveys with parameters like those in the F08 sample. We performed 2000 random realizations for efficiency cuts ranging from 0-90%. We found that, for a single survey, the mean of the estimated LF slope is biased to steeper slopes when truncating the detection efficiencies at some non-zero threshold. The bias was found to decrease asymptotically to zero as the efficiency threshold was moved faintward.

We found the bias caused by including an efficiency cut is removed however, when combining multiple surveys if the separate surveys have different detection efficiencies. Most detections in a survey occur where $\eta(m) \sim 80\%$. Thus, when two or more surveys are well separated in their limiting magnitudes, so are their detections, which creates a "lever arm" that dominates the slope determination, effectively removing any efficiency cut bias in the fit.

For each field with 5 or more detections which is the minimum number of detections required to provide a reliable measure of the LF, we determined the best-fit parameters for the LF using Eq. 2.13 (see Table 2.5). The 1, 2, and 3-sigma credible regions of these fits are presented in Fig. 2.5. The 1-sigma uncertainties of the best-fit parameters, taken as the extrema of the 1-sigma credible regions, are presented in Table 2.5. Presenting the fit parameter uncertainties in this way describes the full range of allowed values for each parameter individually. These uncertainties are somewhat misleading as they do not describe the correlation between α and m_o (see

Fig. 2.5).

The average (V-R) colour of KBOs is $< V - R >= 0.56$ (*Hainaut and Delsanti* 2002). Using the VR and R magnitude transformation given by *Allen et al.* (2001), as well as the relations between V, R, r' and g' given by *Smith et al.* (2002), we determined the expected offsets between the various filters used in the surveys considered here. We found that the average colours of KBOs are $< VR - R >= 0.03$, $< r' - R >= 0.26$, and $< g' - R >= 0.95$. Using these colours to offset the separate fields to R-band, we find the estimates of m_o provided independently by each survey are not consistent with a single value (see Fig. 2.5). Small shifts in m_o are necessary to make all fields agree at the 1 - 2 sigma level. This is acceptable when considering possible sky density variations, and photometric calibration errors (see Section 2.5) and justifies the more complicated likelihood equation given by Eq. 2.21. We therefore shifted all data to R-band using the expected average KBO colours, and used Eq. 2.21 when determining the best-fit LF parameters.

To determine the possible range in m_o values between surveys, we consider a toy model of the Kuiper belt. As the majority of the objects observed in the surveys considered in this work are Plutinos and classical belt objects (CKBOs), we only consider these objects in the model. We represent the LFs of both populations as power-laws with the same slope, but with different observed sky densities. Then the observed cumulative LF (assuming constant detection efficiencies) is a power-law, and is given by

$$N_{obs} = 10^{\alpha(m-m_{o,c})} + f10^{\alpha(m-m_{o,p})} \equiv 10^{\alpha(m-m_o)} \tag{2.22}$$

where $m_{o,c}$, $m_{o,p}$, and m_o are the magnitudes at which one object per square degree is observed for the CKBOs, the Plutinos, and all populations respectively and f is the ratio of the number Plutinos to CKBOs.

The mean eccentricity of Plutinos is $\bar{e} = 0.15$, and they are $\sim 30\%$ as numerous as the classical belt objects of the intrinsic population. ie. $f = 0.3$ (*Kavelaars et al.* 2008). The magnitude of an object as a function of heliocentric distance r is given by $m \sim K + 10.0 \log(r)$. Thus the variation in $m_{o,p}$ for Plutinos at perihelion versus aphelion is ~ 1 mag. If all CKBOs are observed at $r = 43$ AU, then the difference in m_o between fields that observe Plutinos at perihelion versus aphelion is ~ 0.8 mags. This is an upper estimate of the true offset because not all Plutinos come to perihelion at once, but provides a reasonable range of integration for each $m_{o,k}$ parameter.

Latitude differences between surveys will cause variations in m_o requiring knowledge of the latitude distribution of the Kuiper belt. While the location of the mid-plane is unclear, it is secure that the mid-plane is inconsistent with the ecliptic (*Brown and Pan* 2004, *Elliot et al.* 2005); there is disagreement about whether the mid-plane is the invariable plane. *Brown* (2001) has shown that the KBO latitude distribution above the plane has a Full-Width-Half-Maximum of $\sim 7^o$. Most of the observations considered in the F08 sample are made near the ecliptic. If the true plane of the belt is similar to the invariable plane, or the Kuiper plane proposed by *Brown and Pan* (2004), then the density variation due to latitude between ecliptic fields is at most 5% and would affect the $m_{o,k}$ values by ~ 0.05 mags. This variation is small compared to that expected from changes in longitude, and is ignored in our analysis. We bound the integration of Eq. 2.21 over the $m_{o,k}$ parameters between ± 0.4 mags.

The standard deviation of the $< V - R >$ colour from the MBOSS data set is $\sigma(V - R) \sim 0.15$ (*Hainaut and Delsanti* 2002). Hence, the expected variation in average object colour between separate surveys due solely to KBO colour variation is $\sim 0.15/\sqrt{N}$ where N is the number of objects in a survey. For the fields considered in the F08 sample, $N \sim 1 - 15$. Zeropoint calibration errors between separate surveys have been as high as 0.1 magnitudes. Thus a reasonable range of offsets due to calibrations and colour variation is ~ 0.2 mags. This offset can occur in either a positive or negative sense on the measured magnitude. Thus we bound the integration of Eq. 2.21 over the C_k parameters between ±0.2 mags.

Maximizing Eq. 2.21 using the F08 sample, we find a best fit slope of $\alpha = 0.65 \pm 0.05$ and normalization $m_o = 23.42 \pm 0.13$. The likelihood contours of the fit are shown in Fig. 2.6.

The factor $e^{-\tilde{N}}$ in Eq. 2.21 weights the fit towards the lowest possible number of detections. The m_o that maximizes the likelihood equation given by Eq. 2.21 is the maximal value within the range allowed by the $\Delta m_{o,k}$ that best describes each individual field considered. Thus, the best-fit m_o is not applicable to any one field, but rather is a value typical of all data considered in the fit.

To test if the fit is consistent with the observations, we employed a series of Monte-Carlo simulations. The simulations involved random realizations of a number of objects drawn from the best-fit power-law model ($\alpha = 0.65$, $m_o = 23.42$) equal to the number of objects in the F08 sample with the random magnitudes scattered according to our uncertainty model (see Eqs. 2.3 and 2.17). A best-fit power-law of each realization was determined using our maximum likelihood technique, and the distribution of maximum likelihoods was determined from 1000 realizations. We found that the probability of getting a maximum likelihood less than or equal to the maximum likelihood computed from the F08 sample was 43.2%: the model is fully consistent with these data.

In Fig. 2.7 (*top*) we present a histogram of the differential LF of the F08 sample corrected for detection efficiencies. These data are well described by our best fit. The reader is cautioned however, from drawing conclusions about the LF from this diagram alone. All source magnitudes have been adjusted to R-band using typical KBO colours (see above). The observational data from different surveys however, contain calibration and colour offsets, and the observations have not been adjusted to reflect variations in sky densities, as a standard model of the density variations is not known. The minor discrepancies between the observed LF and the model apparent in Fig. 2.7 may be caused by these effects.

In Fig. 2.7 (*middle*) we show the net effective area for all fields as well as a differential histogram of the object magnitudes shifted to R-band with completeness corrections. The different fields which are included in the F08 sample all have different 50% thresholds, resulting in the broad fall off in effective area between $m(R) \sim 21$ to 26.

In Fig. 2.7 (*bottom*) we show the logarithm of the ratio of the observed and fit differential LFs, as a function of magnitude. This figure shows that the LF from $m(R) = 21$ to 26 is well described by a single power-law.

2.6.1 Broken Power-law Models

Bernstein et al. (2004) conclude that the slope of the luminosity function rolls over to shallower values for fainter magnitudes and that the luminosity function is well described by a rolling power-law given by the functional form

$$\Sigma(m) = \Sigma_{23} 10^{\alpha(m-23)+\alpha'(m-23)^2} \tag{2.23}$$

where $\Sigma(m)$ is the differential surface density of objects, Σ_{23} is the surface density of objects at $m(R) = 23$, α is the bright end slope, and α' is the slope derivative. They found that a rolling power-law was a better fit to their observations than the single power-law used here. This suggests that a deviation in the form of a flattening of the power-law might be visible in our data.

To look for evidence of a roll-over in the KBO LF we fit Eq. 2.23 to the F08 sample. As the density parameter for Eq. 2.23, Σ_{23}, is different from m_o in Eq. 2.9, we introduce a density offset parameter $\Delta\Sigma_k$ as a multiplicative factor in front of Eq. 2.23. We maintain the same range in colour and density offsets as used in the power-law fit (see above) and marginalize C_k and $\Delta\Sigma_k$ over the range ± 0.2 and ± 0.25 respectively. Our maximum likelihood method gives a best-fit $A = 0.79 \pm 0.14$,

$\alpha = 0.74 \pm 0.09$, and $\alpha' = -0.03 \pm 0.04$. Bernstein determined a best-fit of $A = 1.07$, $\alpha = 0.66 \pm 0.03$ $\alpha' = -0.05 \pm 0.015$ (1-sigma uncertainties were extracted from Fig. 4 of *Bernstein et al.* (2004)), consistent with our results. The increase in uncertainty of α and α' in our fit versus that from *Bernstein et al.* (2004) is caused by the marginalization in Eq. 2.21. We feel that our approach provides a more realistic estimate of the true uncertainties.

Additionally we fit a simple broken power-law model by Eq. 2.21. The model LF has a sudden change from the bright-side slope α_1 to the faint-side slope α_2 at a break magnitude m_B, and is given by

$$\Sigma = \begin{cases} 10^{\alpha_1(m-m_o)} & \text{if } m < m_B, \\ 10^{\alpha_2 m + (\alpha_1-\alpha_2)m_B - \alpha_1 m_o} & \text{if } m > m_B. \end{cases} \tag{2.24}$$

The best-fit parameters from maximizing the likelihood for the broken power-law LF while marginalizing over nuisance parameters C_k and $\Delta m_{o,k}$ as per Eq. 2.21 are $m_o = 23.2 \pm 0.5$, $\alpha_1 = 0.69 \pm 0.08$, $\alpha_2 = 0.57 \pm 0.2$, and $m_B = 24.4 \pm 0.7$.

The improvement of the maximum likelihood value when considering the rolling and broken power-law LFs given by Eqs. 2.23 and 2.24 fits is only a few percent over that of the single slope model. Hence the additional degrees of freedom included in the more complicated LFs compared to a single slope power-law does not substantially improve the fit and the higher order models are not statistically warranted in the range of magnitudes considered in the F08 sample. Indeed the best fits of both equations are consistent at the 1-sigma level with no break at all ($\alpha' = 0$ and $\alpha_2 = \alpha_1$).

To test at what magnitude a roll over to shallower slopes would be inconsistent with the F08 sample, we made use of Monte-Carlo simulations and the Kolmogorov-Smirnov (KS) test. In these simulations, we simulated the observation of a broken power-law LF of the form of Eq. 2.24, with $\alpha_1 = 0.65$ breaking to some faint-end slope α_2 at break magnitude m_B. The simulated surveys and total number of detections were chosen to match the surveys and number of detections in the F08 sample. We included the effects of variable m_o and colour offsets between surveys by randomly selecting these offsets for each individual survey.

For a given break magnitude and faint-end slope, a parent population of $\sim 10,000$ objects was generated. This parent population was simulated with a set of random C_k and $\Delta m_{o,k}$ offsets linearly sampled from the marginalization range described above (± 0.2 for C_k and ± 0.4 for $\Delta m_{o,k}$). Calibration and colour offsets occur in the observations in the F08 sample. The random sampling we implement provides a simple means of generating offsets consistent with the way in which those observations were made.

From the parent population, a sub-sample of objects was bootstrapped and the KS-statistic of this sub-sample compared to the parent population was calculated. This procedure was repeated for 1000 random sub-samples of the parent population. In this way, the KS statistic distribution was bootstrapped from the parent population.

The KS statistic of the F08 sample when compared to the parent population was compared to the distribution of KS-statistics generated from the bootstrapped samples. The roll-over model (α_2, m_B) was rejected if 99.7% of the bootstrapped KS statistics were smaller than the KS statistic of the F08 sample. This was repeated 25 times using different random realizations of the C_k and $\Delta m_{o,k}$ offsets for each choice of faint-end slope and break magnitude. The repetition was necessitated by the randomness included with variable C_k and $\Delta m_{o,k}$ values; in certain circumstances, a particular set of colour and m_o offsets will enhance the chances of observing a break. A model could not be rejected if the break was not rejected in 2 or more of the 25 simulation repetitions for that model.

Presented in Fig. 2.8 is the 95% probability contour that a particular break model is rejected by the F08 sample. The contour has been smoothed to remove the effects of course sampling in α_2-m_B space. As expected, brightward of a particular magnitude most break models would likely have been detected in the observations. From these simulations, we conclude that the observations cannot reject the possibility of a break in the Kuiper belt LF with break magnitudes fainter than $m_B(R) \sim 24.3$.

Bernstein et al. (2004) find that the LF is well described by the harmonic mean of a steep power-law for bright objects and a shallow power-law for faint objects with both power-laws contributing equally at magnitude R_{eq}. They find $R_{eq} \sim 22.8 - 23.6$. This is not however inconsistent with the results of our KS test as m_B and R_{eq} are not equivalent parameters between the two LF models. The reader is cautioned about drawing conclusions from comparison of these two parameters.

While no break is apparent in the observations, the best-fit single sloped model is inconsistent with the results from *Bernstein et al.* (2004) at $m(R) \gtrsim 28$ as the number of objects detected in that survey are too few by a factor of ~ 6 from that predicted by the model. To account for this, the LF must roll-over to shallower slopes at some faint magnitude not present in the F08 sample.

2.6.2 The Size Distribution

Our best-fit luminosity function slope is $\alpha = 0.65 \pm 0.05$. Under the assumption that Eq. 2.10 holds, we find that the KBO differential size distribution has a slope of $q = 4.25$ with a 1-sigma uncertainty of 0.25. If the belt is in a state of collisional equilibrium, we would expect the slope to be $q \simeq 3.5$. This is inconsistent with the inferred size distribution at the 3-sigma level. We conclude that, for objects larger than $D \approx 50$ km, the size-distribution of the belt is inconsistent with a system in collisional equilibrium.

2.7 Discussion

To understand what the KBO size distribution tells us about the history of objects in the outer solar system, we must interpret our observations in terms of models that account for the size distribution of a belt of planetesimals. Generally, there are two broad types of models that attempt this, fragmentation models and accretion models.

Analytic fragmentation models are those in which a series of equations accounting for accretion and collisional disruption are solved, producing a steady-state collisional-cascade equilibrium. These models vary in complexity. Some assume that each disruption produces a number of equal size collision remnants (*Dohnanyi* 1969, *Pan and Sari* 2005), while some model object-disruptions with a distribution of collision remnant sizes (*O'Brien and Greenberg* 2003). Some calculations also include various models of KBO physical strengths (*O'Brien and Greenberg* 2003). The detailed results depend on the calculations, but generally the outcome is a differential size distribution in a quasi-equilibrium steady-state with a slope equal to or less than Dohnanyi slope, $q \lesssim 3.5$.

Pan and Sari (2005), assumed that the strengths of large Kuiper belt objects are gravity dominated and modeled a collisional cascade in which all collisions were purely disruptive (no accretion). They found that, for objects smaller than some break size, the size distribution slope was $q = 3$ and could not account for the steep slope observed for large KBOs with this model.

O'Brien and Greenberg (2003) accounted for accretion and fragmentation, and a variation of object strength as a function of size. They found that the equilibrium size distribution slope was related to the power-law slope describing the variation in object disruption energy per unit mass with size. From this model, the Kuiper belt size distribution inferred from the F08 sample implies a unit disruption energy that decreases rapidly with increasing size. This is consistent with objects whose physical strength is dominated by tensile forces, but is inconsistent with objects whose strength is dominated by gravity; these objects have an increasing disruption energy with size. Objects in the tensile strength dominated regime are typically smaller than 1 km in size. The objects we observe here are likely to be gravity dominated and the scaling of KBO disruption energy versus size implied by the model from *O'Brien and Greenberg* (2003) seems unlikely. We conclude from these results that the observed LF and the inferred size distribution is inconsistent with analytic equilibrium models.

The large diversity of fragmentation models have similar outcomes; they predict a shallow size distribution slope of $q \sim 3.5$ which is incompatible with the large object size distribution inferred from the luminosity function of the Kuiper belt.

Numerical accretion models are those in which the size distribution, and orbits of a population of bodies is calculated. Unlike analytic collisional cascade models, the size distribution calculated from accretion models is not assumed to be in steady state, but evolves in time along with the orbital distribution. Models which account for accretion and fragmentation of planetesimals in the region of the Kuiper belt, predict a broken power-law size distribution with a steep slope for large objects ($D \gtrsim 10$ km) that rolls over to a shallower slope for smaller objects ($D \sim 2$ km) (*Kenyon and Bromley* 2001, *Kenyon* 2002, *Kenyon and Bromley* 2004).

These models have two general evolutionary phases. The first phase is planetesimal accretion, in which a large reservoir of planetesimals on nearly circular orbits accrete to form larger bodies via low encounter-velocity collisions. This process rapidly produces a steep size distribution for large objects ($q \gtrsim 5$). Models from *Kenyon and Bromley* (2001) and *Kenyon* (2002) calculate planet growth in the 40-47 AU zone. These models have a relatively low-mass intial Kuiper belt, and do not include stirring from Neptune. They calculate planet growth before Neptune attains its current mass and orbit, and start from bodies with radius $\lesssim$ 1km. Initially, the size distribution of large objects is very steep ($q \gtrsim 5$). After $\sim 100 - 300$ Myr, the slope of the largest objects flattens to $q \sim 4.1 - 4.4$.

The second phase is started when the belt members are stirred up onto dynamically excited orbits (via interactions with Neptune, oligarchs, etc.) such that mutual collisions are mainly catastrophic. Collisional grinding rapidly reduced the slope of the size distribution for small bodies ($D \lesssim 1$ km). The longer the collisional evolution continues, the larger the radius at which the break to shallower slopes occurs. In the models from *Kenyon and Bromley* (2001) and *Kenyon* (2002) the size distribution breaks to $q \lesssim 3.5$ at $D \sim 2 - 20$ km after ~ 1 Gyr.

More complicated models that start with a more massive initial Kuiper belt, and include effects of gas-drag and a more detailed model of object strength, produce large object slopes of $q \sim 3$ and after 4.5 Gyr, and a break at $D \sim 2 - 40$ km to very flat slopes of $q \sim 0 - 0.5$ for small objects (*Kenyon and Bromley* 2004).

The observed size distribution exhibits a steeper slope than those determined by *Kenyon and Bromley* (2004) and is more consistent with models that start with a less massive Kuiper belt. In these models, the break radius grows larger and the large object slope flattens as accretion and collisional evolution continues. An accurate measure of the break size in addition to the large object slope determined here, combined with modeling, may further constrain the duration of accretion in the region of the Kuiper belt.

Accretion models which include migration of Neptune can account for some of the features of the KBO orbit distribution, but come at the cost of complicating the accretion process (Kenyon et al. 2007 and references there in). In these models, most of the current Kuiper belt consists of objects that are scattered by Neptune to their current positions, and originate from regions interior to Neptune's current orbit. Accretion of the KBOs in their original locations proceeds until stirring and scattering by Neptune disrupts the accretion process.

In these migration models the KBOs are initially closer to the Sun than there current locations and accrete in regions of high density, and therefore both the accretion and collision process occur on much faster time-scales than in-situ formation models predict. The migration time-scale becomes an important parameter in these models; too fast a migration and the largest KBOs are not formed, while too slow, and the break size can evolve to be large enough such that it would be detected in the available observations.

Numerical accretion models of KBO formation, are generally in better agreement with the observed large size distribution than collisional cascade equilibrium models. Accretion models suggest that knowledge of the size distribution slope, and the radius at which the break to shallower slopes occurs will provide strong constraint on the accretion dynamics, and KBO formation time-scales. Due to the large degree of complexity in these models however, there is much work needed to interpret the observed size distribution. Models which achieve collisional-cascade equilibrium for large objects cannot account for the observed steep size distribution.

2.8 Conclusions

We have performed a survey of the Kuiper belt with an sky coverage of 3.0 square degrees with our deepest field having a depth of $m(g') = 26.43$ magnitudes. An analysis of current survey data confirms that the luminosity function of the belt is well described by a single slope power-law between $m(R) = 21 - 26$ with a slope of $\alpha = 0.65 \pm 0.05$ and normalization $m_o = 23.42 \pm 0.13$ which is typical of all the fields considered in the F08 sample.

We have shown the necessity of considering calibration, and density effects when inferring the luminosity function from the combination of different surveys that have observed separate regions of the sky, and are not directly calibrated to one-another. Such effects can skew the inferred LF away from the true form, and cause uncertainties in the inference to be highly underestimated.

We conclude that:

1. The Kuiper belt is not in a state of collisional equilibrium for objects larger than $D \approx 50$ km.

2. There is no evidence for a change in the slope of the luminosity function for

magnitudes brighter than $m(R) \sim 24.3$ corresponding to objects with diameters $D \gtrsim 110$ km at 40 AU. The sample of observations considered here is consistent with a best-fit model that breaks at $m(R) \sim 24.4$ to a slope of $\alpha_2 \sim 0.6$, but the more complicated fit is not warranted by the slight improvement in the maximum likelihood value.

3. The observed slope of the luminosity function implies that the size distribution of the Kuiper belt is consistent with a power-law with slope $q = 4.25 \pm 0.25$ for objects with diameters larger than $D \sim 50$ km.

2.9 Acknowledgements

We thank the reviewers for providing excellent feedback and suggestions for improvement of this manuscript. We also thank Tom Loredo for his many discussions in the use of statistics.

This project was funded by the National Science and Engineering Research Council and the National Research Council of Canada. This research used the facilities of the Canadian Astronomy Data Centre operated by the National Research Council of Canada with the support of the Canadian Space Agency.

Table 2.1: Field Details

Field	Telescope	Date (UT)	Camera	Filter	Exp. Time	α	δ	Seeing (")
UNE	CFHT	2001-08-24	CFH12k	Kron-Cousins R	16 × 480 s	21:41:06.6	-14:28:04.9	1.0
UNW	CFHT	2001-08-25	CFH12k	Kron-Cousins R	17 × 480 s	21:38:34.9	-14:37:15.6	0.87
MEGA	CFHT	2004-09-15	MEGAPrime	g'	48 × 240 s	22:24:46.4	-10:46:51.3	0.74
	CFHT	2004-09-16	MEGAPrime	g'	45 × 240 s	22:24:37.9	-10:47:39.0	0.83
N10032W3	Blanco	2001-08-10	Mosaic2	VR	40 × 480 s	20:38:35.8	-18:01:02.5	1.4
N10033	Blanco	2001-08-11	Mosaic2	VR	33 × 480 s	20:39:05.8	-18:37:45.5	1.3
NEP0813NW3	Blanco	2002-08-13	Mosaic2	VR	21 × 480 s	20:45:10	-17:38:27.7	0.87
	Blanco	2002-08-15	Mosaic2	VR	20 × 480 s	20:44:58.9	-17:39:20.7	0.674
NEP0815NE3	Blanco	2002-08-15	Mosaic2	VR	21 × 480 s	20:47:25.0	-17:32:20.8	0.6

Table 2.2: Observation Details. * - Field used only for confirmation purposes. λ - ecliptic longitude (°). β - ecliptic latitude (°). λ_N - longitude with respect to Neptune (°).

Field	Area (°*square*)	λ	β	λ_N
UNE	0.32	322.9	-0.72	15.4
UNW	0.32	322.9	-0.72	15.4
MEGAPrimeN1	0.85	334.9	-0.76	19.9
MEGAPrimeN2 *	-	334.9	-0.76	19.9
N10032W3	0.38	307.4	0.13	0.0
N11033	0.38	307.4	0.13	0.0
NEP0813NW3	0.38	309.6	0.06	0.0
NEP0815NW3 *	-	309.6	0.06	0.0
NEP0815NE3	0.38	309.6	0.06	0.0

Table 2.3: Detection efficiency parameters using Eq. 2.2, and flux measurement error parameter using Eq. 2.3. A - peak efficiency. m_* - magnitude where efficiency is half the peak. g - width parameter. Z - field zeropoint. γ - error parameter.

Field	η_{max}	m_*	g	Z	γ
UNE	0.96	25.32 (R)	0.41	26.21	0.47
UNW	0.97	25.44 (R)	0.40	26.22	0.49
MEGAPrimeN1	0.97	26.43 (g')	0.41	26.46	0.27
N10032W3	0.91	25.10 (VR)	0.46	26.0	0.77
N11033	0.93	25.20 (VR)	0.5	26.0	0.58
NEP0813NW3	0.93	25.13 (VR)	0.34	25.9	0.73
NEP0815NE3	0.97	25.18 (VR)	0.27	25.9	0.58

Object	m	Filter	Δ (AU)	i (∘)
UNEa2 *	23.23 ± 0.03	R	47 ± 5	7 ± 23
UNEa4 *	24.44 ± 0.09	R	45 ± 6	31 ± 32
UNEa6 *	24.56 ± 0.10	R	48 ± 5	2 ± 22
UNEa7	26.17 ± 0.45	R	49 ± 5	0.6 ± 8
UNWa8 *	23.17 ± 0.07	R	42 ± 4	3 ± 16
UNWb11 *	24.59 ± 0.11	R	42 ± 4	1 ± 14
UNWa10 *	25.05 ± 0.17	R	40 ± 4	3 ± 15
UNWa11	25.51 ± 0.25	R	44 ± 4	11 ± 19
UNWa6	25.61 ± 0.28	R	56 ± 15	78 ± 99
MEGAa2 *C	24.10 ± 0.03	g'	42 ± 3	18 ± 7
MEGAa33 *C	24.60 ± 0.05	g'	43 ± 3	3 ± 1
MEGAb12 *C	24.69 ± 0.05	g'	39 ± 3	25 ± 11
MEGAa10 *g	25.25 ± 0.09	g'	41 ± 5	41 ± 30
MEGAb33 *CV	$25.25 \pm 0.09(0.7)$	g'	44 ± 3	1.1 ± 0.3
MEGAa15 *C	25.41 ± 0.10	g'	45 ± 3	1.0 ± 1.0
MEGAa23 *C	25.59 ± 0.12	g'	41 ± 3	24 ± 11
MEGAa7 *C	25.76 ± 0.14	g'	48 ± 3	1.3 ± 1.3
MEGAa24 *C	25.86 ± 0.16	g'	47 ± 3	12 ± 18
MEGAa31 *CV	$25.86 \pm 0.16(0.7)$	g'	40 ± 3	3 ± 1
MEGAc19 *C	25.92 ± 0.17	g'	41 ± 3	1.2 ± 0.5
MEGAa29 *C	25.93 ± 0.17	g'	41 ± 3	1.3 ± 0.3
MEGAa35 *C	25.99 ± 0.018	g'	39 ± 3	30 ± 14
MEGAa19 *C	26.07 ± 0.19	g'	39 ± 4	38 ± 20
MEGAb29 *C	26.16 ± 0.21	g'	39 ± 5	5 ± 2
MEGAa20 *C	26.19 ± 0.21	g'	44 ± 3	2.1 ± 1.1
MEGAa22 *C	26.24 ± 0.22	g'	45 ± 3	4 ± 2

MEGAa8 *C	26.26 ± 0.23	g’	39 ± 3	8 ± 3
MEGAa14*g	26.35 ± 0.25	g’	41 ± 3	4 ± 12
MEGAa5 *g	26.39 ± 0.25	g’	37 ± 3	15 ± 12
MEGAa12*C	26.42 ± 0.26	g’	42 ± 3	32 ± 15
MEGAa18 C	26.60 ± 0.31	g’	41 ± 3	3 ± 2
MEGAb19 C	26.62 ± 0.31	g’	64 ± 7	76 ± 38
MEGAa1 C	26.68 ± 0.34	g’	36 ± 3	12 ± 5
MEGAc33	27.03 ± 0.45	g’	42 ± 4	15 ± 15
N11033a5 *	22.09 ± 0.015	VR	36 ± 4	33 ± 18
N11033c1 *	22.70 ± 0.03	VR	46 ± 3	1 ± 8
N11033d13 *	24.18 ± 0.24	VR	58 ± 4	2 ± 12
N11033b7 *	24.61 ± 0.16	VR	43 ± 3	3 ± 8
N11033c7 *	24.79 ± 0.19	VR	44 ± 3	2 ± 8
N11033a9 *	24.80 ± 0.19	VR	46 ± 3	1 ± 8
N11033e1*	25.19 ± 0.27	VR	43 ± 3	4 ± 7
N11033c13*	25.20 ± 0.11	VR	44 ± 3	20 ± 12
N11033b1*	25.22 ± 0.28	VR	44 ± 4	1 ± 8
N11033b9	25.282 ± 0.30	VR	45 ± 3	15 ± 10
N11033d1	25.44 ± 0.34	VR	43 ± 3	1 ± 7
N11033a11	25.50 ± 0.37	VR	43 ± 3	25 ± 14
N11033a13	25.51 ± 0.28	VR	45 ± 3	27 ± 14
N11033a1	25.94 ± 0.55	VR	44 ± 3	14 ± 10
N10032W3a5 *	23.52 ± 0.08	VR	39 ± 3	5 ± 6
N10032W3c13 *	23.54 ± 0.08	VR	45 ± 3	1 ± 7
N10032W3b13 *	24.46 ± 0.19	VR	45 ± 3	4 ± 7
N10032W3a11 *	24.52 ± 0.20	VR	44 ± 3	4 ± 7
N10032W3a15 *	24.69 ± 0.23	VR	43 ± 3	1 ± 6

N10032W3b1 *	24.97 ± 0.29	VR	45 ± 3	12 ± 9
N10032W3b15 *	25.04 ± 0.32	VR	44 ± 3	3 ± 7
N10032W3a3 *	25.05 ± 0.32	VR	44 ± 3	1 ± 7
N10032W3a9	26.12 ± 0.86	VR	41 ± 3	17 ± 10
NEP0813NW3a5 *C	23.58 ± 0.06	VR	43 ± 2.5	1.4 ± 0.6
NEP0813NW3a7 *C	24.05 ± 0.10	VR	45 ± 2.6	3 ± 1
NEP0813NW3a1 *C	24.62 ± 0.20	VR	43 ± 2.6	0.8 ± 0.6
NEP0813NW3b7 *C	24.80 ± 0.17	VR	42 ± 2.5	0.6 ± 0.1
NEP0813NW3a11 C	25.17 ± 0.29	VR	45 ± 2.7	8 ± 3
NEP0813NW3a3 C	25.26 ± 0.4	VR	39 ± 2.7	20 ± 8
NEP0815NE3c9 *	22.62 ± 0.02	VR	41 ± 3	0.3 ± 5
NEP0815NE3b15 *	24.06 ± 0.09	VR	43 ± 3	5 ± 6
NEP0815NE3a3 *	24.35 ± 0.12	VR	39 ± 3	25 ± 12
NEP0815NE3a15 *	24.79 ± 0.19	VR	44 ± 3	1 ± 6
NEP0815NE3b9 *	24.83 ± 0.19	VR	47 ± 3	1 ± 7
NEP0815NE3a13 *	24.89 ± 0.21	VR	43 ± 3	16 ± 9
NEP0815NE3a1 *	25.02 ± 0.25	VR	46 ± 3.1	20 ± 11
NEP0815NE3b13 *	25.05 ± 0.23	VR	42 ± 3	5 ± 6
NEP0815NE3a5	25.49 ± 0.36	VR	44 ± 3	6 ± 6

Table 2.4: Detections List. * - object used in likelihood fits. C - object confirmed on second night. g - object fell on chip gap on second night. V- object has variable magnitude. Number in brackets in column 2 is the range of magnitude measurements for the variable objects. Δ is barycentric distance. i is inclination.

Field	Filter	N	N_{50}	alpha	m_o	Reference/Fields
UN	R	9	6	0.34 ± 0.26	22.3 ± 2	UNE,UNW
MEGA	g'	25	21	0.76 ± 0.25	24.5 ± 0.65	MEGA
CTIO01	VR	23	14	0.56 ± 0.25	22.7 ± 1.0	N10032W3, N11033
CTIO02	VR	15	12	0.68 ± 0.31	23.3 ± 1.0	NEP0813NW3, NEP0815NE3
SSU	r	38	20	0.94 ± 0.31	23.4 ± 0.25	*Petit et al.* (2006) Uranus Fields
SSN	r	27	17	1.12 ± 0.38	23.3 ± 0.3	*Petit et al.* (2006) Neptune Fields
G01	r	17	14	0.5*	23*	*Gladman et al.* (2001) CFHT Field
AF	VR	10	10	0.34 ± 0.2	21.4 ± 2.0	*Allen et al.* (2001) AF Field
AKL	VR	8	7	0.78 ± 0.45	23.5 ± 1.0	*Allen et al.* (2001) KL Fields
TE1G	r	15	12	0.56 ± 0.25	23.4 ± 0.5	*Trujillo et al.* (2001) See Appendix E
TE2G	r	7	6	0.44 ± 0.3	23.4 ± 1.0	*Trujillo et al.* (2001) See Appendix E
TE3G	r	12	7	0.74 ± 0.45	23.7 ± 0.4	*Trujillo et al.* (2001) See Appendix E
TE5M	g'	7	5	1.44 ± 0.9	23.4 ± 1.5	*Trujillo et al.* (2001) See Appendix E

Table 2.5: Results of the maximum likelihood fits for all fields fit individually. Uncertainties are taken from the extrema of the 1-sigma likelihood contours. *-Provides a 3-sigma lower limit only. N - Number of objects detected in the field. N_{50} - number of objects brightward of 50 % threshold.

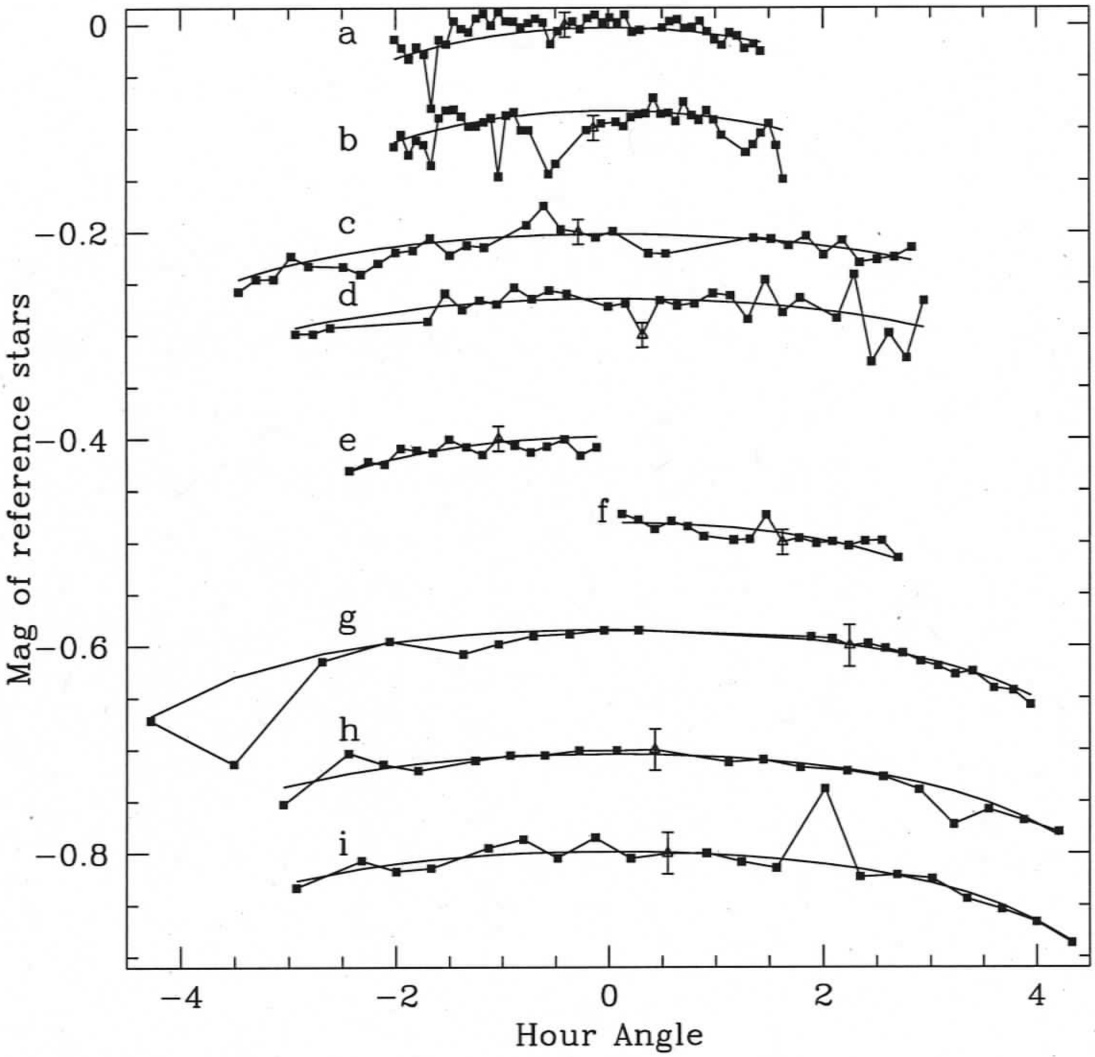

Figure 2.1: Variation of magnitude of reference stars versus hour angle of observations. Smooth line is the magnitude variation with airmass expected from nominal airmass extinction terms reported by the telescopes. The reference image used for planted object magnitude scaling is shown as an open triangle for each night, with a typical uncertainty shown for each point given. Each field is labeled; a: MEGAPrime Night1, b: MEGAPrime Night2, c: N10032W3, d: N11033, e: UNE, f: UNW, g: NEP0813NW3 Night1, h: NEP0815NW3 Night2, i: NEP0815NE3.

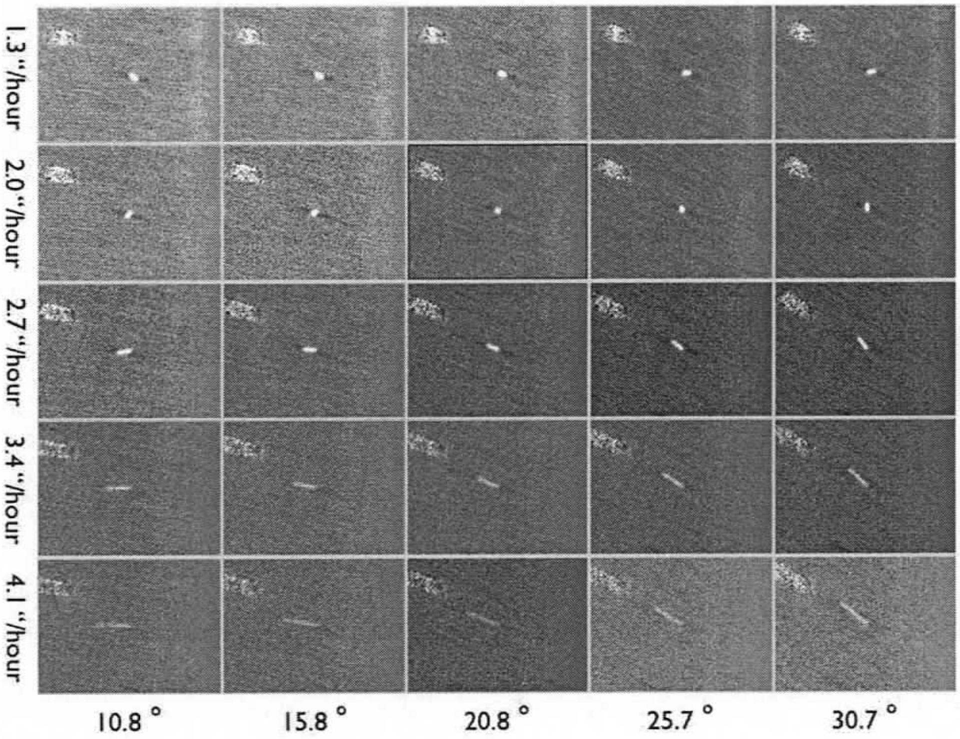

Figure 2.2: Grid of shift rates and angles used to search the MEGAPrime field. Rates are in arcseconds per hour. Angles are in degrees below the horizontal. The source visible in the images is a real 23.8 mag. object with a rate of motion close to 2 arcsec. hr^{-1} at 20.8°, consistent with the ecliptic. The subtraction well and characteristic trailing can be seen at other rates of motion.

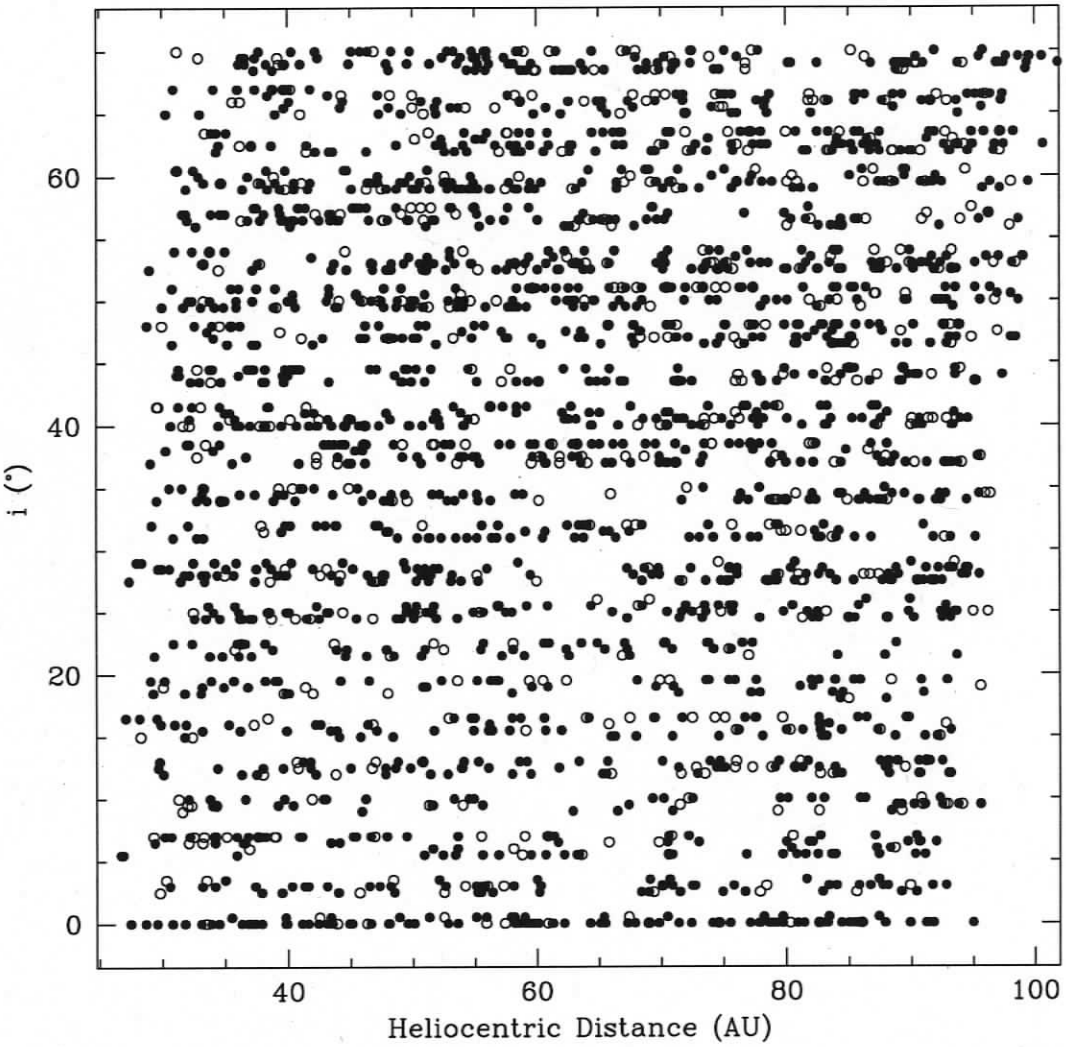

Figure 2.3: Distribution of inclinations and distances for the artificial objects planted in the observations, taken from the planted objects lists of 10 chips in the MEGAPrime field. Solid circles mark those planted objects that were found during the object search. Open circles mark those that were not found. The same magnitude distribution of artificial objects was used at all distances. Thus, for a given magnitude, the detection efficiency did not depend on object distance.

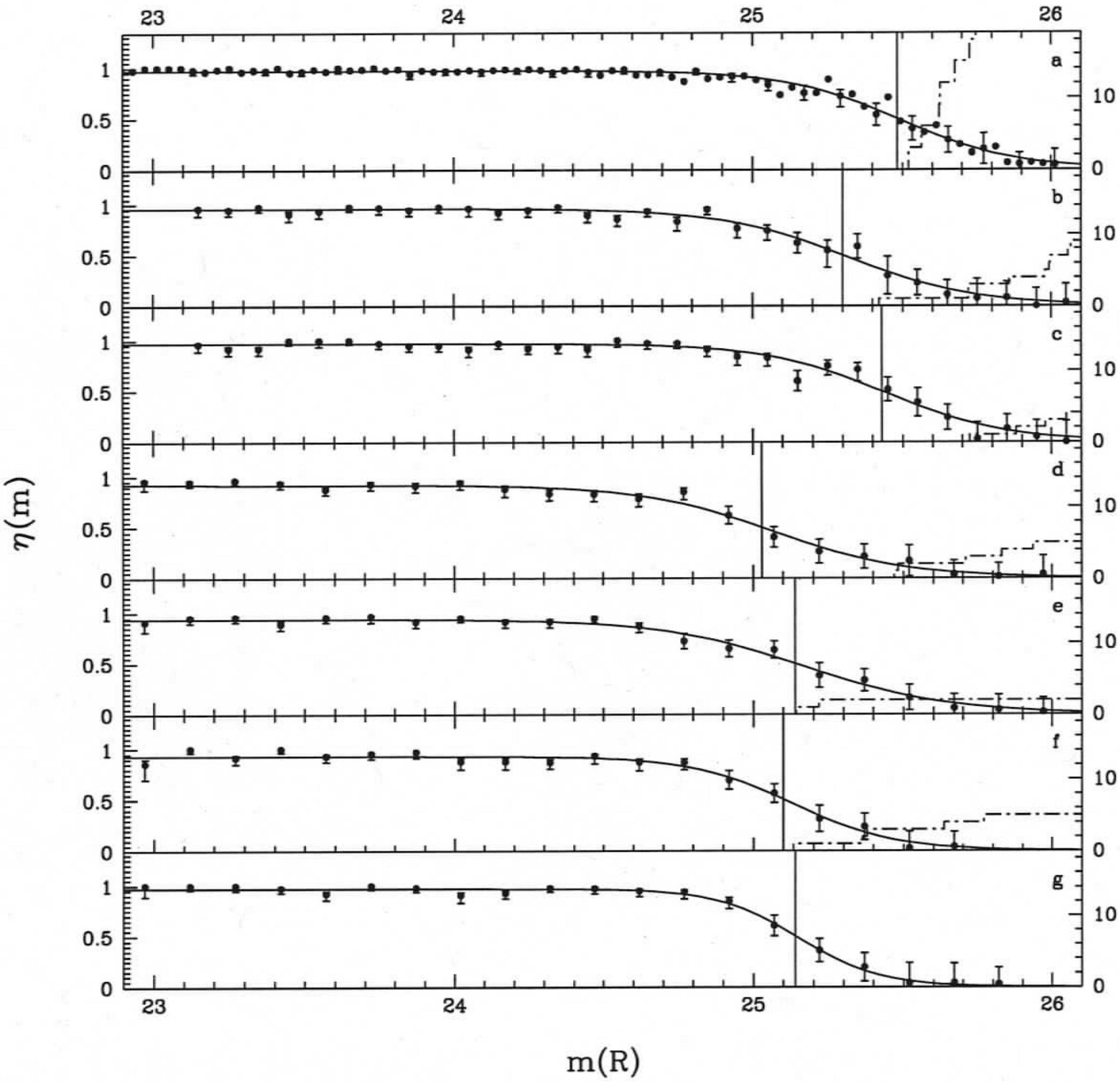

Figure 2.4: Net efficiency for each field with 50% efficiency marked with a vertical line. Magnitudes are converted to R-band using average colours (see Section 2.6). Points are the binned efficiencies determined from the image search. Errorbars are 1-sigma Poisson confidence regions. The solid curve is the best fit efficiency using Eq. 2.2. The dotted curve is a cumulative histogram of visually rejected false candidates. Each field is labeled; a: MEGAPrime N1, b: UNE, c: UNW, d: N10032W3, e: N11033, f: NEP0813NW3, g: NEP0815NE3.

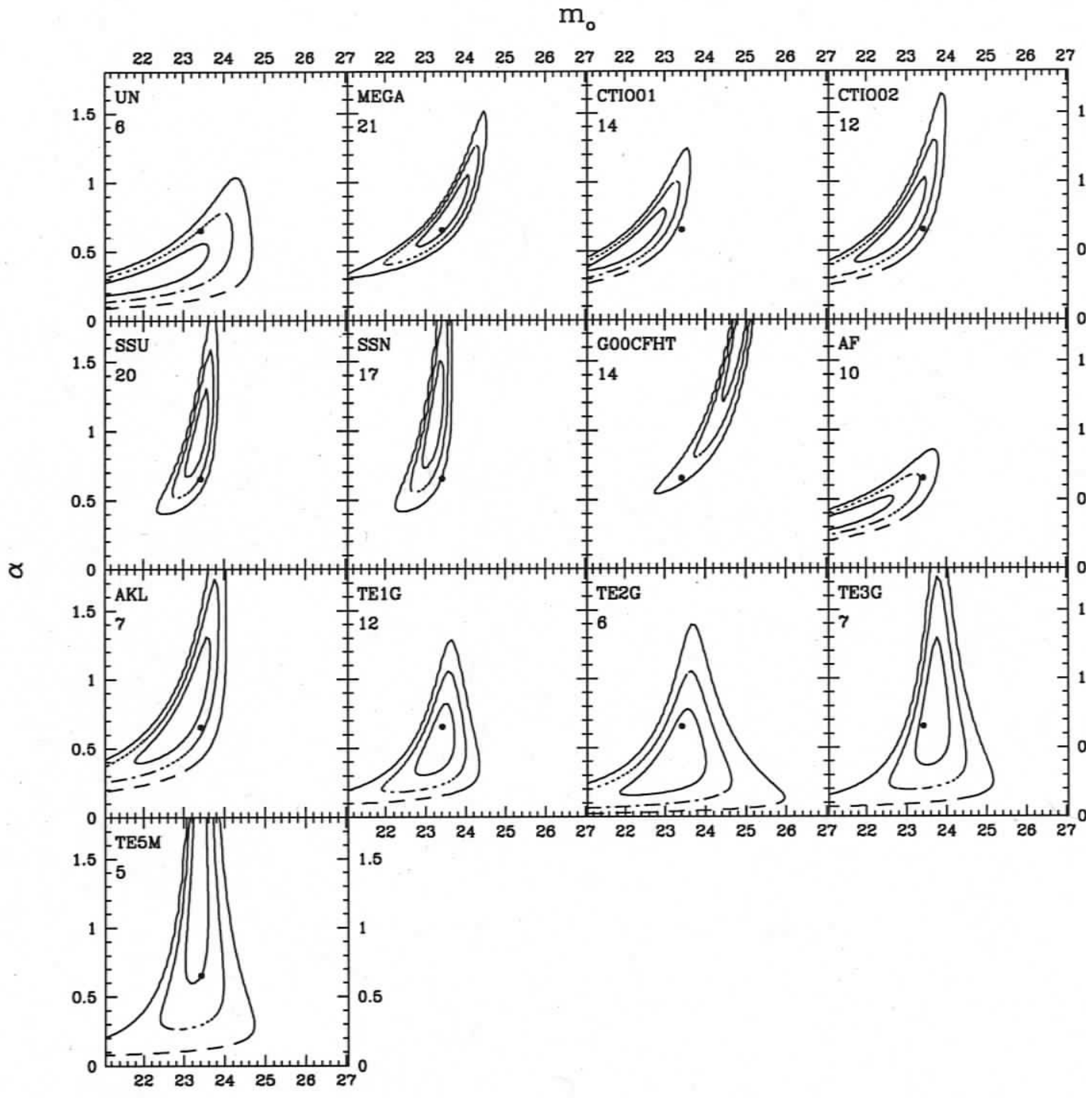

Figure 2.5: Credible regions for the maximum likelihood fits to individual fields with 5 or more detections. Contours have been shifted to R-band using the nominal colours (see Section 2.6). Solid: 1-sigma, Dashed: 2-sigma, Dotted: 3-sigma credibility contours. Field name and number of detections used in fits presented. Point indicates the best fit when combining all data together. Contours indicate m_o is not consistent between surveys unless small shifts in m_o are allowed.

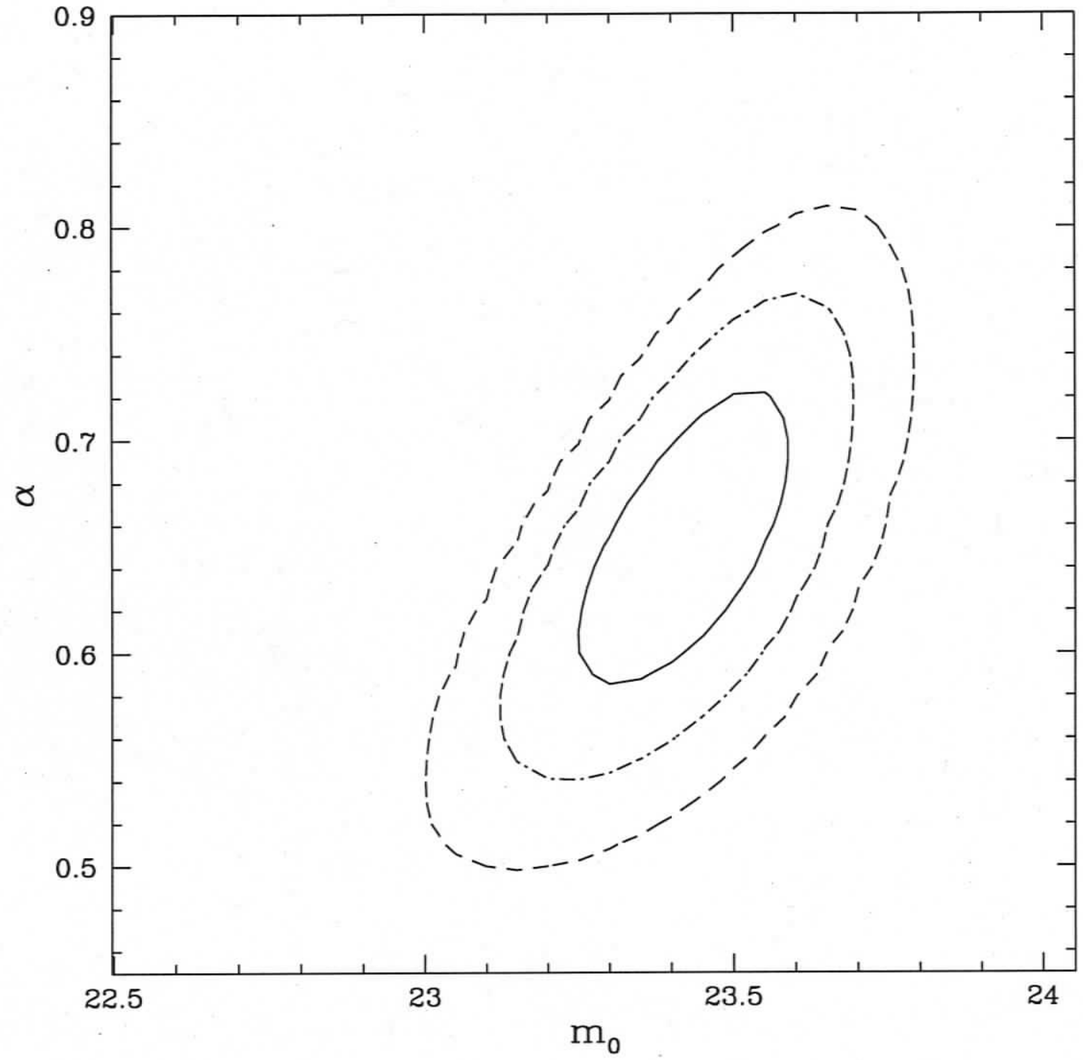

Figure 2.6: 1, 2, and 3-sigma confidence regions for the single power-law maximum likelihood fits using all data. Plotted are the likelihood contours for α and m_o.

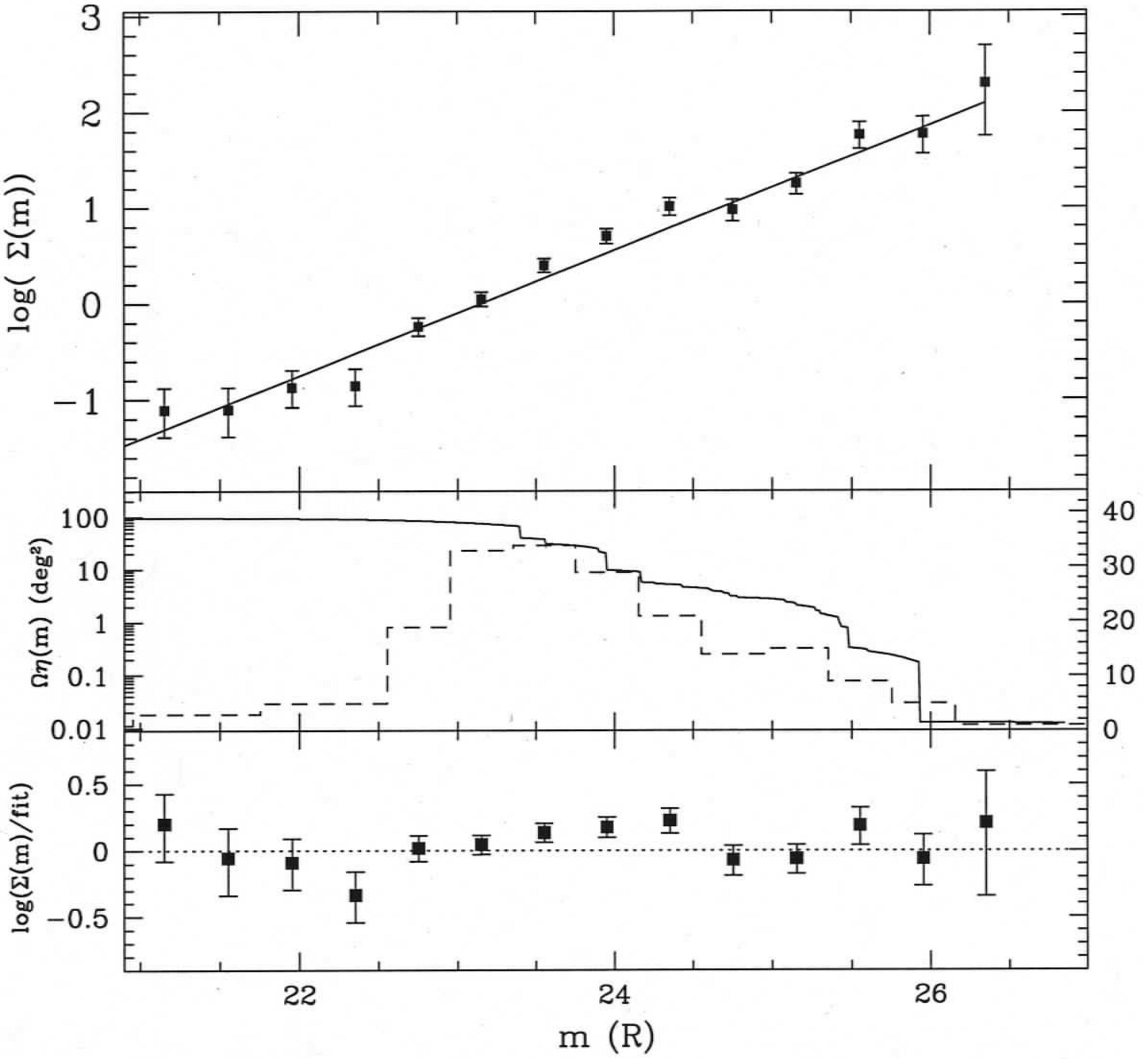

Figure 2.7: *Top:* Histogram of combined data using 0.4 mag bin-widths. Object magnitudes are shifted to R-band using typical magnitude colours. Errorbars are 1-sigma Poisson intervals. Solid straight line: best fit line with $\alpha = 0.65$ and $m_o = 23.42$. *Middle:* Effective area (area times efficiency) of combined data. Dashed line: histogram of all detections using 0.4 mag bin-width. *Bottom:* Log ratio of histogram to best fit $\alpha = 0.65$ and $m_o = 23.42$. Errorbars are 1-sigma Poisson interval.

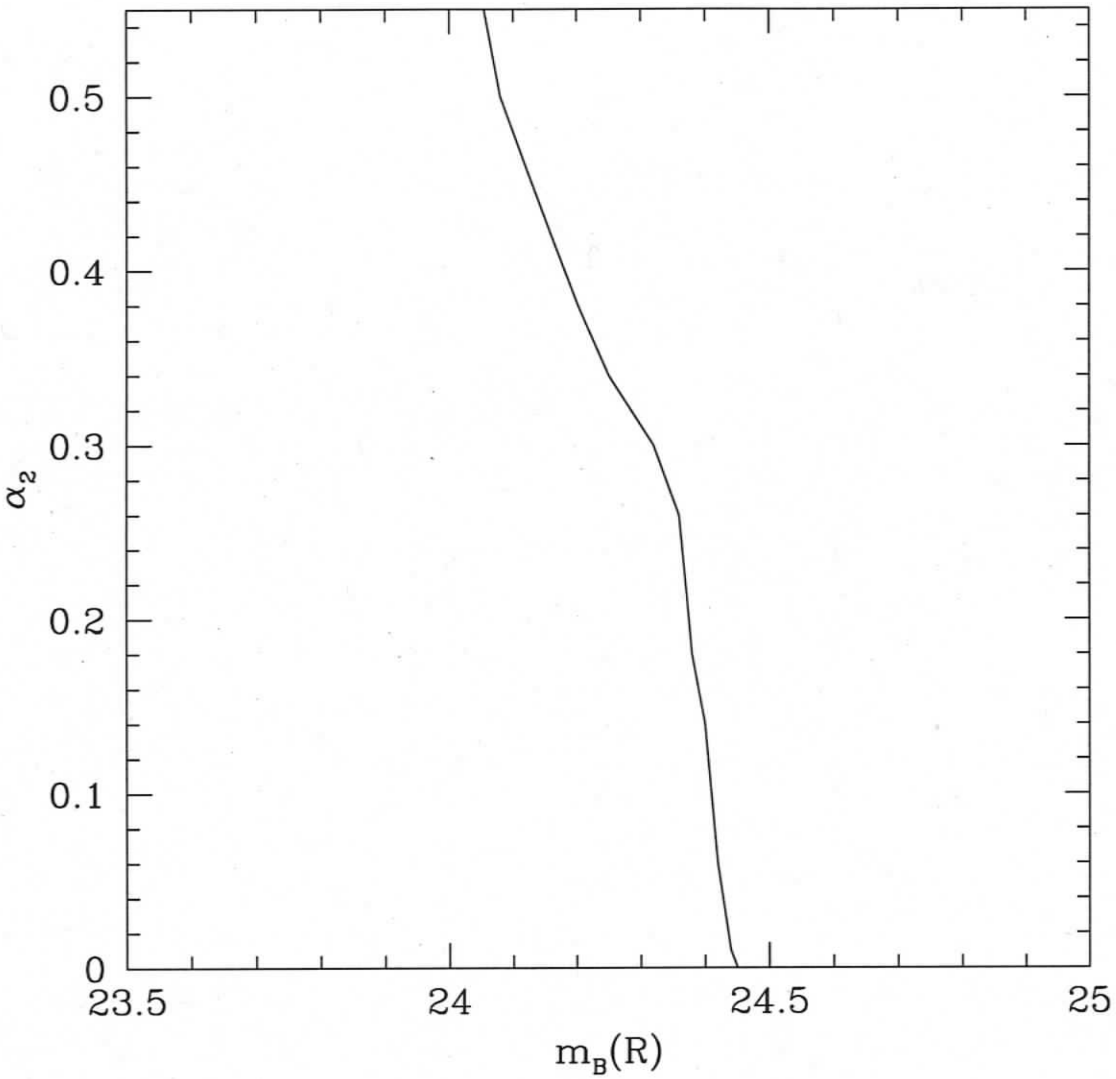

Figure 2.8: Probability of rejection of a broken power-law from the data. Plotted is faint-end slope α_2 versus break magnitude m_B. Contour represents the 95% rejection confidence region. Contour has been smoothed to remove effects of course simulation sampling.

Chapter 3

A Derivation of the Luminosity Function of the Kuiper Belt from a Broken Power-Law Size Distribution

W. C. Fraser, JJ Kavelaars

Based on a manuscript Accepted in Icarus.

Abstract

We have derived a model of the Kuiper belt luminosity function exhibited by a broken power-law size distribution. This model allows direct comparison of the observed luminosity function to the underlying size distribution. We discuss the importance of the radial distribution model in determining the break diameter. We determine a best-fit break-diameter of the Kuiper belt size-distribution of $30 < D_b < 90$ km via a maximum-likelihood fit of our model to the observed luminosity function. We also confirm that the observed luminosity function for $m(R) \sim 21 - 28$ is consistent with a broken power-law size distribution, and exhibits a break at $m(R) = 26.0^{+0.7}_{-1.8}$.

3.1 Introduction

The size distribution (SD) of a belt of planetesimals can provide information on the physical and dynamical properties of those objects. Collisions between belt members causes the SD to evolve over time. Low velocity collisions can cause objects to accrete into larger bodies, while high velocity collisions smash bodies into smaller pieces. A generic outcome of collisional evolution simulations of a belt of planetesimals is a power-law SD with a steep slope for large objects, breaking to a shallower slope at some object diameter. Waves or other shapes can be induced in a size distribution, but the general behavior is that of a broken power-law (*O'Brien and Greenberg* 2003). The location of the transition between the steep and shallow SD slopes (break), as well as the small and large object slopes provides information on the strengths of the colliding bodies, and constrains time-scales of accretion and total mass in the belt region (*Safronov and Zvjagina* 1969, *Dohnanyi* 1969, *Kenyon and Bromley* 2001, *Kenyon* 2002, *Kenyon and Bromley* 2004, *Bottke et al.* 2005)

The SD of the Kuiper belt has been inferred from a measurement of the belt's luminosity function (LF) (see for example *Fraser et al.* 2008, (F08) and references therein). F08 show that for the largest objects in the belt (diameter $D \gtrsim 100$km), the SD is well represented by a power-law $N(D) \propto D^{-q}$ with a slope $q \sim 4.3$.

Kuiper belt surveys designed to measure the Kuiper belt object (KBO) faint-end LF ($m(R) \gtrsim 26$), have found evidence to suggest that the LF deviates from a power-law (*Bernstein et al.* 2004). *Bernstein et al.* (2004) found that a distribution with a steep slope for bright objects, that "rolled over" to a shallow slope for faint objects was necessary to describe the substantial dirth of objects with $m(R) \gtrsim 27$. They concluded that the underlying KBO SD transitions ("breaks") to shallower slopes as predicted from collisional evolution models. Using archival Subaru Suprimecam images, *Fuentes and Holman* (2008) provided a substantial increase in the sample of faint ($m(R) \sim 26$) KBOs and concluded that the luminosity function breaks from a steep to shallow slope at $m(R) \sim 24.3$.

Bernstein et al. (2004) and *Fuentes and Holman* (2008) use analytic functions to represent the shape of the observed LF. These functional forms were not derived from physical or theoretical properties, making infering the underlying KBO SD based on the reported LF difficult. We present here a new functional form of the LF that results from the observation of a belt of planetesimals exhibiting a broken SD. This function provides a direct interpretation of the observed LF in terms of the size and radial distributions.

In Section 3.2, we derive the new functional form. We fit the function to the available observations of the Kuiper belt in Section 3.3, describe what future efforts are necessary to constrain the SD in Section 3.4, briefly discuss implications of the Kuiper belt SD in Section 3.5, and make concluding remarks in Section 3.6..

3.2 Broken Power-Law Derivation

To determine the shape of the LF exhibited from a belt of planetesimals with a given SD, we first consider a number of objects in a sample represented by

$$N \simeq A \int \int R(r) S\left(D\right) dD dr \tag{3.1}$$

where r is heliocentric distance, D is object diameter, and $R(r)$ and $S\left(D\right)$ are the radial and SDs of those objects (number of objects with distance r to $r + dr$ or diameter D to $D + dD$). A is a normalization constant to present the equation in number of objects per square degree. Here we have implicitly assumed that the radial and size distributions are separable.

The magnitude of brightness of an object at a heliocentric distance r in AU, with diameter D in km is well approximated as

$$m = K + 2.5 \log_{10} \left(r^4 D^{-2} \right) \tag{3.2}$$

where, for KBOs we have applied the simplification, $\Delta \sim r$. Setting $K = 18.4$, corresponds to KBOs with 6% albedos when observed at opposition (*Gladman et al.* 2001); implicitly assuming that all objects have similar albedos. The largest object observable at a given distance, r in a survey that is sensitive to source magnitudes between m_{min} and m_{max} has diameter $D_{max} = r^2 10^{(m_{min}-K)/5}$. Similarly, the smallest observable object has diameter $D_{min} = r^2 10^{(m_{max}-K)/5}$.

The cumulative LF of a belt of planetesimals as observed by a particular survey, can be derived from Eq. 3.1 by using the integration limits D_{min} and D_{max}. If we assume $S(D) \propto D^{-q}$, ie. we assume a SD is a power-law with 'slope' q, Eq. 3.1 becomes

$$N\left(< m_{max}\right) = A \int \frac{r^2 R(r)}{1-q} dr \left[10^{\frac{K-m_{min}}{5}(1-q)} - 10^{\frac{K-m_{max}}{5}(1-q)} \right] \tag{3.3}$$

where $q \neq 1$. Setting $\alpha = \frac{q-1}{5}$, $a_1 = A \int \frac{r^2 R(r)}{q-1} dr$, and restricting to the case, $10^{\frac{K-m_{min}}{1-q}} \ll 10^{\frac{K-m_{max}}{1-q}}$, then the cumulative LF can be represented by

$$N\left(m_{max}\right) = a_1 \left(m_{max}\right) 10^{\alpha m_{max}}. \tag{3.4}$$

We consider the case where the SD breaks to a different slope at a particular break size D_b. That is,

$$S(D) \propto \begin{cases} D^{-q_1} & \text{for } D > D_b \\ D^{-q_2} & \text{for } D < D_b. \end{cases} \tag{3.5}$$

If r_1 and r_2 define the inner and outer edges of the belt, then a survey where $D_{min} = r_1^2 10^{(m_{max}-K)/5} > D_b$, the observed LF is given by Eq. 3.4 where the slope $\alpha = \alpha_1 =$

$\frac{q_1-1}{5}$. If however, the survey is sensitive to objects smaller than D_b out to some distance r_b, then Eq. 3.1 becomes

$$N = A\int_{r_1}^{r_b} R(r)\left[\beta\int_{D_{min}}^{D_b} D^{-q_2}dD + \int_{D_b}^{D_{max}} D^{-q_1}dD\right]dr + A\int_{r_b}^{r_2} R(r)\int_{D_{min}}^{D_{max}} D^{-q_1}dDdr \tag{3.6}$$

where β is a scaling factor to ensure that $S(D)$ is piecewise continuous at D_b.

Using Eq. 3.2, the maximum distance r_b a survey is sensitive to the break size D_b, is given by $r_b = D_b^{\frac{1}{2}}10^{(m_{max}-K)/10}$.

The constant β can be solved for by requiring that the number of objects slightly larger than D_b be equal to the number of objects slightly smaller than D_b. That is

$$\beta\int_{D_b-\delta}^{D_b} D^{-q_2}dD = \int_{D_b}^{D_b+\delta} D^{-q_1}dD, \tag{3.7}$$

which gives

$$\beta = D_b^{q_2-q_1}. \tag{3.8}$$

Restricting to the case where $10^{\frac{K-m_{min}}{5}(1-q_1)} \ll 10^{\frac{K-m_{max}}{5}(1-q_1)}$ and $10^{\frac{K-m_{min}}{5}(1-q_1)} \ll 10^{\frac{K-m_{max}}{5}(1-q_2)}$, then the cumulative LF is given by

$$N\left(< m_{max}\right) \simeq b_1 10^{\frac{q_2-1}{5}m_{max}} + b_2 10^{\frac{q_1-1}{5}m_{max}} + b_3\left(m_{max}\right) \tag{3.9}$$

where

$$b_1 = A\int_{r_1}^{D_b^{1/2}10^{(m_{max}-K)/10}} R(r)D_b^{q_2-q_1}\frac{r^{2(1-q_2)}}{q_2-1}dr10^{\frac{-K}{5}(q_2-1)},$$

$$b_2 = A\int_{r_b}^{r_2} R(r)\frac{r^{2(1-q_1)}}{q_1-1}dr10^{\frac{-K}{5}(q_1-1)}$$

and

$$b_3 = A \int_{r_1}^{D_b^{1/2} 10^{(m_{max}-K)/10}} R(r) dr D_b^{1-q_1} \left[\frac{q_2 - q_1}{(q_1 - 1)(q_2 - 1)} \right],$$

where $q_1 \neq 1$ and $q_2 \neq 1$, and A is chosen such that N is the number of objects per square-degree of the sky.

If a survey is deep enough to see objects with diameters $D \leq D_b$ for all r, then the cumulative LF then becomes

$$N(< m_{max}) \simeq c_1 10^{\frac{q_2-1}{5} m_{max}} + c_2 \tag{3.10}$$

where

$$c_1 = A \int_{r_1}^{r_2} R(r) \frac{r^{2(1-q_2)}}{q_2 - 1} D_b^{q_2-q_1} dr 10^{\frac{-K(q_2-1)}{5}}$$

and

$$c_2 = A \int_{r_1}^{r_2} R(r) dr D_b^{1-q_1} \frac{q_2 - q_1}{(1 - q_2)(1 - q_1)}.$$

The cumulative LF of a belt of planetesimals with a two sloped power-law SD is a power-law with slope α_1 for magnitudes brightward of m_1. The roll-over in the LF begins at the brightest magnitude at which objects smaller than D_b can be detected at the inner edge of the belt, r_1. Thus, $m_1 = K + 2.5 log\left(r_1^4 D_b^{-2}\right)$. The LF becomes a power-law again at the magnitude m_2 faint-ward of which, objects larger than the break-size are no longer observed at the outer edge of the belt, r_2. Thus, $m_2 = K + 2.5 log\left(r_2^4 D_b^{-2}\right)$. For magnitudes $m_1 \leq m \leq m_2$, the LF is the sum of nearby objects with $D < D_b$, and distant objects with $D > D_b$. Hence both the radial and size distributions become important as the shape of the LF is determined by the coupling of the two. The functional form of this LF is

$$N\left(<m\right)=A\begin{cases}a_1 10^{\alpha_1 m} & \text{if } m<m_1\\ b_1 10^{\alpha_2 m}+b_2 10^{\alpha_1 m}+b_3\left(m\right) & \text{if } m_1\leq m\leq m_2\\ c_1+c_2 10^{\alpha_2 m} & \text{if } m>m_2.\end{cases}\tag{3.11}$$

Comparing to Eq. 3.9, we see that the SD slopes q_1 and q_2 are related to the LF slopes α_1 and α_2 by $q_1 = 5\alpha_1 + 1$ and $q_2 = 5\alpha_2 + 1$.

The power-law coefficients, a_i, b_i, and c_i, of this function depend on the radial distribution. For the case where a break is observed, knowledge of the true radial distribution is important as the shape of the LF is determined from the coupling of the radial and size distributions. For the case where the break is not seen, the radial distribution is not important as it only affects the LF normalization. The size distribution slopes q_1 and q_2 can be inferred from the LF slopes α_1 and α_2 if the LF has been observed sufficiently brightward and faint-ward of the roll-over.

3.3 Model fit to the Observations

We present here a fit of our model (Eq. 3.11) to the observed KBO LF.

Eq. 3.1 can be evaluated analytically if $R(r) \propto r^{-c}$ where c is the radial distribution 'slope'. While this is likely not the true KBO radial distribution, *Trujillo and Brown* (2001) and *Kavelaars et al.* (2008) have shown that the radial distribution is sharply decreasing beyond $r \sim 40$ AU. A visual examination of Figure. 2 from *Trujillo and Brown* (2001) reveals that $R(r) = \left(\frac{r}{63}\right)^{-10}$ is a good representation of the sharp density fall-off. Such a representation is sufficient to show the importance of accurately modeling the radial distribution when determining the size distribution. The full functional form using this radial distribution is presented in Appendix F.

Fraser et al. (2008) present a fit of the LF for data brightward of $m(R) = 26$. They find that the LF of the Kuiper belt is well described by a single power-law with slope $\alpha = 0.65 \pm 0.05$. To ensure reliability of the fit, they only considered surveys with measured detection efficiencies as a function of magnitude for each field in the survey. In fitting Eq. 3.11 to the observed LF, we adopted the same practices as *Fraser et al.* (2008) listed below:

1. We considered the F08 sample presented by *Fraser et al.* (2008). In addition, we included the survey presented by *Bernstein et al.* (2004, 2006). Note: we did not included the survey presented by *Fuentes and Holman* (2008) as the majority of analysis for this manuscript was complete before the author was aware of that work. This manuscript focuses on the functional form of the LF, and these data, which may improve the constraint on the function parameters, do not change our conclusion that a full understanding of the size distribution requires a rigorous treatment of the radial distribution as well.

2. We offset all magnitudes to R-band using the average KBO colours presented in *Fraser et al.* (2008).

3. We cull from each survey all sources faintward of the 50% detection efficiency of that survey, and set the detection efficiency to zero faintward of that point.

4. We fit the differential LF, $\Sigma(m) = \frac{dN(<m)}{dm}$ using a maximum likelihood technique.

5. We adopted a form of the likelihood equation as derived by *Loredo* (2004), and extended to account for sky density variations, A_k, and color variations, C_k (see *Fraser et al.* 2008, for details). We adopted the same prior ranges of the colour offsets and range of normalization parameters as presented in *Fraser et al.* (2008) (± 0.2 for the colour parameters, and ± 0.4 for the normalization parameters).

To evaluate Eq. 3.11, we require a set of radial distribution parameters, $r_1, r_2, \gamma = (1-c)/10$. We set the Kuiper belt inner edge as $r_1 = 35$ AU. For a baseline model, we consider an outer edge $r_2 = 60$ AU with the radial fall-off parameter, $c = 10$ (see previous discussion). This provides a reasonable representation of the steep fall-off in the Kuiper belt radial distribution and typical outer limit to the objects detected in the F08b sample. We also consider two test cases; in model 2 we set $r_2 = 100$ AU, and in model 3, we set the radial fall-off parameter, c, to that of the minimum-mass solar nebula, $c = 3/2$ (*Hayashi* 1981) corresponding to $\gamma = -0.05$. Models 2 and 3 were chosen to evaluate the effects of the radial distribution parameters on the fit results. We speculate that the value of r_2 for any reasonable choice, will have no strong effect on the fit parameters as most objects are detected at distances less than ~ 45 AU.

Using our maximum likelihood technique, we determined the best-fit LF parameters of Eq. 3.11 using the baseline model, as well as models 2 and 3. These are presented in Table 3.1. The observations were best-fit with $\alpha_1 = 0.69 \pm 0.07$, $D_b = 37^{+50}_{-10}$ km, $\alpha_2 = -0.4^{+0.8}_{-3}$ for our baseline model.

We found that the best-fit α_1 and D_b, $D_b = 37^{+50}_{-10}$ km and $\alpha_1 = 0.69 \pm 0.07$, are not dependent on the choice of radial distribution models. As demonstrated in Eqs. 3.3 and 3.9, the radial distribution has no effect on the apparent bright object slope and the break diameter depends only on the choice r_1. Thus, because the same data was always used, and because we set $r_1 = 35$ AU for all choices of radial distribution, the best-fit α_1 and D_b *should* be the same for all radial distributions considered.

We found very different behaviors for the faint-end slope from our two choices of γ. The best-fit α_2 was found to be $-0.4^{+0.8}_{-3}$, $-0.4^{+0.8}_{-3}$, and $-\infty$ for the baseline model $(r_1, r_2, \gamma) = (35, 60, -0.9)$, Model 2 $(r_1, r_2, \gamma) = (35, 100, -0.9)$, and Model 3 $(r_1, r_2, \gamma) = (35, 100, -0.05)$ respectively.

With $\gamma = -0.05$ $(c = 3/2)$, we found that the observations were best-fit with a

SD in which there is a complete absence of objects, ($\alpha_2 = -\infty$) smaller than break diameter, $D_b \sim 40$ km. When $\gamma = -0.9$ ($c = 10$), the best-fit faint end slope was $\alpha = -0.4$. These two behaviors are expected; a sharp roll-over in the LF can be the result of a very sharp roll-over in the SD with a gradual fall-off in the radial distribution, or a less sharp roll-over in the SD and a steep fall-off in the radial distribution. Setting $c = 3/2$ does not correctly model the very sharp radial fall-off in the Kuiper belt and thus it is unlikely that there is a complete absence of objects smaller than $\sim D_b$. We discard model 3 as this is an unlikely model of the radial and size distributions. We do note however, that no KBOs smaller than $D \sim 30$ km have yet been detected.

We found no difference in the best-fit parameters when r_2 was varied (see the baseline model and model 2). This demonstrates the expected lack of influence of this parameter on the fits.

A series of Monte-Carlo simulations were performed in which a sample of detections representative of the surveys and detections in the F08 sample were generated from a model Kuiper belt. Each simulated data-set was fit using the maximum likelihood technique, and on average, the fitting routine reproduced the input model parameters. The same behavior was found for the fits of the simulated observations, as for the real observations. That is, the best-fit faint-end slope, α_2, depended on our choice of γ, and the best-fit break diameter, D_b, depended on our choice of r_1. The reported best-fit values were correct however, if the chosen γ and r_1 were within a factor of 2 the correct value. Thus we feel that our likelihood method presented here produces satisfactory results to within the accuracy of the fit to the data currently available.

All minimizations have the same maximum likelihood value to within a few percent. Thus there is no preference, in a statistical sense, to choose one model over another; each is equally sufficient to describe the observations. Thus, we take

take the baseline model, with $(r_1, r_2, \gamma) = (35, 60, -0.9)$ and $(\log A, \alpha_1, \alpha_2, D_b) = (22.82, 0.69, -0.4, 37)$ as the best model, as the baseline model radial distribution is the most similar of the three considered, to that observed for the Kuiper belt.

The differential LFs (derivative of Eq. 3.11 wrt. m) using the best-fit parameters for all choices in radial distribution are presented in Fig. 3.1. To produce the histogram, object magnitudes and the areas of each survey have been adjusted using the best-fit C_k and A_k parameters (see F08 for details). These parameter values were determined by maximizing the likelihood while holding the LF parameters to their best-fit values, and are presented in Table 3.2. The histogram is presented in order to visualize the observations, but was never used in the fitting procedure. As can be seen, a very sharp roll-over is apparent for magnitudes faint-ward of $m(R) \sim 26$. This plot provides visual confirmation that the fit describes the data reasonably well.

The likelihood contours of the best-fit LF for our choice in baseline radial distribution is presented in Fig. 3.2. As can be seen, α_1 and A and α_2 and D_b are highly correlated. The uncertainties of the best-fit parameters in Table 3.1 are the extrema of the 67% bayesian credible regions.

The best-fit large object slope and break diameter, $q_1 = 4.45 \pm 0.35$ and $Db = 37^{+50}_{-10}$, are consistent with (*Fraser et al.* 2008) who found that $q = 4.25 \pm 0.75$ for objects larger than $D \sim 50$ km.

3.4 Sources of Uncertainty

The best-fit LF we present assumes that the lack of faint KBOs observed by *Bernstein et al.* (2004) and *Fuentes and Holman* (2008) is caused by a break in the SD, and suggests that the break observed must occur at diameter $27 < D_b < 87$. This result however assumes that an R-albedo of 6% is typical of KBOs. Recent observations suggest that this is true for objects $D \lesssim 500$ km, but objects with $D \gtrsim 1000$ km have albedos $\sim 60 - 90\%$ (*Grundy et al.* 2005, *Stansberry et al.* 2007). *Fraser et al.* (2008)

has shown however, that the trend of lower albedos for smaller objects would produce a *steeper* LF than otherwise would be observed for constant albedos. Thus, albedo effects are likely not the source of the observed break. In addition, *Fraser et al.* (2008) found that a variation of albedo with distance has no effect on the inferred LF slopes, and only the LF normalization.

We also assume that the size distribution is the same at all distances. If this is not true, it would have similar affects as assuming constant albedos for all sizes. That is, the slope inferred under the assumption that the size distribution is distance dependent could be steeper or shallower than the true slope depending on the trend of size with distance. This effect cannot be tested without substantially more observations than currently available. This effect however, is likely negligible, as KBOs have excited orbits. Thus interactions (collisions) between objects occur over a range of many tens of AU which would cause the size distribution to be similar over the full range of the Kuiper belt.

The LF also assumes that the break in the SD is sharp. That is, there is no size range over which the SD slope transitions from q_1 to q_2. While this is certainly not true, simulations of accretion and collisional processing in a belt of planetesimals show that the transition occurs over a small range of sizes compared to the range over which the SD exhibits a power-law like behavior (*Kenyon* 2002). Additionally, the lack of surveys sensitive to KBOs with $m(R) > 27$ from which the roll-over shape is constrained implies a more complicated description is not warranted. More survey data is needed that covers a few square degrees in the range $m(R) \sim 26 - 28$ to accurately constrain the break magnitude; a large number ($N \sim 20$) of detected objects with a range of magnitudes beyond the break are necessary to constrain the faint end slope, without which the break diameter determination remains uncertain.

The SD inferred from the LF is still model dependent, and determining the structure of the SD reliably from the LF requires improved knowledge of the properties of the Kuiper belt (albedo, radial distribution, etc.). A large source of uncertainty stems from the current lack of knowledge of the KBO radial distribution. Each survey considered in this analysis sampled the Kuiper belt at different locations on the sky. Variations in the sky density between surveys, requires treating sky density parameters as nuisance parameters for each individual field (*Fraser et al.* 2008). This causes the range of parameter values consistent with the observations to be grossly enlarged. An accurate Kuiper belt model which provides the instantaneous radial distribution as a function of latitude and longitude is needed such that density estimates and the coefficients of Eq. 3.11 can be calculated as a function of latitude and longitude. This would remove the need for treating sky densities as nuisance parameters, and would greatly reduce the uncertainty in the inferred SD.

3.5 Discussion

Our results have demonstrated that the size distribution of the Kuiper belt can be described by three size distribution parameters, q_1, q_2, and D_b, and that, to accurately measure the break-slope q_2 requires that the radial distribution be accounted for in a way which removes the ambiguity between source brightness and source size. We have found that $q_1 \sim 4$, $q_2 \sim -1$, and $D_b \sim 40$ km.

As in previous works, we have found that the observed large object slope, $q_1 \sim 4$ (*Trujillo et al.* 2001, *Gladman et al.* 2001, *Bernstein et al.* 2004, *Petit et al.* 2006, *Fraser et al.* 2008), is inconsistent with the $q \sim 3.5$ slope expected from a steady-state collisional cascade (*Dohnanyi* 1969, *O'Brien and Greenberg* 2003, *Pan and Sari* 2005). Rather, the slope is consistent with the large object slope produced from accretionary processes (*Safronov and Zvjagina* 1969, *Kenyon and Bromley* 2001, *Kenyon* 2002).

Various accretion and collisional models exist that can reproduce some of the observed features of the size distribution, ie. the correct small object slope, or break diameter. But to this date, none can simultaneously reproduce q_1, q_2, and D_b. For instance, *Pan and Sari* (2005) present a collisional model in which the accretion size distribution breaks to one in a state of collisional equilibrium. They demonstrate that a break diameter consistent with our results could occur if collisional disruption occurred for timescales $\sim 1-4$ Gyr. The equilibrium slope they considered ($q_2 \sim 3$) however, is inconsistent with the small object slope of our baseline model. The assumption *Pan and Sari* (2005) make, that the size distribution immediately breaks from an accretionary slope to collisional equilibrium is likely incorrect, as there is likely a range of sizes over which disruptions by the more numerous smaller objects have significantly depleted the population, but which have not been replenished with fragments from larger object disruptions. This transition range is seen in more complicated accretion models (*Kenyon and Bromley* 2001, *Bottke et al.* 2005).

In early times of the accretion simulations of *Kenyon and Bromley* (2001), *Kenyon* (2002), steep large object slopes, $q_1 \sim 4$ are produced. For times longer than ~ 70 Myr (~ 1 Gyr for weak bodies), the slope rapidly evolves to a shallower slope inconsistent with our findings. This suggests that accretion in the primordial Kuiper belt was a short-lived process which must have been 'turned off' by some process - likely the dynamical excitation of the belt by some scattering process, such as gravitational stirring from a migrating or scattering Neptune (*Malhotra* 1993, *Thommes et al.* 2002, *Levison and Morbidelli* 2003) or a rogue planet (*Gladman and Chan* 2006). These simulations also produce a break diameter, $D_b \sim 10$ km - only moderately consistent with our results. *Kenyon and Bromley* (2004) found that, with gravitational stirring from Neptune, after 4.5 Gyr, 'weak' KBOs - that is, bodies with collisional strengths lower than expected from icy planetesimals - exhibited a roll-over at break diameters as large as $D_b \sim 30$ km, consistent with that found here. In addition, there simulations produced small object slopes consistent with our findings, but produced a large object slope which is too shallow compared to the observed slope.

The models studied by *Kenyon and Bromley* (2001), *Kenyon* (2002), *Kenyon and*

Bromley (2004) have suggest that KBOs are effectively strengthless, gravitationally bound rubble-piles. These models however, cannot simultaneously produce both the large object and small object slopes; either the evolution is short enough such that the steep accretion slope is maintained, or the evolution is long enough such that a large enough break, and shallow enough small object slope are produced. This is not a surprise however, as it is apparent that the Kuiper belt history is not as quiescent as that considered in these models. The highly excited KBO orbital distribution cannot be produced by in-situ formation. Some large-scale scattering event is needed. Thus, the correct dynamical history must be determined before reliable conclusions can be drawn about the accretion/disruption history, and strengths of KBOs.

3.6 Conclusions

We have developed a model of an LF exhibited from a planetesimal belt with a broken power-law SD. This model allows a direct interpretation of the observed LF in terms of the underlying SD assuming a broken power-law shape. We fit this model to the observed Kuiper belt LF and the break first observed by *Bernstein et al.* (2004). The best-fit parameters are presented in Table 3.1. We find that the break in the SD must occur at diameters $27 - 87$ km ($m(R) \sim 25.8$) for reasonable choices of the radial distribution. We have demonstrated that the inference of the SD from the LF requires an accurate model of the radial distribution. Additional detections of KBOs faintward of $m(R) = 26$, and a proper treatment of the KBO orbital distribution are required to provide an accurate measure of the break size and faint-end slope.

3.7 Acknowledgements

The authors would like to thank the reviewers for their helpful comments which patched a few holes in the original manuscript not recognized by the authors. A special thanks goes to Doug Johnstone for his very careful read through of this manuscript. This project was funded by the National Science and Engineering Research Council and the National Research Council of Canada. This research used the facilities of the Canadian Astronomy Data Centre operated by the National Research Council of Canada with the support of the Canadian Space Agency.

Table 3.1: Maximum Likelihood Parameters. The bright and faint object slopes α_1, α_2, the break diameter D_b, and the normalization constant A were fit by the maximum likelihood routine. Belt edges r_1 and r_2 as well as the radial fall-off parameter γ are fixed parameters not fit by the maximum likelihood routine. Fit 1 represents our baseline model, as the chosen radial distribution best matches that of the Kuiper belt. Fits 2 and 3 have different values of r_2 and γ respectively, chosen to determine the sensitivity of different choices in radial distribution models on the measured LF parameters. Note: $\gamma = -0.05$ produces physical implausible results. ie. $\alpha_2 = -\infty$.

Parameter	Baseline Model	Model 2	Model 3
r_1	35.0	35.0	35.0
r_2	60.0	100.0	100.0
γ	-0.9	-0.9	-0.05
$\log A$	22.8 ± 0.6	22.8 ± 0.6	9.3 ± 0.6
α_1	0.69 ± 0.07	0.69 ± 0.07	0.69 ± 0.07
α_2	$-0.4^{+0.8}_{-3}$	$-0.4^{+0.8}_{-3}$	$-\infty$
D_b (km)	37^{+50}_{-10}	37^{+50}_{-10}	37^{+50}_{-10}

Field	$\log A_k$	C_k	Source
UN	22.6	0.0	*Fraser et al.* (2008)
MEGA	23.0	-0.15	*Fraser et al.* (2008)
CTIO01	23.2	0.1	*Fraser et al.* (2008)
CTIO02	23.1	0.05	*Fraser et al.* (2008)
SSU	23.0	0.0	*Petit et al.* (2006)
SSN	23.1	0.03	*Petit et al.* (2006)
G01	22.9	-0.01	*Gladman et al.* (2001)
AF	23.0	0.0	*Allen et al.* (2002)
AKL	23.2	0.0	*Allen et al.* (2002)
TE1G	22.8	0.0	*Trujillo et al.* (2001) (see *Fraser et al.* (2008))
TE2G	22.8	0.0	*Trujillo et al.* (2001) (see *Fraser et al.* (2008))
TE3G	22.7	0.0	*Trujillo et al.* (2001) (see *Fraser et al.* (2008))
TE5M	22.8	0.2	*Trujillo et al.* (2001) (see *Fraser et al.* (2008))
Bern	22.7	-0.2	*Bernstein et al.* (2004)
KeckV	22.6	0.2	*Chiang and Brown* (1999)
JLT98	22.5	-0.2	*Jewitt et al.* (1998)
G98UH	22.4	-0.1	*Gladman et al.* (1998)
G98Palomar	23.2	-0.03	*Gladman et al.* (1998)
TE1M	22.8	0.13	*Trujillo et al.* (2001) (see *Fraser et al.* (2008))
TE3M	22.9	0.19	*Trujillo et al.* (2001) (see *Fraser et al.* (2008))
TE4G	22.8	0.0	*Trujillo et al.* (2001) (see *Fraser et al.* (2008))
TE4M	22.7	0.05	*Trujillo et al.* (2001) (see *Fraser et al.* (2008))
AB	22.9	-0.11	*Allen et al.* (2002)
AD	22.8	0.0	*Allen et al.* (2002)
AE	22.9	0.0	*Allen et al.* (2002)
AG	22.5	0.0	*Allen et al.* (2002)

AJ	22.8	0.08	*Allen et al.* (2002)

Table 3.2: Best-fit normalization parameters A_k and colour off-set parameters C_k for each field as defined in *Fraser et al.* (2008). These are treated as nuisance parameters and are marginalized when determining the best-fit LF (see Section 3.3). For this table, and Fig. 3.1, these best-fit parameter values are determined from the maximum likelihood routine when the LF parameters are set to their best-fit values (Fit 1 from Table. 3.1).

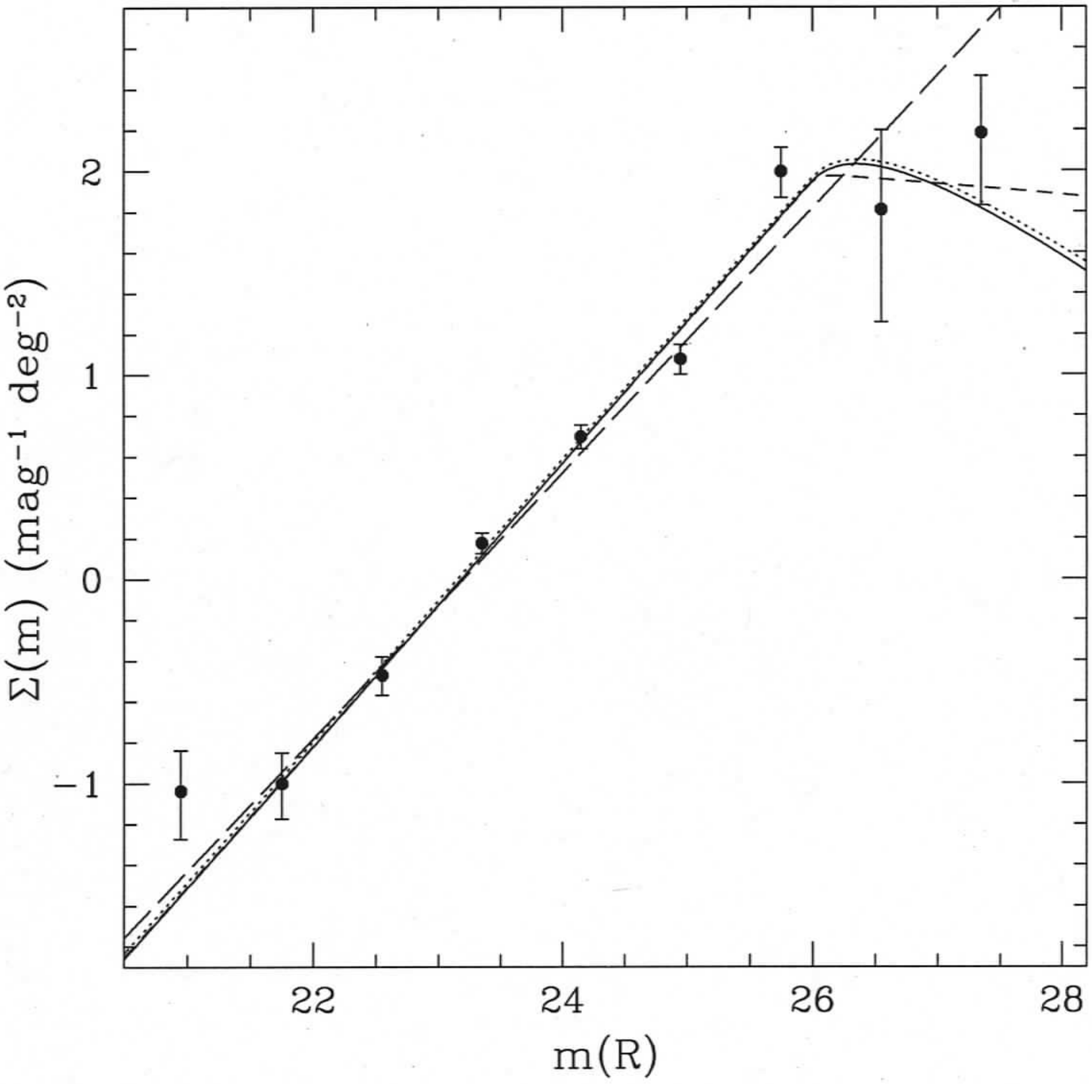

Figure 3.1: Differential surface density histogram of data from the F08 sample and *Bernstein et al.* (2004) using 0.8 mag bin-widths. Objects magnitudes have been shifted using the best fit colour offsets C_k, and observed sky densities have been adjusted using the normalization values A_k taken from Table 3.2. Dashed straight line: best fit power-law with $\alpha = 0.65$ and $m_R = 23.42$ taken from *Fraser et al.* (2008). Solid curve: Model 1 (baseline model), dotted curve: Model 2, and dashed curve: Model 3. The baseline model has the radial distribution which best represents that of the Kuiper belt. Models 2 and 3 test the sensitivity of the fit to different radial distributions. Parameters listed in Table 3.1. As can be seen, a strong break is seen in the LF, as a deviation from the power-law behavior faint-ward of $m(R) \sim 25.8$. The shape of the binned LF is highly sensitive to the choice of bin boundaries and readers are cautioned from drawing conclusions based on such representations. We present the observations in this form only to demonstrate visually the generally correct shape of the LF as derived from our model SD.

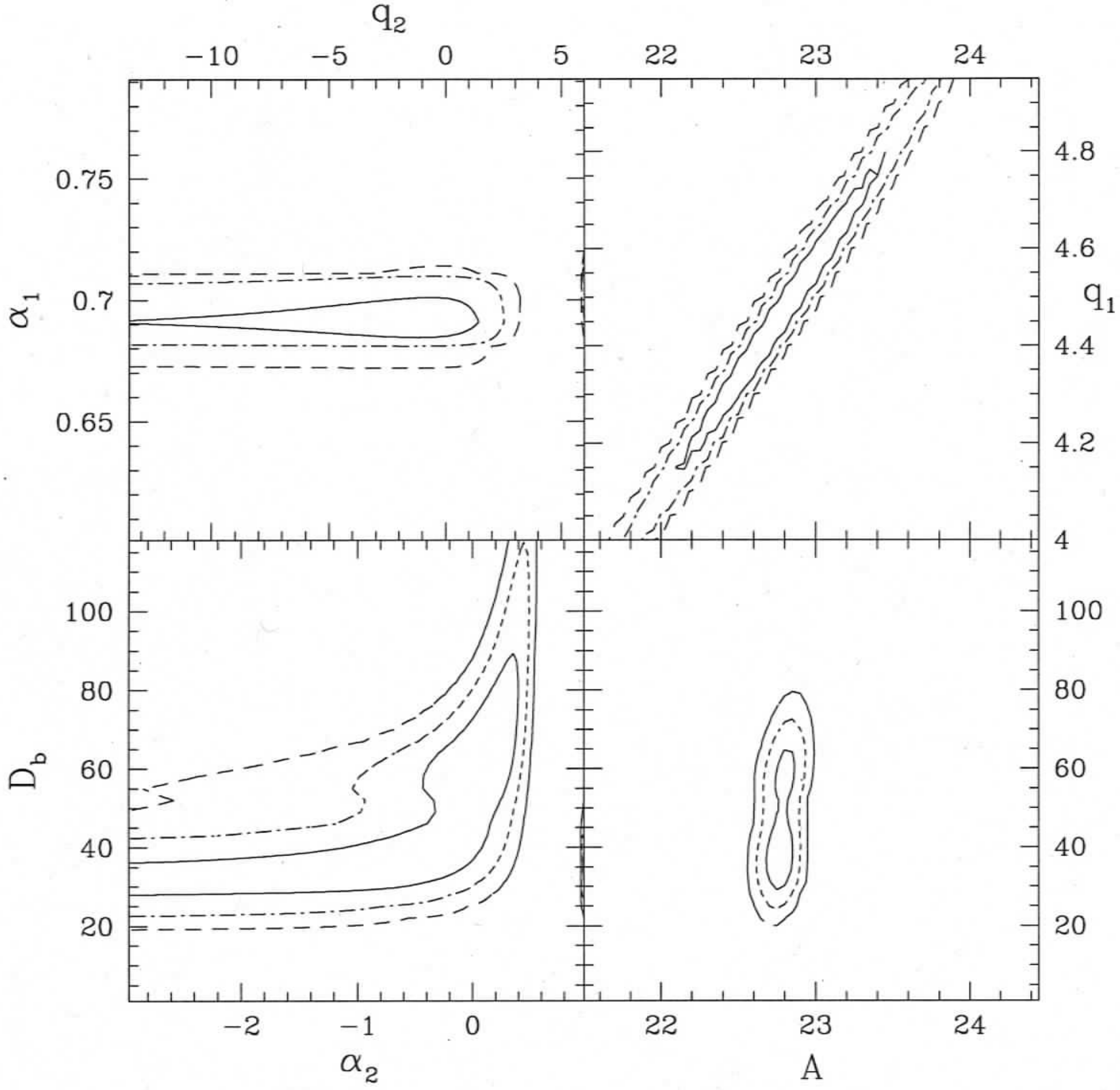

Figure 3.2: 1, 2, and 3-sigma likelihood contours for pairs of bright and faint object slopes α_1, and α_2 (or equivalently large and small object size distribution slopes q_1 and q_2), break diameter D_b (assuming 6% albedos), and normalization parameter $\log A$. Contours for parameter pairs were generated with the other pair of parameters set to their best-fit values.

Chapter 4

The Size Distribution of Kuiper belt objects for $D \gtrsim 10$ km

W. C. Fraser, JJ Kavelaars

Based on manuscript submitted to the Astronomical Journal

Abstract

We have performed a survey of the Kuiper covering $\sim 1/3$ a square degree of the sky using Suprime-cam on the Subaru telescope, to a limiting magnitude of $m_{50}(R) \sim 26.8$ and have found 36 new KBOs. We have confirmed that the luminosity function of the Kuiper belt must break as previously observed (Bernstein et al. 2004; Fuentes & Holman 2008). We find that the luminosity function is consistent with that observed from a size distribution with large object power-law slope $q_1 \sim 4.8$ that breaks to a slope $q_2 \sim 1.9$ at object diameter $D_b \sim 60$ km assuming 6% albedos. We have found no conclusive evidence that the size distribution of KBOs with inclinations $i < 5$ is different than that of those with $i > 5$. We discuss implications of this measurement for early accretion in the outer solar system and Neptune migration scenarios.

4.1 Introduction

The Kuiper belt is a population of planetesimals with diameters as large as a few thousand kilometers (*Brown et al.* 2006) and a mass of approximately a few $0.01 M_\oplus$

(*Gladman et al.* 2001, *Bernstein et al.* 2004, *Fuentes and Holman* 2008). The state of the belt is enigmatic, as such large objects are not likely to form in such a low mass Kuiper belt, over the age of the solar system (*Kenyon and Bromley* 2001). Rather, it is likely that a much more massive initial belt underwent accretion for a time before some large-scale mass-depletion event occurred, such as a stellar passage (*Ida et al.* 2000, *Levison et al.* 2004), a sweep through of the mean-motion resonances of Neptune (*Levison et al.* 2008), or the scattering of KBOs by rogue planets (*Gladman and Chan* 2006). Whatever the event, it is also responsible, at least in part, for the dynamically excited orbits of KBO populations such as the plutinos or the scattering population (*Gladman et al.* 2008).

The size distribution of the Kuiper belt contains a fossil record of the end-state of the accretion processes that occurred in that region. Knowledge of the size distribution can constrain disruption strengths of the bodies, formation time-scales in the outer solar system, and the early conditions of the proto-planetary disk. This makes the determination of the size distribution a primary constraint on Kuiper belt formation scenarios.

Because of the large distance to the Kuiper belt, the size distribution is not determined directly, but rather, is inferred from the shape of the observed luminosity function (LF). Early observations determined that the LF for bright objects ($m(R) \lesssim 26$) was well represented by a power-law with a logarithmic slope $\alpha \sim 0.7$ (*Jewitt et al.* 1998, *Gladman et al.* 1998, 2001, *Allen et al.* 2002, *Petit et al.* 2006, *Fraser et al.* 2008). This suggests that the size distribution of KBOs is a power-law with logarithmic slope $q \sim 4.5$. The deepest survey of KBOs on the ecliptic, presented by *Bernstein et al.* (2004), found a derth of faint objects demonstrating that the LF must "roll-over" or break to a shallower slope at $m(R) \lesssim 27$ (*Bernstein et al.* 2004). Interpreting the roll-over in terms of the Kuiper belt size distribution implies that the large-object power-law size distribution breaks at a KBO diameter $D_b \sim 100$ km assuming 6% albedos. Models of accretion in the outer solar system predicted such a break at least an order of magnitude smaller (*Kenyon and Bromley* 2001, *Kenyon* 2002).

The goal of our work was to confirm the results of *Bernstein et al.* (2004), and accurately measure the shape of the LF at and beyond the roll-over magnitude. From this, the shape of the under-lying KBO size distribution can be inferred. We present here a survey of the ecliptic with limiting magnitude $m(R) \sim 27$, and use this along with previous observations to determine the shape of the LF. In section 2 we present our observations and in section 3 we present our survey results. In sections 4 and 5 we consider past ecliptic Kuiper belt surveys and consider various LF functional forms. In sections 6 and 7 we present our analysis and a discussion of the results.

4.2 Observations, image processing, and characterization

New observations were made in service mode with Suprime-Cam on the Subaru 8.2 m telescope (*Miyazaki et al.* 2002b). Suprime-cam is a 10 chip mosaic CCD camera with a 34'×27' field-of-view (FOV) and a $0''.202$ pixel scale. Observations were made in the r-band on the nights of April 22nd (night 1), and May 8th (night 2) 2008. The same target field was observed each night, targeting the ecliptic with coordinates $\alpha = 13^h46^m57^s.7$, $\delta = -10^o44'00''$. Additionally, each night, a photometric reference image was taken of the Canada-France-Hawaii Supernova Legacy Survey D2 field (*Astier et al.* 2006). Details of the observations are presented in Table 4.1. Presented in Figure 4.1 is a summary of the image quality of both nights; as can be seen, the nights were photometric.

Here we quickly describe our image processing techniques and subsequent moving object search for these data. A more thorough discussion of these techniques can be found in our previous work (*Fraser et al.* 2008). We describe in more detail here the additional image processing steps that were necessitated by the use of Suprime-cam.

All images went through the same image pre-processing before the image search step. From the overscan strip, the bias level was measured for each image, and subtracted. It was found that the bias level varied by ~ 100 ADU (1%) along the bias strip. Proper removal of this variation required that a fourth order polynomial be fit in a least-squares sense to the overscan region. This polynomial bias-fit was removed from the raw images.

An average flat-field was produced for each chip from the sky-flats provided from the service mode observer (10 from night 1, 6 from night 2) using the *mask_mkflat_HA* routine from the sdfred software reductions package. This is the standard image pre-processing package provided and supported by Subaru (*Yagi et al.* 2002, *Ouchi et al.* 2004). This routine detects sources in the sky-flat images. Regions near detected sources are ignored when the average flat is produced.

The Suprime-cam field is vignetted, with $\sim 40\%$ throughput-loss near field edges. This vignetting needed to be accounted for when adding artificial sources to the data as the artificial sources must accurately reflect the sensitivity variations across each chip. Thus, the average flat-fields for each chip were separated into a quantum-efficiency variation map, and an illumination pattern. The illumination pattern was created by running a 20 by 20 pixel median filter over the average flat-fields. The quantum-efficiency variation map was set as the normalized difference of the flat-field and the illumination pattern, and was divided out of each of the over-scan subtracted images producing smooth images that revealed the vignetting pattern.

The Suprime-cam FOV is distorted such that a fast moving Kuiper belt object (KBO), with a rate of motion $\gtrsim 3"$/hr., whose motion would be linear on the sky, would not be linear in the images. Thus, spatial distortions needed to be removed. Image distortions were measured with the *dofit* routine (*Gwyn* 2008). This routine compares a reference source list containing true astrometric positions of sources, and positions of those sources within the images; from this, it calculates a 3rd order spatial distortion map. The image of the D2 field used to photometrically calibrate our images also provided a perfect astrometric reference, as sources in the field have been astrometrically calibrated with residuals better than 0.3". The distortion map was measured from the D2 field image of each night, and then used to resample all images onto a spatially flat image using the *SWarp* package (*Bertin et al.* 2002). Flux was conserved during this resampling, and produced images with a 0.1986" pixel-scale. The spatial rms residuals of the resampling were 0.06", or $\sim 1/3$ of a pixel as confirmed using the astrometric positions of stars in the USNO catalogs.

The point-source image shape varied significantly across each chip, and warranted the use of a spatially variable point-spread-function (PSF). It was found that a PSF whose shape varied linearly with image position could accurately re-produce the point-source image shape variations. For each chip, a gaussian PSF with look-up table was generated from 15 bright, unsaturated, hand-selected point-sources.

For each chip, a random number of artificial moving sources (between 150 and 250) were generated with random rates and angles of motion consistent with objects on circular Keplerian orbits between 25 and 200 AU, and with random fluxes consistent with that of point sources between 23 and 28.5 mag. These artificial sources were implanted blindly in the data, and the source list was revealed only after the search was complete. Additionally, 10 23rd mag. sources were implanted. These sources had flux sufficient to flag errors in the image combining algorithms.

Artificial sources with sky motions larger than 0.2 pixels were split up into a number of dimmer sources with total flux equal to the original source. The centres of the dimmer sources were shifted to account for the motion of the object in the images. The flux of each artificial source was varied from image to image to match the average brightness variations of 20 reference stars with respect to a reference image (that with the lowest airmass). Additionally, the fluxes of the artificial sources were scaled to account for the vignetting apparent in each chip. This was done by implanting the artificial source into a blank image. The blank image pixel values were then multiplied by the illumination pattern. This was subsequently summed with the vignetted sky images. After artificial object implanting, the illumination pattern was removed from the images. The result was images with spatially smooth backgrounds containing artificial sources with spatially varying sensitivity that matched that of the images.

No attempt was made to subtract a bias pattern from the raw images as no bias frames were provided from the service observations. The sdfred documentation however, claims that this step is unnecessary, as the bias level variations of Suprime-cam are low (*Yagi et al.* 2002, *Ouchi et al.* 2004).

To maximize the searchable area of the images, stationary objects were removed by subtracting an image template from the vignetting corrected images. The image template for each chip was created from an average of the search field images using an artificial skepticism routine which places little weight on pixels far away from the pixel average (*Stetson* 1989). Every fifth image was used to create the image template, reducing the presence of subtraction residuals created behind all moving sources, while ensuring a high quality template such that all stationary sources were sufficiently removed. The image subtraction was done using *psfmatch3* routine (*Pritchet* 2005).

Before final image stacks were produced, a high pixel mask was applied to the subtracted images to mask out any spurious hot-pixels and cosmic-ray spikes. The masked-subtracted images were spatially shifted to account for the motions of moving sources. A grid of shift rates ($0.4 - 4.5$ "/hr.) and angles ($\pm 15^o$ off the ecliptic) were considered which covered the range of motions consistent with bound solar system objects in the Kuiper belt on prograde orbits. In our past searches, we found that the search depth is not very sensitive to the choice in grid spacing between angles, but is very sensitive to the choice in spacing between rates. We chose a rate spacing small enough such that a moving source would never exhibit a trail longer than twice its seeing disk at the rate and angle which best approximated its apparent motion. Our grid consisted of 19 separate rates and 5 separate angles.

The data from each night was photometrically calibrated to the SDSS wavebands by comparing source flux measurements in the D2 field to those quoted in the Mega-pipe project (*Gwyn* 2008). A source's magnitude in the Subaru data is given by $r_{Sub} = 2.5 \log\left(\frac{b}{t}\right) + Z$ where b is the source brightness in ADU, t is the exposure time, and Z is the telescope zeropoint. For each chip, a linear relation of the form $r_{Sub} = C(g' - r')_{Mega} - r'_{Mega}$ was used to transformation the r'-band magnitudes in the Mega-pipe project to Subaru r-band magnitudes. The colour term, C, and the zeropoint Z were fit in a least-squares sense to the source-flux measurements in the data, and the Mega-pipe magnitudes using at least 40 sources on each chip. This procedure determined the best fit zeropoint to an accuracy of ~ 0.04 mag. The results are presented in Table 4.2. We found that chip 00 exhibits a 0.4 magnitude decrease in sensitivity compared to the other 9 chips, which is consistent with other photometrically calibrated Suprime-Cam observations (*Yoshida and Nakamura* 2007).

The transformations of the r' and g'-band Mega-pipe magnitudes to the r', and g'-bands in the SDSS filter set are given by $r'_{Mega} = r'_{SDSS} - 0.024(g' - r')_{SDSS}$ and $g'_{Mega} = g'_{SDSS} - 0.153(g' - r')_{SDSS}$. Using the colour term $C_{av} = -0.048$ which is the average of colour terms from Table 4.2, we find that the transformation between r-band Subaru and SDSS magnitudes is given by $r'_{SDSS} = r_{Sub} + 0.018(g' - r')_{SDSS}$. For typical KBOs $(g' - r')_{SDSS} \sim 0.7$ mag (*Fraser et al.* 2008). Thus, the r-band Subaru and SDSS magnitudes differ by ~ 0.01 mag. which is smaller than the uncertainty of the telescope zeropoint. Hence, we use the approximation that for KBOs, $r'_{SDSS} = r_{Sub}$.

4.3 Survey and results

From the first night, the grid of image stacks for each chip was manually searched by one operator producing a candidate source list. Moving sources were identified by their appearance in the images; a moving source is round (or nearly) in the image stack that best compensated for the source's apparent sky motion, and exhibits a characteristic trail in other stacks, helping the operator distinguish moving sources from noise. See *Fraser et al.* (2008) for a more complete discussion of this technique.

Implanted artificial sources were identified in the candidate source list if the candidate source's location was within a few pixel of the artificial source's true centre. The detected artificial sources allowed us to measure our detection efficiency as a function of magnitude, $\eta(r'_{SDSS})$. We represent the detection efficiency of the full field by the functional form

$$\eta(r'_{SDSS}) = \frac{\eta_{max}}{2}\left(1 - \tanh\frac{r'_{SDSS} - r_*}{g}\right) \tag{4.1}$$

where η_{max} is the maximum efficiency, r_* is the half-maximum detection efficiency magnitude, and g is approximately half the width of the fall from maximum detection efficiency to zero. This function was fit, in a least-squares sense, to the detection efficiency of artificial sources. The best fit parameters were $(\eta_{max}, r_*, g) = (0.932 \pm 0.008, 26.86 \pm 0.02, 0.44 \pm 0.03)$. The best-fit curve represents the measured detection efficiency well (see Figure 4.2).

We fit the measured efficiency with

$$\eta'(r'_{SDSS}) = \frac{\eta_{max}}{2}\left(1 - \tanh\frac{r'_{SDSS} - r_*}{g}\right)\left(1 - \tanh\frac{r'_{SDSS} - r_*}{g'}\right) \tag{4.2}$$

which has been found to represent the detection efficiency of previous KBO surveys (*Petit et al.* 2006, *Fuentes and Holman* 2008). The best-fit curve is presented in

Figure 4.2. As can be seen, there is very little difference between the more complicated efficiency representation and that of Equation 4.1, and both describe the measurements equally well. Thus, we find that the more complicated function is not warranted or necessary.

Flux measurements were made for all identified moving sources on the shifted image stack which contained the roundest image for that source. Magnitudes were measured in a 3-4.5 pixel radius aperture, and corresponding aperture corrections were determined from the image profiles of ten 23rd mag. artificial sources on each chip. By comparing the flux measurements of the detected artificial sources to their true values, we were able to characterize our flux measurement uncertainties. For background limited sources, the uncertainty in a source's measured magnitude, r, is given by $\Delta r = \gamma 10^{\frac{r-Z}{2.5}}$ where Z is the telescope zeropoint, and γ depends on the telescope and the observations (*Fraser et al.* 2008). We found that $\gamma = 1.33$ best described the observed uncertainties.

38 sources were not associated with artificial sources. 36 of these are identified as newly discovered KBOs. Two of these were identified as coincidental overlap of multiple poorly subtracted saturated galaxies. Both of these false detections have fluxes below the 50% detection efficiency. This is consistent with our previous survey - a non-zero false candidate rate occurred for detection efficiencies $\eta < 50\%$ (*Fraser et al.* 2008). We therefore truncate our detection efficiency at the 50% threshold and ignore the 8 sources faint-ward of this level.

From the positions of the objects on the first night, orbits were calculated using *fit_radec* (*Bernstein and Khushalani* 2000) and positions of the objects on night 2 were predicted. While not all of our objects had follow-up detections, we had a 100% follow-up rate for those 7 objects who's predicted positions fell in the FOV of the second night's observations. This is consistent with the 100% follow-up rate above the 50% detection threshold we report from our past survey (*Fraser et al.* 2008). We are thus confident that all detected non-artificial sources with magnitudes above the 50% threshold are real KBOs.

For each detected KBO, three image stacks were created (6 for those with follow-up) of the first half, middle half, and last half of the vignetting removed, non-subtracted images from a night's observations, using the rate and angle of motion that produced the roundest source image. From these, flux measurements were made. The final source magnitudes we report are the average of all the flux measurements made for that source off the image stacks where the source was at least a few FWHM away from nearby bright stars and galaxies. The results of our survey are presented in Table 4.3.

4.4 Luminosity function

Previous surveys have found that the differential LF (number of KBOs with magnitude m to $m + dm$ per square degree) of bright KBOs ($m(R) \lesssim 26$ mag.) is well represented by

$$\Sigma(m) = \ln(10)\alpha 10^{\alpha(m-m_o)} \tag{4.3}$$

where $\Sigma(m)$ is the number of objects with magnitude m (usually R-band) per square degree, α is the power-law "slope", and m_o is the magnitude for which the sky density of objects with magnitudes $\leq m$ is one per square degree (see for example *Trujillo et al.* (2001), *Gladman et al.* (2001), *Petit et al.* (2006)). In our previous work, we found $\alpha = 0.65$ and $m_o(R) = 23.43$ for a broad range of surveys(*Fraser et al.* 2008). *Bernstein et al.* (2004) presented the faintest Kuiper belt survey to date. Using a substantial amount of Hubble observations ($\sim$ 100 orbits) they achieved a search depth of $m(R) \sim 28.5$ (*Bernstein et al.* 2006) and discovered three KBOs. The dearth of detections was at least a factor of $\sim$ 10 below the number expected, requiring that the LF has a steep logarithmic slope for bright objects, that "rolls-over" to shallower slopes for fainter objects.

Fraser et al. (2008) presented a survey in which they searched 3 square degrees of the ecliptic to a depth of $m(R) \sim 25.4$ mag. and substantially increased the number of known detections suitable for a determination of the LF faint-ward of $m(R) \sim 23.5$. They found that the LF was well represented by a power-law given by Equation 4.3. They concluded that the lack of objects observed by *Bernstein et al.* (2004) must be caused by a sharp break rather than a broad roll-over, and that this could not occur for $m(R) \leq 24.4$.

Additionally, *Bernstein et al.* (2004) examined the LFs of the so-called cold and excited KBO populations, $i < 5^o$ and $i > 5^o$ respectively. They found that the cold population exhibited a steeper bright object slope than the excited population. The statistical support for such a difference however, was not strong. Simulations that test different Kuiper belt formation scenarios suggest that a difference in the SDs of different KBO populations is caused by different formation conditions/histories for those objects. Thus, a confirmation of the findings by *Bernstein et al.* (2004) is important, as it provides a very strong constraint on the Kuiper belt formation history.

The survey reported here detected 28 KBOs that can be used to characterize the luminosity function (LF) and SD of KBOs. With these detections, we wish to address three questions:

1. At what magnitude is the large object LF no longer a power-law?
2. Is the observed break consistent with the LF expected if the SD has a sharp break at some object radius? If not, what is the true shape of the LF?
3. Is the SD of the excited population different from that of the cold population?

4.4.1 LF forms

In determining the correct LF shape, we consider three functional representations of the differential LF. The first is the power-law given by Equation 4.3. The second is the rolling power-law suggested by *Bernstein et al.* (2004), given by

$$\Sigma(m) = \Sigma_{23} 10^{\alpha(m-23)+\alpha'(m-23)^2} \tag{4.4}$$

where α is the bright object slope, α' is the derivative of the logarithmic slope, and Σ_{23} is the number of objects per square degree at 23rd mag.

The third functional form we consider was first presented by *Fraser and Kavelaars* (2008a). They showed that, if the SD is a power-law with slope q_1 for large objects that has a sharp break at objects with diameter D_b to slope q_2 for small objects, then the *cumulative* LF has the form

$$N(<m) = A \begin{cases} a_1 10^{\alpha_1 m} & \text{if } m < m_1 \\ b_1 10^{\alpha_1 m} + b_2 10^{\alpha_2 m} + b_3(m) & \text{if } m_1 \leq m \leq m_2 \\ c_1 + c_2 10^{\alpha_2 m} & \text{if } m > m_2. \end{cases} \tag{4.5}$$

where $\Sigma(m) = \frac{dN(<m)}{dm}$, $\alpha_1 = \frac{q_1 - 1}{5}$ and $\alpha_2 = \frac{q_2 - 1}{5}$. In Equation 4.5 $m_1 = K + 5\log\left(r_1^2 D_b^{-1}\right)$ and $m_2 = K + 5\log\left(r_2^2 D_b^{-1}\right)$ are the magnitudes for which objects smaller than the break diameter are detectable by a given survey for heliocentric distances larger than the Kuiper belt inner edge r_1 but smaller than the outer edge r_2. $K \sim 18.4$ is the R-band magnitude of a $D \sim 1600$ km object at 40 AU with a 6% albedo.

The coefficients a_i, b_i, and c_i of Equation 4.5 are functions of the KBO radial distribution. *Fraser and Kavelaars* (2008a) have shown that the LF shape for $m_1 \leq m \leq m_2$ is strongly dependent on the assumed KBO radial distribution, but the SD slopes q_1 and q_2, and the break diameter D_b however, can be accurately inferred if data exists sufficiently far away from the break magnitude. They assume that the radial distribution is given by $N(\Delta) \propto \Delta^{-c}$, and suggest that $c = 10$ is a good approximation to the radial fall-off observed by *Trujillo and Brown* (2001). We assume the same radial distribution here and take the inner and outer edges of the disk as $r_1 = 35$ AU and $r_2 = 60$ AU.

These three functions provide a good sample of LF forms to consider as they progress in levels of complication by a single degree of freedom - the parameters for the different LF forms are (α, m_o) for Equation 4.3, $(\alpha, \alpha', \Sigma_{23})$ for Equation 4.4, and $(\alpha_1, \alpha_2, D_b, A)$ for Equation 4.5. Thus, it is a straight-forward process to determine the number of parameters necessary to describe the true shape of the LF using simple statistics techniques.

4.4.2 Data-sets

In our previous estimates of the LF, we considered observations from surveys for which the detection efficiency was well characterized as a function of magnitude. The F08 sample *Fraser et al.* (2008) consists of near ecliptic KBO surveys presented in *Jewitt et al.* (1998), *Gladman et al.* (1998, 2001), *Allen et al.* (2002), *Petit et al.* (2006), and *Fraser et al.* (2008) along with the data from *Trujillo et al.* (2001) which we subdivided by detection efficiency and astrometric position. The F08b sample is the F08 sample, plus the inclusion of the survey presented by *Bernstein et al.* (2004, 2006) and *the survey presented here.*

To measure any differences in the LF between the dynamically excited and cold populations, we define the F08b$_{i<5}$ and F08b$_{i>5}$ samples as those objects with inclinations smaller than and greater than 5^o respectively. For these samples, we only consider surveys in which the majority of objects have been observed on arcs longer than 24 hrs; inclinations measured from the observations spanning only one night are not accurate enough to make an inclination cut reliable, and a large contamination between the two samples would occur. Thus we exclude from the F08b$_{i<5}$ and

F08b$_{i>5}$ subsamples the Uranus field from *Petit et al.* (2006), the N11033, N10032W3, UNE, and UNW fields from *Fraser et al.* (2008), and the survey presented here.

While an inclination cut does not directly probe the different KBO populations, ie. cold/hot-classical objects, resonators, scattered members, etc. (*Gladman et al.* 2008), it does provide a crude means of separating those KBOs with 'highly' excited orbits from those with less excited orbits. The division of $i = 5^o$ is chosen to ease comparison with the LF presented by *Bernstein et al.* (2004). For the F08b$_{i<5}$ and F08b$_{i>5}$ samples, no heliocentric distance cut was made.

Note: the analysis for this manuscript was already complete before the authors were aware of the survey presented by *Fuentes and Holman* (2008). The moderate increase in the total number of detections, $\sim 20\%$, will not substantially alter the results presented here. Thus, we did not include the survey of *Fuentes and Holman* (2008) in our analysis. Their results however, are discussed below.

4.4.3 Analysis

In determining the correct LF shape and best-fit parameters of the various functional forms, we adopt the same practices as *Fraser et al.* (2008), *Fraser and Kavelaars* (2008a). These are as follows:

1. We cull from each survey all sources faintward of the 50% detection efficiency of that survey, and set the detection efficiency to zero faintward of that point.
2. We offset all magnitudes to R-band using the average KBO colours presented in *Fraser et al.* (2008).
3. We fit the differential LF, $\Sigma(m) = \frac{dN(<m)}{dm}$ using a maximum likelihood technique.
4. We adopted the same form of the likelihood equation as presented in *Fraser et al.* (2008) which treats calibration errors and variable sky densities as sepa-

rate nuisance parameters. We marginalized the likelihood over these parameters before determining the maximum likelihood.

5. We adopted the same prior ranges of the colour and density parameters as presented in *Fraser et al.* (2008) (±0.2 magnitudes for the colour parameters, and ±0.4 for the logarithm of the density parameters).

In determining the quality of the fits, we utilize the Anderson-Darling statistic

$$\Delta = \int_0^1 \frac{\left(S(m) - P(m)\right)^2}{P(m)\left(1 - P(m)\right)} dP(m) \tag{4.6}$$

where $P(m)$ is the cumulative probability of detecting an object with magnitude $\leq m$ and $S(m)$ is the cumulative distribution of detections. We calculate the probability, $P(\Delta > \Delta_{obs})$ of finding a value of the Anderson-Darling statistic, Δ, larger than that of the observations for a given LF function and parameter set by bootstrapping the statistic, ie. randomly drawing a subsample of objects from that LF equal to that detected in a particular sample, and fitting the LF to that random sample and computing Δ. In the random sampling process, we include random sky-density and colour offsets which represent those expected from the real observations. Values of $P(\Delta > \Delta_{obs})$ near 0 indicate that the functional form is a poor representation of the data.

To determine if the more complicated LF functional forms are statistically warranted, we utilize the log-likelihood test $\chi^2 = -2\log\frac{L'}{L}$. The logarithm of the ratio of maximum likelihoods of the simple and more complicated functions, L and L', are distributed as a chi-squared variable with a number of degrees of freedom equal to the difference in free parameters between the two functional forms. A table of χ^2 values can be used to determine the significance of the improvement in the LF fit between the two functional forms (*Kotz and Johnson* 1983).

4.5 Results

4.5.1 F08b Sample

Presented in Table 4.4 are the best-fit parameters for the three different LF forms, and $P(\Delta > \Delta_{obs})$ of each fit. The best-fit power-law slope to the F08b data-set, $\alpha = 0.58$, is moderately shallower than, but is consistent with the best-fit $\alpha = 0.65$ from *Fraser et al.* (2008). The fit however, is a poor description of the data as evidenced by the low $P(\Delta > \Delta_{obs}) < 0.04$.

The best-fit of the rolling power-law to the F08b data-set is $(\alpha, \alpha', \Sigma_{23}) = (0.8, -0.06, 0.82)$. The maximum likelihood value of this fit is increased by more than two orders of magnitude over the power-law which warrants the inclusion of a third degree of freedom, and the fit is an acceptable description of the F08b sample, with $P(\Delta > \Delta_{obs}) = 0.4$.

The best-fit of the LF given by Equation 4.5, $(\log A, \alpha_1, \alpha_2, D_b) = (23.56, 0.76, 0.18, 62)$, is an acceptable fit to the data with $P(\Delta > \Delta_{obs}) = 0.4$. The maximum likelihood value is increased by more than two orders of magnitude over the power-law with a log-likelihood chi-square, $\chi^2 = 11.7$, and by a factor of 2 over the rolling power-law with $\chi^2 = 1.4$. We find that the best-fit from Equation 4.5 is preferred over the power-law at greater than the 3-sigma level. This fit is preferred over the rolling power-law at $\sim 80\%$ significance. Thus we find that both the rolling power-law and broken power-law of Equation 4.5 provide equally adequate descriptions of the F08b sample. Note: the Monte-Carlo simulations we have done to calculate $P(\Delta > \Delta_{obs})$ have also demonstrated that on average, the best-fit LF parameters determined from our maximum likelihood technique reproduce the input parameters of the simulations for all LF functionals forms we have considered here.

When the observations of *Bernstein et al.* (2004) are excluded from the F08b sample, the best-fit power-law has parameters $(\alpha, m_o) = (0.65, 23.42)$, which is nearly identical to that found from by *Fraser et al.* (2008). The power-law is a moderately adequate description of the observations with $P(\Delta > \Delta_{obs}) = 0.1$. This result hints that the Kuiper belt LF exhibits a break within the magnitude range of the F08b sample, but fits to the survey data with $m(R) \lesssim 27$ do not explicitly require a broken or rolling power-law description.

Presented in Figures 4.3, 4.4, and 4.5 are the credible regions of the fits to the F08b sample. The function given by Equation 4.5 is derived from a size-distribution similar to that expected from accretion calculations, and thus provides a proper interpretation of the under-lying size-distribution. We find that the LF is consistent with a broken power-law size-distribution with large and small object slopes $q_1 = 4.8 \pm 3$ and $q_2 = 2 \pm 2$, and a break diameter, $D_b = 60 \pm 40$ km.

Presented in Figure 4.6 is a histogram of the F08b sample, the best-fit LFs for the three functional forms we consider, the best-fit power-law LF from *Fraser et al.* (2008), and the best-fit LF presented by *Fuentes and Holman* (2008). As can be seen, power-laws do not provide acceptable fits to the data with $m(R) \sim 28$, and a more complicated function is required. Equations 4.4 and 4.5 both provide reasonable descriptions of the observations.

The user is cautioned from drawing any further conclusions from Figure 4.6. The F08b sample contains data from many different surveys. Thus the sample includes any calibration errors and sky-density variations between surveys which might lead the reader to a false conclusion about the structure of the LF (see *Fraser et al.* (2008) for a discussion of the magnitude and significance of these effects).

The best-fit LF presented by *Fuentes and Holman* (2008) is a harmonic mean of two power-laws with bright-end slope $\alpha_1 = 0.7$ and faint-end slope $\alpha_2 = 0.3$ with a break magnitude of $R_{eq} \sim 24.3$. These parameters are consistent with the slopes and break magnitude of our best-fit non-power-law LFs. They find however, a factor of 3 higher sky-density which is inconsistent at greater than the 3-sigma level with the range of sky densities we find for similar bright-end slopes (see Figure 4.4). The source of the increased number of detections compared to that expected from fits to the F08b sample is unknown.

4.5.2 F08b$_{i>5}$ Sample

When we consider the F08b$_{i>5}$ sample, we find that the best-fit power-law has slope $\alpha = 0.55$ with $P(\Delta > \Delta_{obs}) < 0.04$, and is a poor description of the data. The sample has no objects fainter than $m(R) \sim 25.8$. The lack of faint objects requires a break near this point. The best-fit rolling power-law with parameters $(\alpha, \alpha', \Sigma_{23}) = (0.74, -0.06, 0.46)$ is an acceptable fit to the data with $P(\Delta > \Delta_{obs}) = 0.1$. The best-fit broken power-law model is an acceptable description of the data with $P(\Delta > \Delta_{OBS}) = 0.1$. The log-likelihood ratio implies that the broken power-law model of Equation 4.5 is preferred over the rolling power-law at the 90% significance level. The best-fit has $\alpha_1 = 0.7$ and breaks at $D_b = 36$ km. Because the F08b$_{i>5}$ sample has no detections faint-ward of the break, both the break diameter and small-object slope of this sample are poorly constrained. The maximum likelihood is found with a break at $m(R) = 25.8$ with no objects faint-ward of this point. ie. $\alpha_2 = -\infty$. Note: we consider slopes, $\alpha_2 > -6$ to avoid numerical errors in the likelihood calculations.

Presented in Figures 4.7, 4.8, and 4.9 are the likelihood contours of the best-fit of Equation 4.5 to the F08b$_{i>5}$ sample and the histogram of those data. As can be seen, the LF is well described by a power-law for $m(R) \lesssim 25.8$. The lack of faint objects requires that a break must exist at $D_b \lesssim 100$ km.

The faint-object slope is highly uncertain, with a 1-sigma upper-limit of $\alpha_2 \sim 0.6$. This fit however is consistent with that of the F08b sample best-fit at the $\sim$ 1-sigma level. Though the inclinations of the detections we present in this survey are inaccurate, they hint that the break in the LF for the F08b$_{i>5}$ sample is not as sharp as the fit would suggest. The detections from this survey are consistent with the same break diameter (36 km) that breaks to a much flatter faint object slope similar to the 1-sigma upper-limit of the fit ($\alpha_2 \sim 0$). The fit to the F08b$_{i>5}$ sample however, constrains the break to be brightward of $m(R) \lesssim 26.8$. Additional data brightward of $m(R) \sim 27.5$ with accurate inclinations is required before the break location can be accurately constrained.

4.5.3 F08b$_{i<5}$ Sample

The low-inclination LF is sufficiently described by a power-law. The best-fit power-law is an acceptable description of the sample, with parameters $(\alpha, m_o) = (0.59, 24.0)$ and an Anderson-Darling statistic, $P(\Delta > \Delta_{obs}) = 0.15$. Indeed the best-fit of Equation 4.5 is found when the break occurs at the bright-end limit of the data, suggesting there is no strong evidence for a break in the F08b$_{i<5}$ data.

Presented in Figures 4.10 and 4.11 are the likelihood contours of the fit to the low-inclination LF, and the histogram of the observations. As can be seen, there is no apparent evidence for a break in the magnitude range of the observations.

To test whether or not the excited and cold samples have different LFs, we utilized the Anderson-Darling test described above (see Section 4.4.3) to determine whether or not the broken LF fit of the F08b$_{i>5}$ sample is an adequate description of the F08b$_{i<5}$ sample. We however, set $\alpha_2 = 0$ rather than the best-fit value, as this is a more realistic faint object slope than that of the best-fit of the F08b$_{i>5}$ sample ($\alpha_2 \sim -\infty$), as suggested by our survey. This slope is still within the 1-sigma credible region of the fit (see Section 4.5.2). We found that for the F08b$_{i<5}$ sample, an LF with $(\alpha_1, \alpha_2, D_b, \log A) = (0.7, 0, 34, 22.66)$ has $P(\Delta > \Delta_{obs}) = 0.4$, and is a sufficient description of the cold sample LF. We therefore conclude that we have no evidence that those KBOs with $i > 5$ have a different LF than those with $i < 5$.

Bernstein et al. (2004) found that the LFs of the cold and excited populations were different. *Fuentes and Holman* (2008) found similar results for their survey alone, and concluded that the low inclination population LF exhibits a bright-end slope $\alpha \sim 0.8 - 1.5$, steeper than $\alpha_1 \sim 0.7$ found when they considered objects of all i in their survey. When they considered all available data - the F08b sample, but not including the survey presented here, and including their own search - they found that the low-inclination group exhibited a significantly steeper bright-object slope than the high-inclination sample. This finding is intriguing, as we find no evidence for a difference in the SDs of the low and high inclination groups. It is possible that their results are a consequence of not considering calibration and density offsets when performing the likelihood calculations, as we have done here. Clearly however, more observations are needed which probe the entire range of current observations before these results can be clarified.

4.6 Discussion

The best-fit parameters for the LF presented in Equation 4.5 imply that the size distribution is a power-law with slope $q_1 \sim 4.8$ for large objects, which breaks to a shallower slope at diameter $D_b \sim 50 - 95$ km assuming 6% albedos. Comparison of this size distribution to models which evolve a population of planetesimals and track their size distribution as a function of time in the Kuiper belt region can place constraint on the formation processes and the duration of accretion in that region (*Kenyon and Bromley* 2001, *Kenyon* 2002, *Kenyon and Bromley* 2004).

In the early stages of formation, run-away growth occurs, and very rapidly grow objects as large as $\sim 10^3$ km in the in the Kuiper belt (*Kenyon* 2002). During this process, a steep-sloped large object size distribution develops, which flattens with time as more objects become "large". Calculations presented in *Kenyon* (2002), which simulate planet accretion for conditions in the Kuiper belt expected for the early solar system, imply that, in the absence of influences from Neptune, the modern-day large object slope would be shallower than that observed if accretion lasted the age of the solar system. They find that for an initial Kuiper belt mass similar to that predicted from the minimum-mass solar nebula model (*Hayashi* 1981) - much more massive than the current belt (*Fuentes and Holman* 2008) - accretion must have been halted after $\sim$ 100 Myr. If KBOs are weak (easier to disrupt), then accretion might have gone on for as long as 1 Gyr (see Figures 9, and 10 from *Kenyon* 2002). Some event(s) must have halted this process by clearing the majority of initial mass out of the belt before the slope became too shallow.

Kenyon and Bromley (2004) have demonstrated that weaker bodies will exhibit a size distribution with a larger break diameter D_b than stronger bodies would if they underwent the same evolutionary history. They calculated the size distribution expected from a Kuiper belt under the gravitational influence of Neptune which evolved for the age of the solar system. In this model, break diameters as large as 60 km were produced only for the weakest bodies they considered. This model however, produced a large object slope much too shallow to be consistent with the observations, implying that accretion over the age of the solar system cannot have occurred.

The existence of such a large break diameter in the KBO SD implies that, KBOs must be quite weak (strengthless rubble piles), and have undergone a period of increased collisional evolution. This suggests a scenario in which the event responsible for the early end to accretion, and the clearing of the majority of the mass in the Kuiper belt, also increased the rate of collisional evolution for a time, pushing the break diameter to the large value we see today.

Collisional disruption would be substantially increased for a period of time during the scattering of planetesimals by a rogue planet (*Gladman and Chan* 2006), or during a close stellar passage (*Ida et al.* 2000, *Levison et al.* 2004). During these scenarios, relative velocities of KBOs are increased, causing collisions between bodies to result in catastrophic disruption, rather than accretion as would otherwise be the case. The combination of scattering and collisional grinding would produce a substantial mass loss in the Kuiper belt region, and produce the large knee observed currently.

Increased bombardment would also occur if Neptune migrated outwards. In such a scenario, Neptune formed closer to the Sun than its current location. Gravitational scattering of small planetesimals transfer angular momentum to Neptune, causing the gas-giant to migrate outwards. During this process, some planetesimals have their orbits excited, and are thrust into the modern day Kuiper belt creating the orbital distribution we see today. The remaining planetesimals are cleared from the system during close encounters with Neptune causing a rapid and substantial mass-loss during the migration process. Various incarnations of this attractive scenario can provide the necessary collisional bombardment of KBOs, and simultaneously account for some of the other observed features of the Kuiper belt (*Malhotra* 1993, *Levison and Morbidelli* 2003, *Hahn and Malhotra* 2005, *Levison et al.* 2008).

The Neptune migration scenario predicts that the more excited population will have a more evolved size distribution, with a shallower large-object slope - objects which originated closer to the Sun have stronger encounters with Neptune, and thus have the most excited final orbits. These now excited objects would have originated from a more dense region of the protoplanetary disk, and hence underwent more rapid accretionary evolution, than objects which originated further from the Sun producing the shallower large object slope. We do not see any differences in the large object slopes of the cold and excited populations. Our findings suggest that, assuming migration of Neptune occurred, the total distance travelled by Neptune was sufficiently small such that the rate of planet formation and hence the size distribution of all objects scattered by Neptune and implaced in the Kuiper belt could not be substantially different.

4.7 Conclusions

We have performed a survey of the Kuiper covering $\sim 1/3$ a square degree of the sky using Suprime-cam on the Subaru telescope, to a limiting magnitude of $m_{50}(R) \sim 26.8$

and have found 36 new KBOs. Using the likelihood technique of *Fraser et al.* (2008) which accounts for calibration errors and sky density variations between separate observations, we have combined the observations of this survey with previous observations, and have found that the luminosity function of the Kuiper belt is inconsistent with a power-law with slope $\alpha_1 = 0.76$, but must break to a shallower slope $\alpha_2 \sim 0.2$ at magnitudes $m(R) \sim 24.1 - 25.3$. The luminosity function is consistent with a size distribution with large object slope $q_1 \sim 4.8$ that breaks to a shallower slope $q_2 \sim 1.9$ at a diameter of $\sim 50 - 95$ km assuming 6% albedos. We have found no conclusive evidence that the size distribution of KBOs with $i < 5$ is different than that of those with $i > 5$.

4.8 Acknowledgements

This project was funded by the National Science and Engineering Research Council and the National Research Council of Canada. This research used the facilities of the Canadian Astronomy Data Centre operated by the National Research Council of Canada with the support of the Canadian Space Agency.

Table 4.1: Observation Details.

Night	Date	Seeing (")	Number of Exposures	α	δ
1	April 22 2008	$\sim 0.4 - 0.7$	55 × 60 s.	13:46:57.7	10:44:00
2	May 8 2008	$\sim 0.4 - 0.8$	53 × 60 s.	13:46:57.7	10:44:00

Table 4.2: Data Calibration Details. The zero-point, Z, and colour term, C, of each chip of Suprime-Cam (see Section 2).

Chip	Z (mag.)	C
00	27.48	-0.040
01	27.81	-0.050
02	27.78	-0.065
03	27.85	-0.020
04	27.73	-0.095
05	27.89	-0.020
06	27.82	-0.045
07	27.83	-0.040
08	27.86	-0.040
09	27.75	-0.065

Table 4.3: Survey Results. r_{SDSS} is the average r-band magnitude, n is the number of flux measurements used in the average, Δ is the object's heliocentric distance, and i is the object's inclination.

Object	r_{SDSS} (mag.)	n	Δ	i (^{o})	Follow-up
c9a2	24.038 ± 0.0424	3	40 ± 3	22 ± 14	n
c1a3	24.368 ± 0.0575	3	44 ± 3	9 ± 12	n
c6a3	24.394 ± 0.0585	6	45 ± 2	5 ± 2	y
c1a1	24.991 ± 0.1018	3	44 ± 3	1 ± 7	n
c3a1	25.179 ± 0.1212	3	42 ± 3	0 ± 2	n
c5a2	25.245 ± 0.1293	3	41 ± 3	3.3 ± 10	n
c5a5	25.373 ± 0.1444	3	49 ± 3	3 ± 14	n
c8a2	25.397 ± 0.1485	3	47 ± 4	15 ± 15	n
c4a1	25.432 ± 0.1527	3	45 ± 3	9 ± 13	n
c9a1	25.434 ± 0.1527	3	35 ± 3	28 ± 16	n
c9a4	25.438 ± 0.1541	3	48 ± 3	2 ± 13	n
c8a1	25.458 ± 0.1569	3	43 ± 3	2 ± 11	n
c2a1	25.462 ± 0.1569	3	48 ± 3	7 ± 14	n
c4a3	25.569 ± 0.1737	3	38 ± 3	5 ± 10	n
c4a5	25.823 ± 0.2187	3	42 ± 3	5 ± 11	n
c5a9	25.875 ± 0.2311	3	45 ± 3	5 ± 12	n
c6a1	26.019 ± 0.2629	6	37 ± 3	2 ± 9	y
c0a2	26.068 ± 0.2753	6	45 ± 2	1.1 ± 0.3	y
c2a3	26.279 ± 0.3340	4	43 ± 3	5 ± 12	y
c1a4	26.282 ± 0.3340	3	44 ± 3	4 ± 12	n
c0a1	26.334 ± 0.3498	6	45 ± 3	14 ± 5	y
c6a2	26.382 ± 0.3663	6	44 ± 2	3 ± 1	y
c2a2	26.583 ± 0.4404	6	39 ± 2	10 ± 4	y
c4a6	26.610 ± 0.4527	3	43 ± 4	23 ± 17	n
c4a2	26.673 ± 0.4784	3	45 ± 3	12 ± 13	n
c1a5	26.680 ± 0.4828	2	37 ± 3	27 ± 17	n
c5a3	26.688 ± 0.4873	2	44 ± 3	7 ± 12	n
c5a8	26.737 ± 0.5103	3	47 ± 3	7 ± 13	n
c5a7	26.858 ± 0.5699	3	44 ± 3	1 ± 9	n
c4a7	26.859 ± 0.5699	3	34 ± 3	9 ± 9	n
c9a3	26.883 ± 0.5805	1	47 ± 5	75 ± 29	n
c7a1	26.925 ± 0.6079	3	45 ± 3	16 ± 15	n
c5a1	27.120 ± 0.7241	3	43 ± 3	1 ± 8	n
c5a6	27.276 ± 0.8391	3	47 ± 3	6 ± 14	n
c1a2	27.353 ± 0.8950	2	55 ± 4	12 ± 18	n
c5a4	28.807 ± 3.4344	3	42 ± 3	0 ± 1	n

Table 4.4: Luminosity Function Fits and associated Anderson-Darling statistics. $<$ indicate 1-sigma upper limits. We do not present fits utilizing functions with more degrees of freedom than are statistically warranted by the observations. The F08b$_{i<5}$ sample was not fit with Equation 4.5 but is adequately described by LF parameters within the 1-sigma range of the fit of the F08b$_{i>5}$ sample.

Data-set	Power-Law		Rolling Power-law		Broken Power-law	
	(α, m_o)	$P(\Delta > \Delta_{obs})$	$(\Sigma_{23}, \alpha, \alpha')$	$P(\Delta > \Delta_{obs})$	$(\log A, \alpha_1, \alpha_2, D_b)$	$P(\Delta > \Delta_{obs})$
F08b	$(0.58, 23.31)$	< 0.04	$(0.82, 0.80, -0.06)$	0.4	$(23.56, 0.76, 0.1762, 62)$	0.4
F08b$_{i<5}$	$(0.59, 24.0)$	0.15	–	-	-	-
F08b$_{i>5}$	$(0.55, 23.81)$	< 0.04	$(0.46, 0.74, -0.06)$	0.1	$(22.66, 0.70, -6, 36)$	0.1

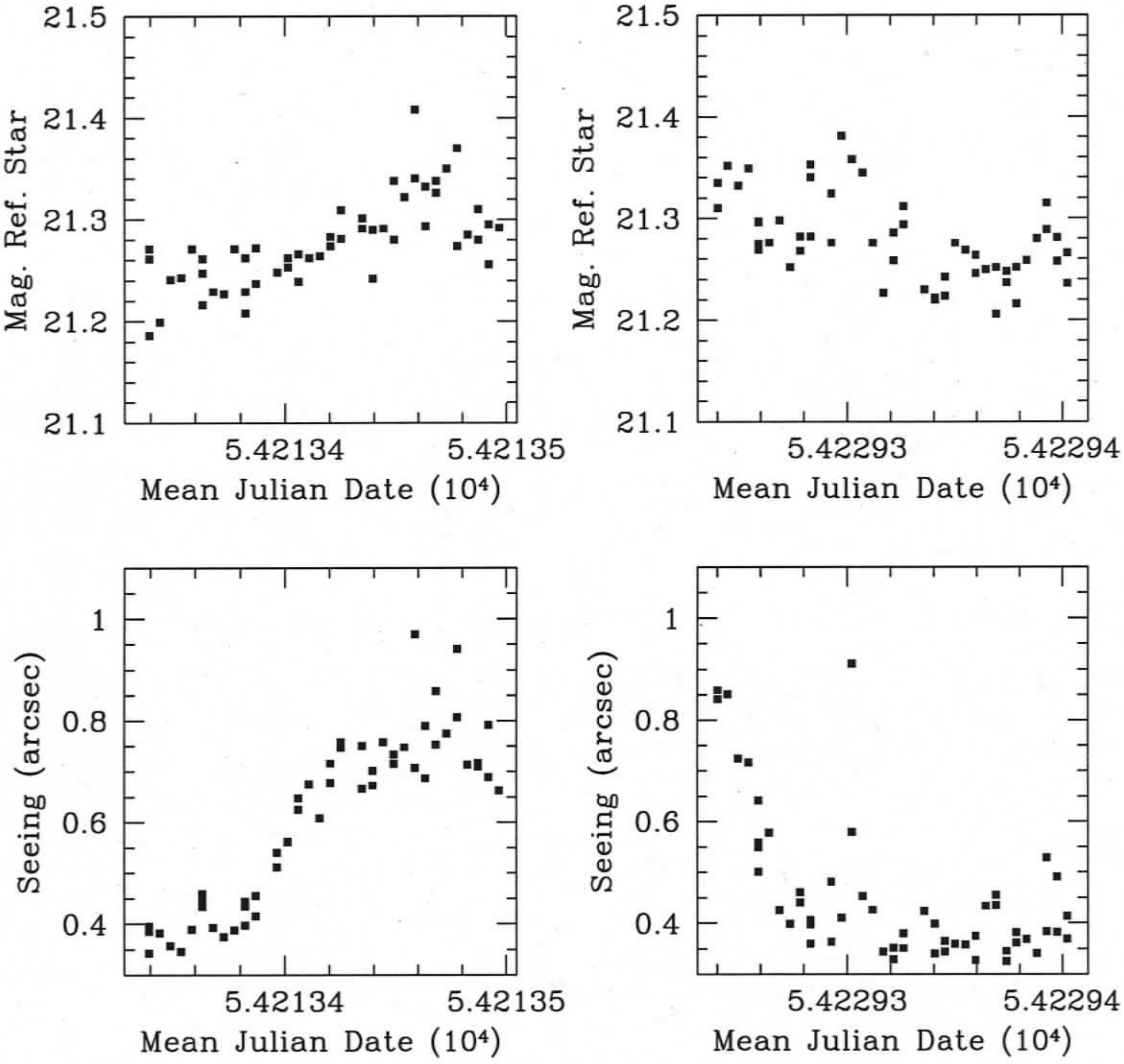

Figure 4.1: Reference star magnitude and full-width-half-maximum for the April 22nd (left) and May 8th (right) nights.

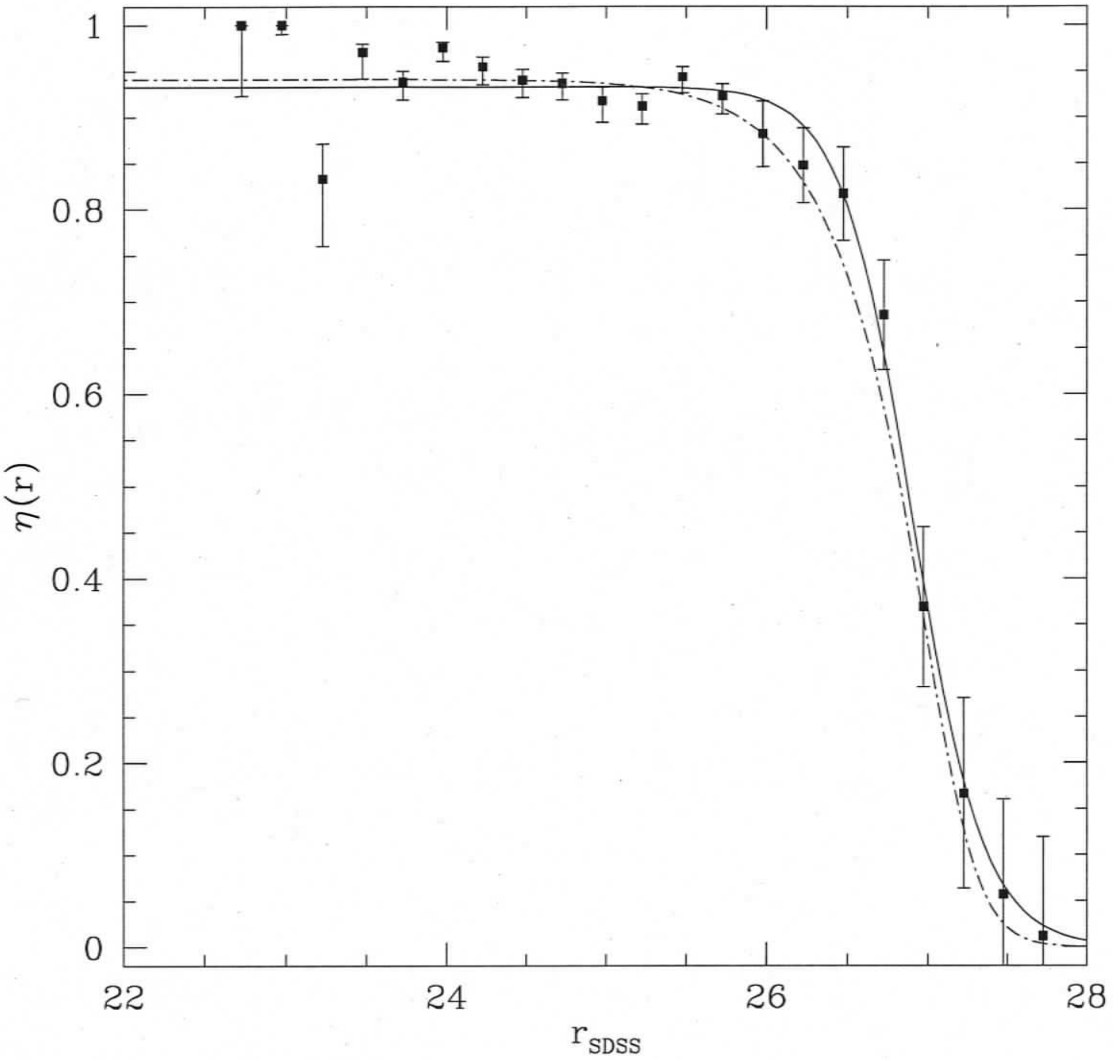

Figure 4.2: Detection efficiency histogram with 1-sigma poisson errorbars, and the best-fit efficiency functions $(\eta_{max}, r_*, g) = (0.932, 26.86, 0.44)$ (solid) and $(\eta_{max}, r_*, g, g') = (0.941, 27.14, 0.333, 0.758)$ (dashed-dotted).

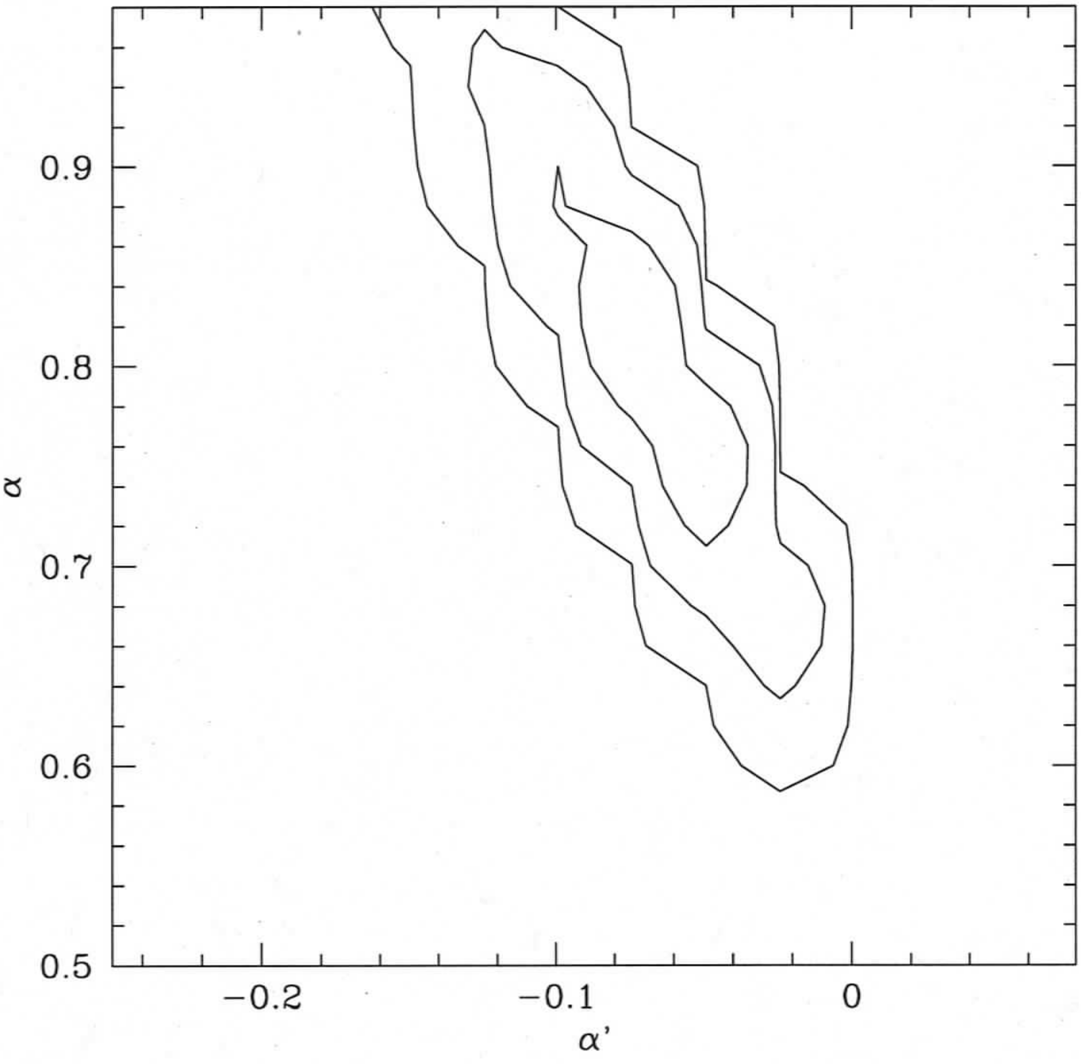

Figure 4.3: The 1,2, and 3-sigma credible regions of the best-fit rolling power-law to the F08b sample with Σ_{23} held at its best-fit value.

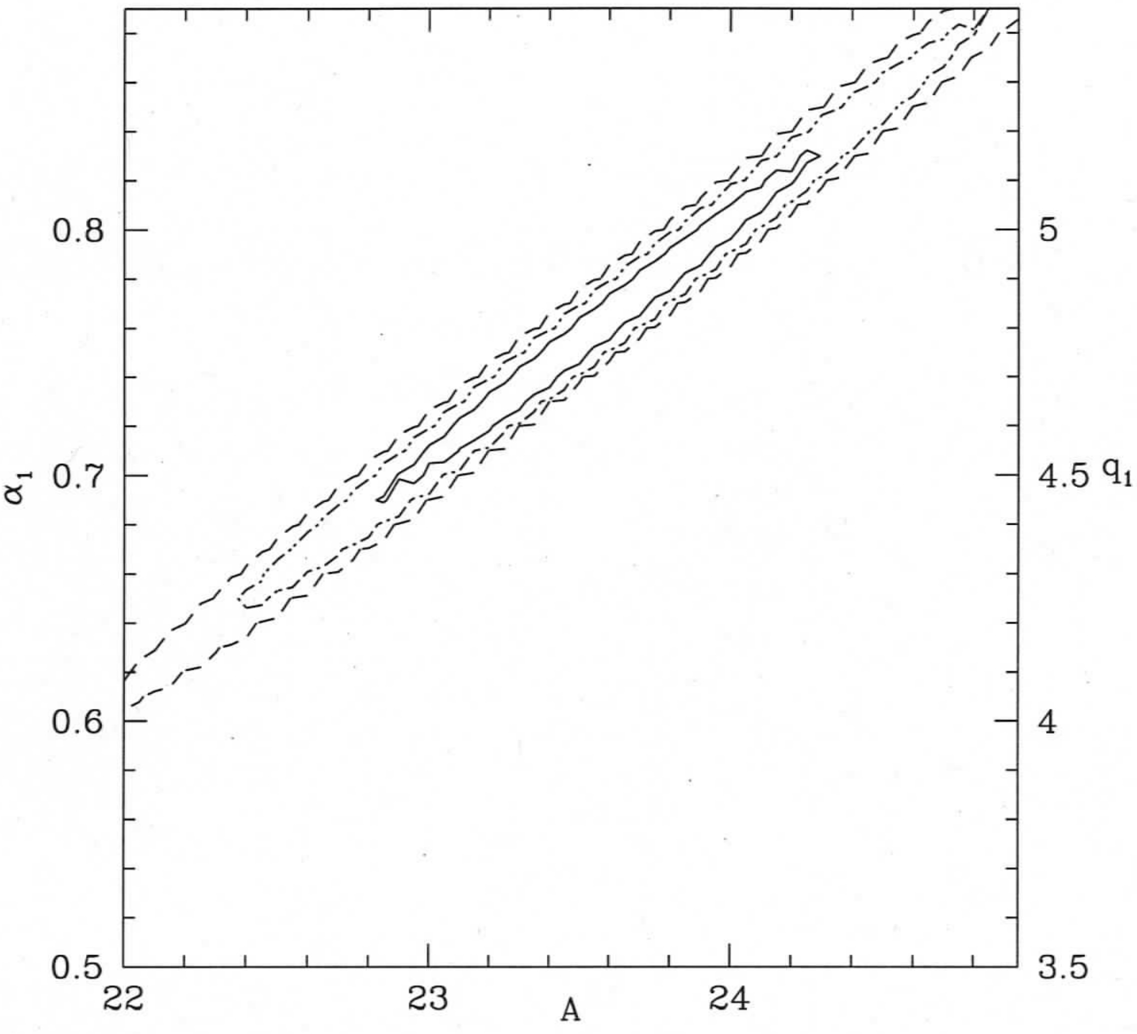

Figure 4.4: The 1,2, and 3-sigma credible regions of the best-fit of Eq 4.5 to the F08b sample with α_2 and D_b held at their best-fit values.

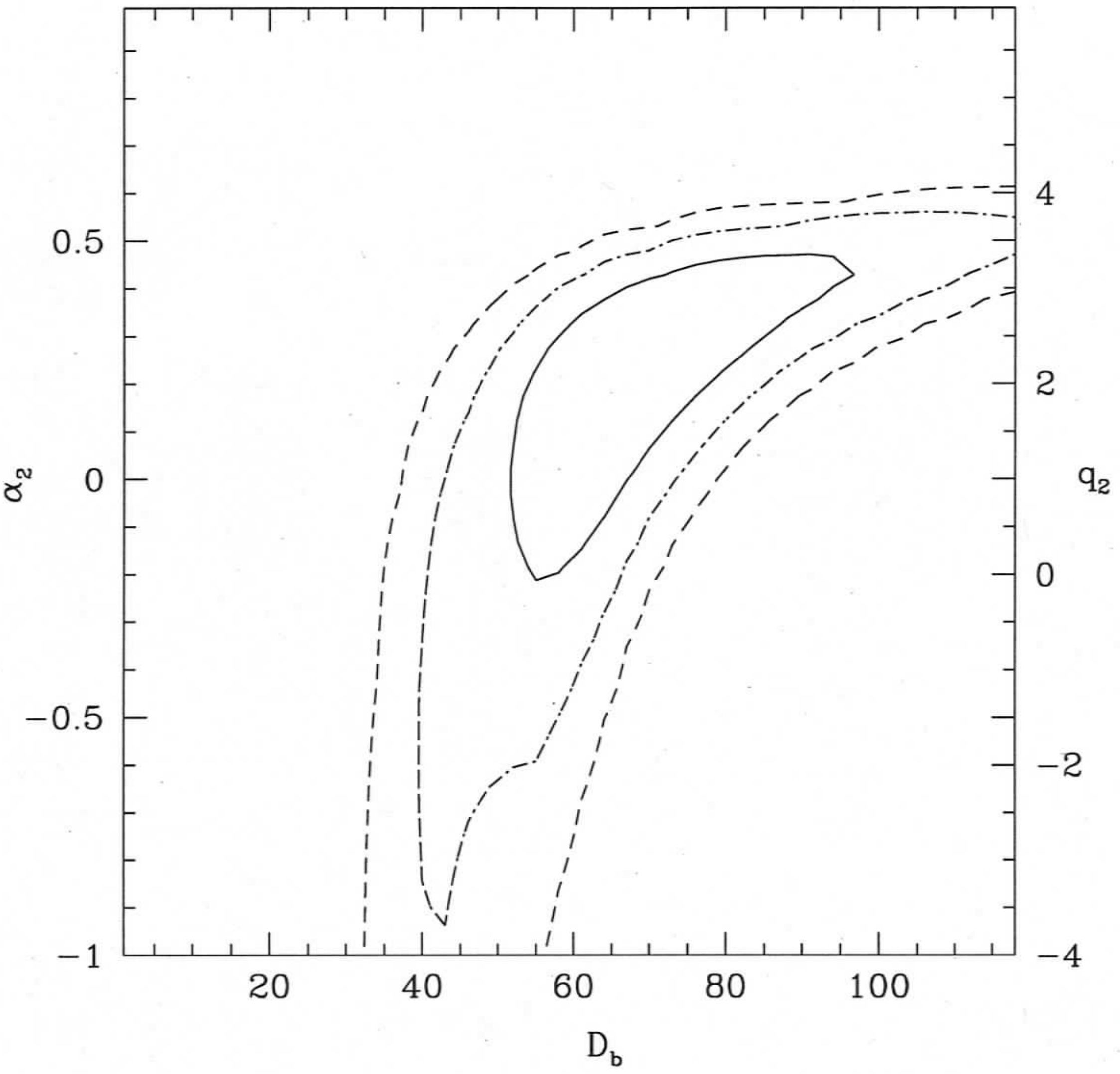

Figure 4.5: The 1,2, and 3-sigma credible regions of the best-fit of Eq 4.5 to the F08b sample with α_1 and A held at their best-fit values.

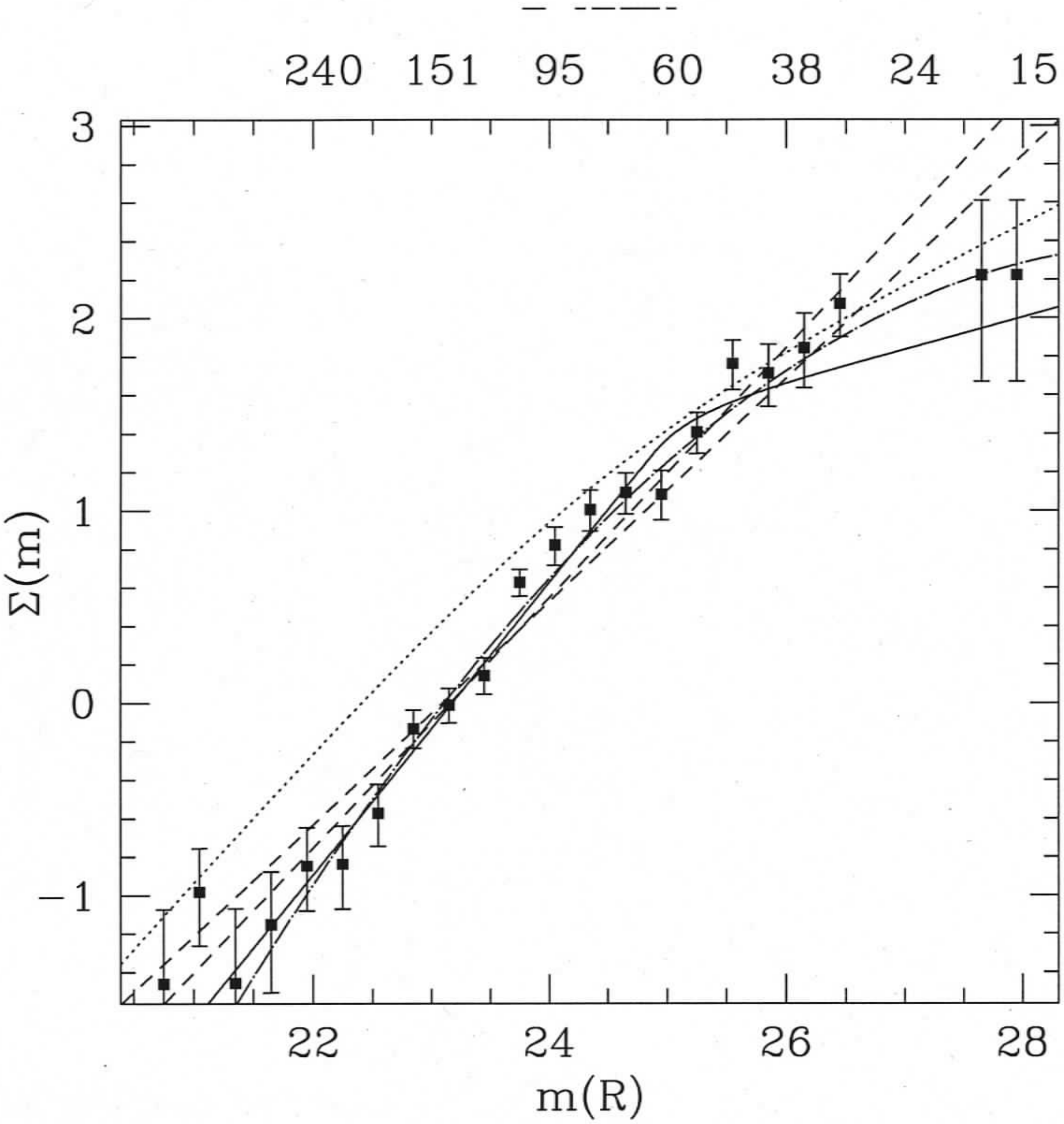

Figure 4.6: Histogram of the data considered in the F08b sample with al magnitudes shifted to R-band using the colours presented in *Fraser et al.* (2008). Errorbars are 1-sigma poisson intervals. The solid curve is the best-fit LF of Equation 4.5. The dashed curves are the best-fit power-law LFs from this manuscript (shallow) and *Fraser et al.* (2008) (steep). The dashed-dotted curve is the best-fit rolling power-law. The dotted curve is the best-fit LF presented by *Fuentes and Holman* (2008). Object diameters (km) are given assuming 6% albedos at 35 AU.

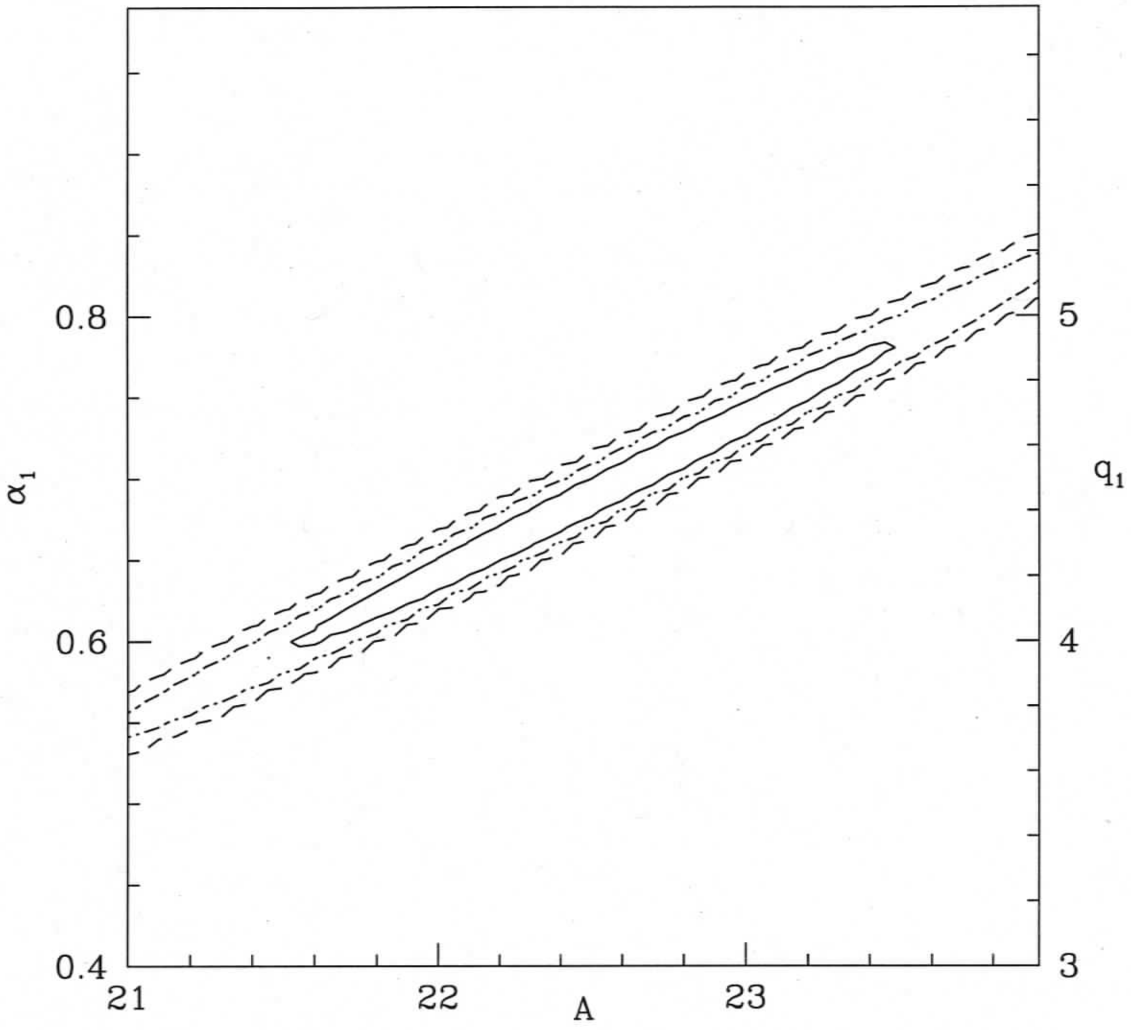

Figure 4.7: The credible regions of the best-fit of Equation 4.5 to the $F08b_{i>5}$ sample. Contours are the 1, 2, and 3-sigma credible regions of the fit with α_2 and D_b held at their best-fit values..

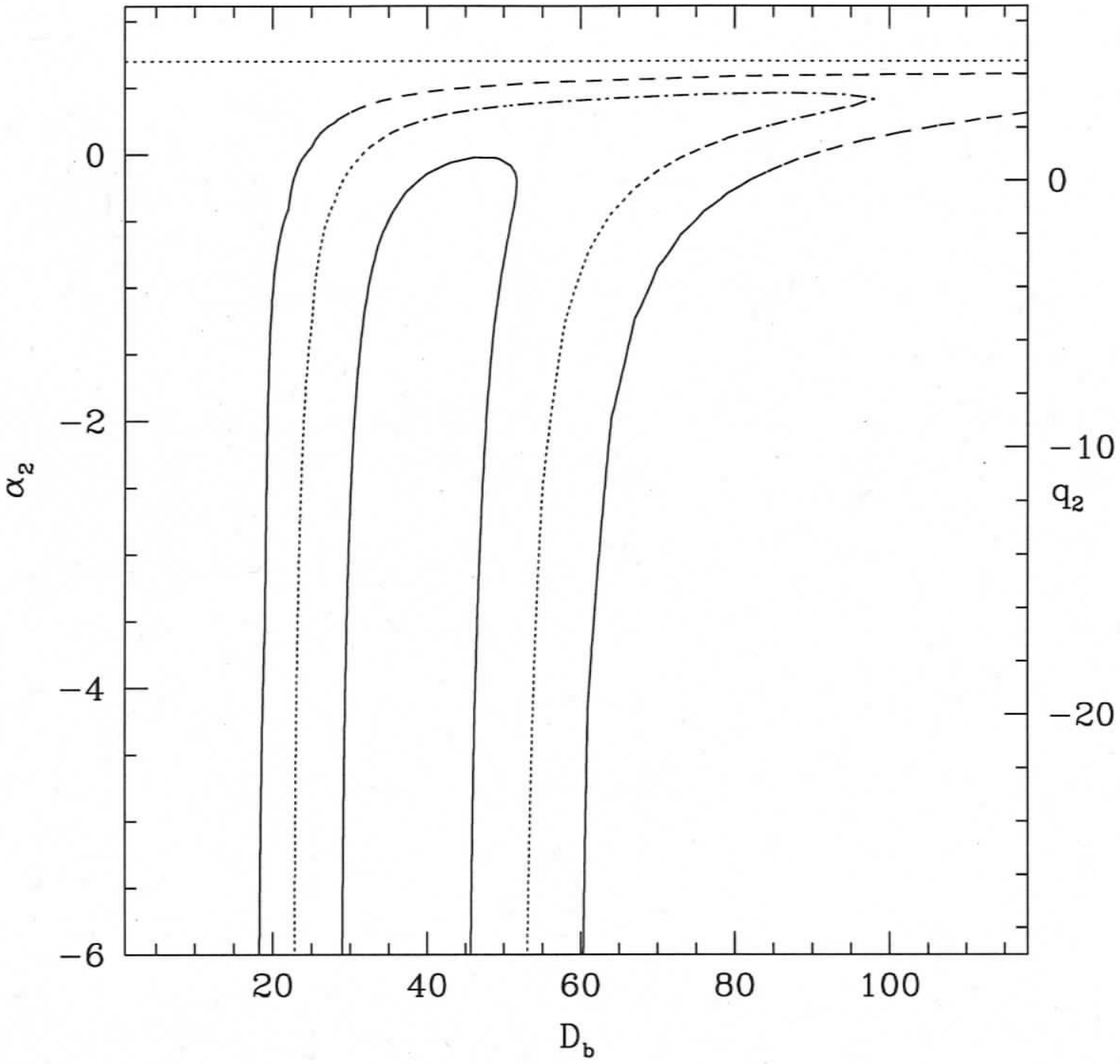

Figure 4.8: The credible regions of the best-fit of Equation 4.5 to the F08b$_{i>5}$ sample. Contours are the 1, 2, and 3-sigma credible regions of the fit with α_1 and A held at their best-fit values. The dotted horizontal line marks the best-fit large object slope, and demonstrates the need for a break to shallower slopes for this sample.

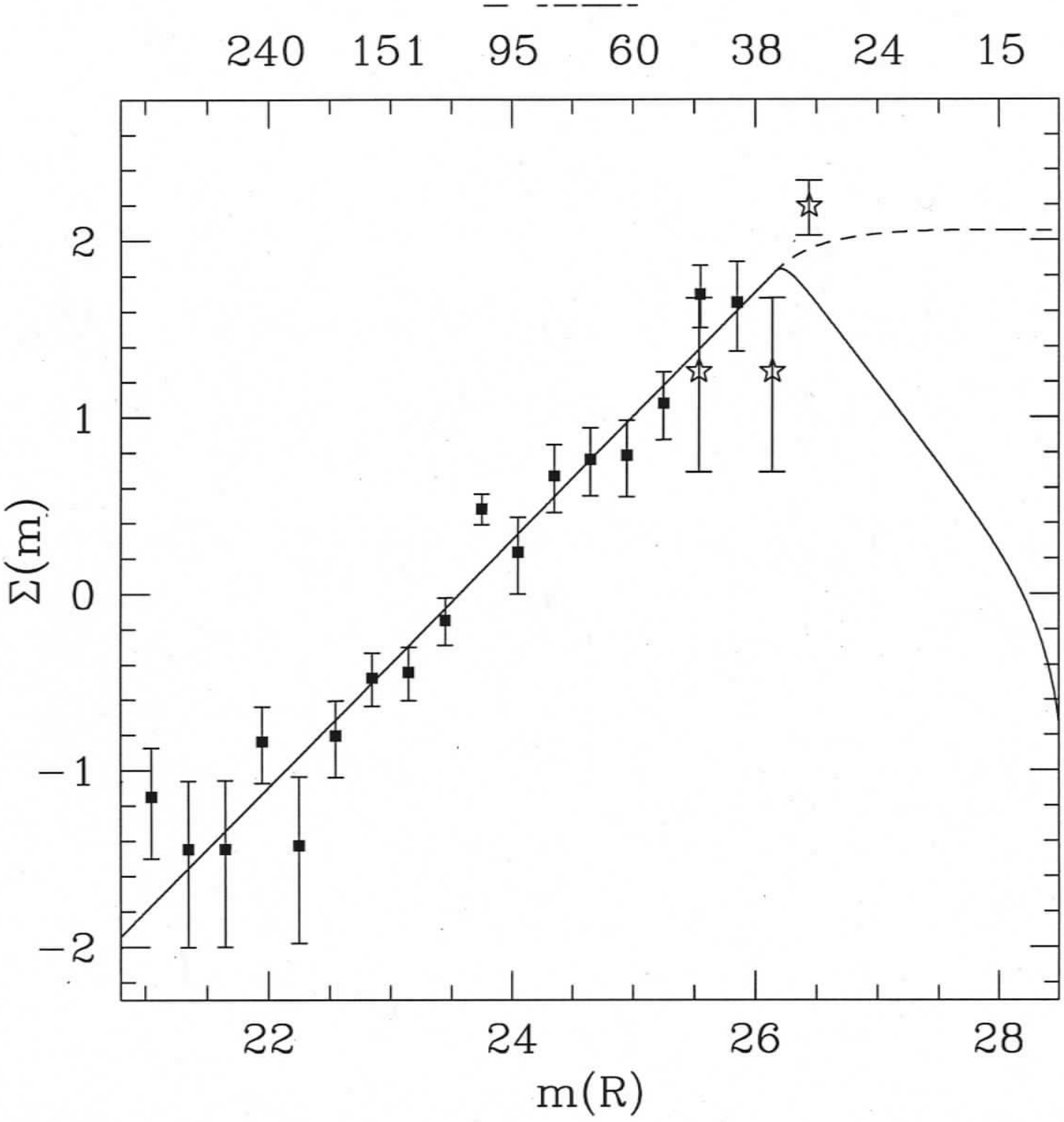

Figure 4.9: Histogram of the data considered in the F08b$_{i>5}$ sample. Errorbars are 1-sigma poisson intervals. The solid curve is the best-fit of Equation 4.5. The dashed curve is the LF expected when α_1, D_b and A are held to their best-fit values, and α_2 is taken at the upper 1-sigma limit, and represents the 1-sigma upper limit to the LF set by the absence of detections with $i > 5$ from *Bernstein et al.* (2004). The stars are the histogram of the Subaru survey presented in this manuscript. These points however, are unreliable as the inclinations for the objects discovered in this survey are highly uncertain. Object diameters (km) are given assuming 6% albedos at 35 AU.

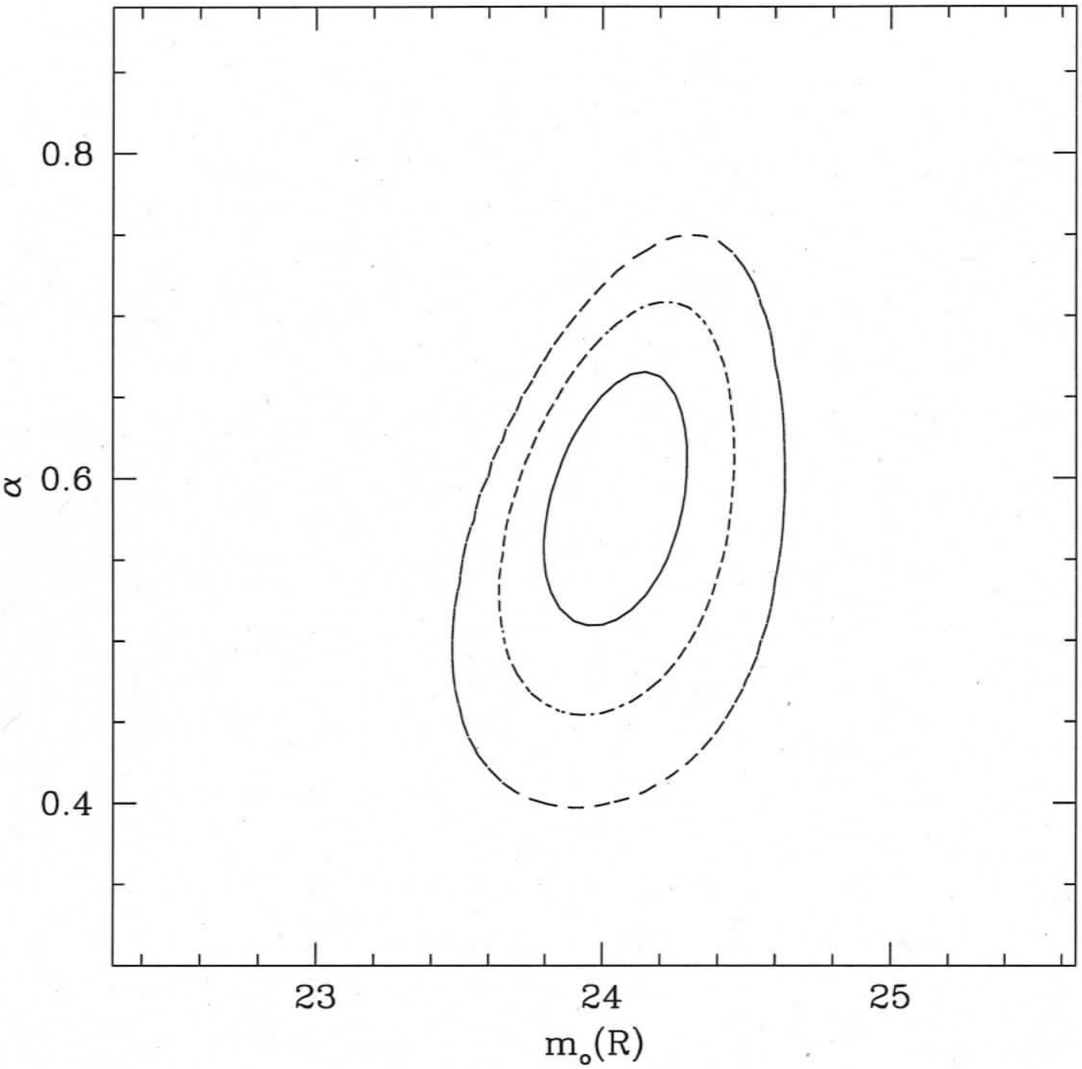

Figure 4.10: The credible regions of the best-fit power-law to the F08b$_{i<5}$ sample. Contours are the 1, 2, and 3-sigma credible regions of the fit. The best-fit power-law is consistent with the collisional equilibrium slope $q = 3.5$ and is a statistically sufficient description of this data-set. THe best-fit broken power-law of the F08b$_{i>5}$ sample is a sufficient description of this data-set.

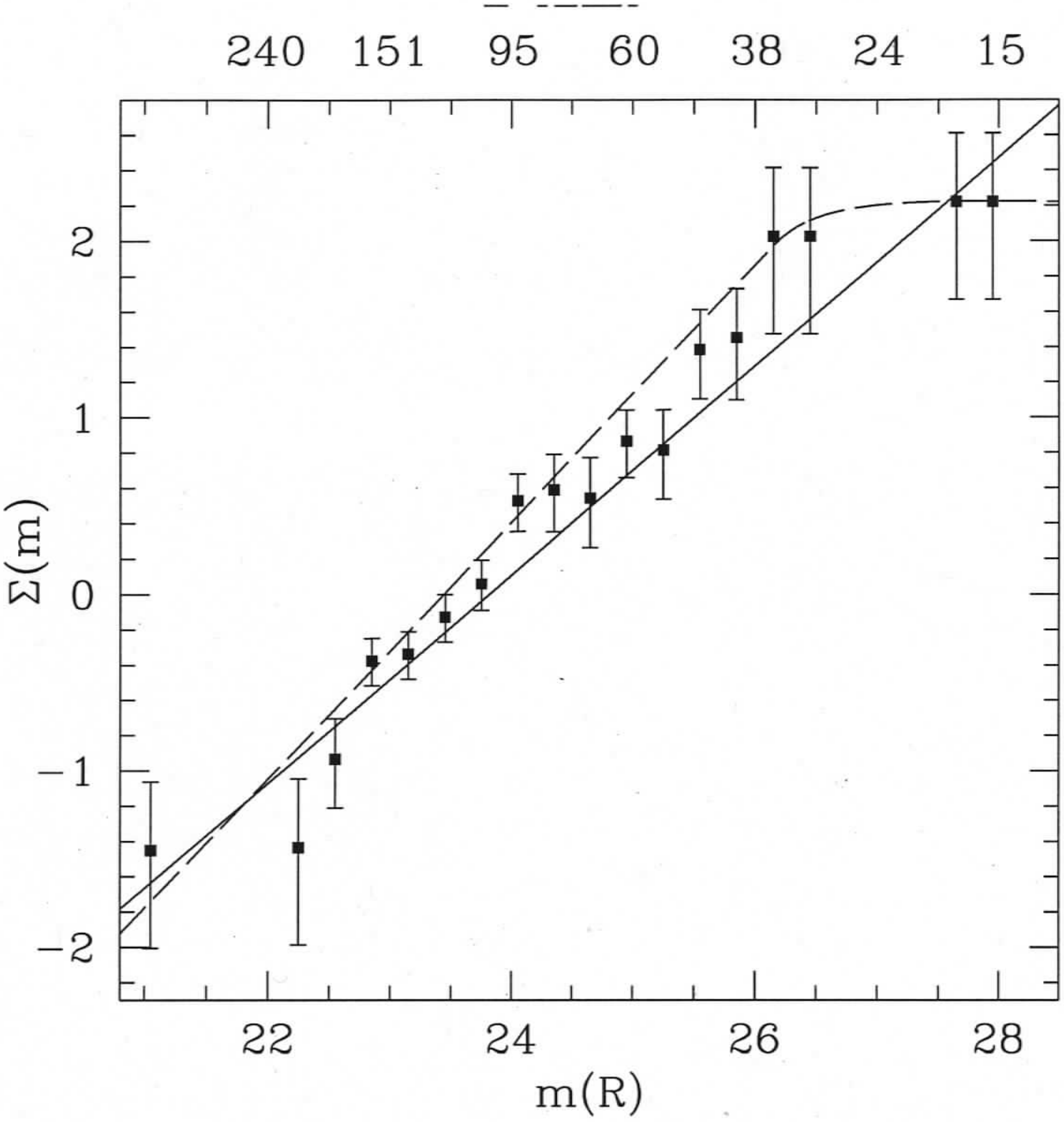

Figure 4.11: Histogram of the data considered in the F08b$_{i<5}$ sample. Errorbars are 1-sigma poisson intervals. The solid curve is the best-fit power-law. Object diameters (km) are given assuming 6% albedos at 35 AU. The dashed line is a broken LF from Equation 4.5 with $(\alpha_1, \alpha_2, D_b, \log A) = (0.7, 0, 34, 22.6)$ and is an adequate description of the data. The dashed curve is consistent at the 1-sigma level with the best-fit LF of the F08b$_{i>5}$ sample.

Chapter 5

Collisional Evolution in the Kuiper belt

Abstract

We have developed a probabilistic cross-sectional collision rate model for a population of planetesimals undergoing collisional evolution. Using a realistic set of destruction and cratering criteria, we have applied this model to the Kuiper belt. We have found that, for planetesimal number densities similar to that in the modern-day Kuiper belt, the observable Kuiper belt size distribution does not evolve appreciably on billion year timescales, for objects larger than a few kilometres radius. We find that a wavy size distribution is produced at object sizes that have undergone substantial collisional evolution.

5.1 Introduction

The Kuiper belt is a population of planetesimals outside the orbit of Neptune. Orbits of the belt members are dynamically excited enough such that the likely result of interactions (collisions) between belt members is ejection mass-loss during cratering, or if the energy is high enough, complete shattering and dispersal of the colliding bodies (*Benz and Asphaug* 1999, *Dell'Oro et al.* 2001). Observations of the Kuiper belt have shown that the large object size distribution is a steep power-law (*Gladman et al.* 2008, *Trujillo et al.* 2001, *Gladman et al.* 2001, *Bernstein et al.* 2004, *Petit et al.* 2006, *Fraser et al.* 2008, *Fuentes and Holman* 2008, *Fraser and Kavelaars* 2008b) consistent with that predicted from accretion scenarios in that region (*Kenyon* 2002).

The preservation of the large object size distribution from accretion in the early Solar system suggests that mutual interactions of large Kuiper belt objects (KBOs) must be infrequent, otherwise the size distribution would have evolved to a shallower slope, or that the existence of excited orbits in the Kuiper belt be a recent phenomenon.

The KBO size distribution has a roll-over from the steep large object slope to a shallower slope for objects $D \lesssim 100$ km (*Bernstein et al.* 2004, *Fraser and Kavelaars* 2008a, *Fuentes and Holman* 2008, *Fraser and Kavelaars* 2008b). This roll-over is likely created by the collisional disruption of objects at the roll-over size, or break diameter and smaller. The observed break diameter is larger than simulations predict for quiescent collisional evolution over the age of the Solar system, even for a massive primordial belt - orders of magnitude more massive than current Kuiper belt - which is required to grow Pluto sized objects in 4.5×10^9 yr. (*Stern and Colwell* 1997a, *Kenyon and Bromley* 2001, *Kenyon* 2002). The observed KBO velocity distribution has higher relative velocities than predicted by those simulations (*Dell'Oro et al.* 2001). Thus, some process excited KBOs onto their current orbits, causing an erosive environment in which the size distribution of objects smaller than $r \sim 100$ km has evolved, producing the large break diameter we see today. This process must have also driven a large scale mass-depletion effectively halting accretion in the Kuiper belt region.

This presents the question: under conditions similar to the modern-day Kuiper belt (low mass, high relative velocities), could the size distribution evolve to its current state on timescales shorter than the age of the Solar system, or did the collisional evolution occur before the Kuiper belt lost the majority of its mass?

We present a model in which, using simple cross-sectional arguments, we calculate the number of disruptive collisions of KBOs as a function of size. Using this model we evolve various size distributions under collisional disruption and track them as a function of time. The purpose of this work is to explore the current collisional state of the Kuiper belt. From these calculations, we wish to determine if the current Kuiper belt size distribution is evolving, and if not, what belt mass is required before the observed size distribution exhibits significant evolution on timescales shorter than the age of the Solar system.

In section 5.2, we discuss the collision model, our adopted model of KBO disruptive strength, and the validity of our method. In section 5.3, we demonstrate the generic size distribution shape our model produces. In section 5.4 we present the outcome of evolving size distributions consistent with current observations, and discuss the implications of these results in section 5.5. Finally, we review our conclusions in section 5.6.

5.2 The Model

Our collisional evolution model considers a swarm of particles distributed in a finite number of size bins, where bin i contains a number of objects, N_i, with radii $r_i - fr_i < r < r_i + fr_i$. In our model we assume that the relative interaction velocity between colliding particles, v_{rel}, is high enough such that interactions do not result in accretion. That is, during a collision a disruption occurs if the relative kinetic energy of the collider is high enough, or the two colliding bodies remain intact as they were before the collision. We do not include velocity evolution in our model, and assume that v_{rel} is a constant during the simulations.

5.2.1 Strength and Fragment Model

Naively, one might expect that the tensile, or material strength (resistance to disruption) of a planetesimal does not depend on size, and is merely a property of the material the makes up the planetesimal. Additionally, one might expect that the contribution by gravity would be some fraction of the planetesimal binding energy. From this, the disruption energy per unit mass should be constant for small bodies where material strength is dominant, and would scale as $r^{5/3}$ for large bodies where gravity dominates. It has been shown however, that for a wide range of materials (ice, basalt, etc.), the disruption energy scales as r^a where $a < 0$ for material strength dominated bodies, and as r^b where $b \sim 1.1 - 1.3$ for gravity dominated bodies (see *O'Brien and Greenberg* 2003, and references therein).

We adopt the catastrophic disruption energy threshold functional form presented by *Benz and Asphaug* (1999). This form includes contributions from the tensile strength of the material body, as well as a gravitational binding term, and is given by

$$Q_D^* = Q_o \left(\frac{r}{1 \text{ cm}}\right)^a + B\rho \left(\frac{r}{1 \text{ cm}}\right)^b \tag{5.1}$$

where Q_D^* is the disruption energy per unit mass of the target body necessary to disperse the target body into a spectrum of fragments. ρ is the target density which we assume is constant for both target and projectile, and Q_o, a, b, and B are constants appropriate for the material properties of icy KBOs.

Benz and Asphaug (1999) utilized a smooth particle hydrodynamic method to simulate the outcome of disruptive collisions between icy bodies. They calibrated Equation 5.1 under a large range of impact parameters (velocity, size ratio, etc.) for both basalt and water ice targets. They found that the disruption energy and hence the constants Q_o, a, b, and B depended on the relative impact velocity. They also found that the mass of the largest remaining fragment M_{LRF} depended linearly on the ratio of the impact energy to the disruption energy, Q/Q_D^* where Q is the relative kinetic energy of the impactor body. They demonstrated that the mass of the largest remaining fragment can be well represented by

$$\frac{M_{LRF}}{M_t} = \gamma = Y + X\left(\frac{Q}{M_t Q_D^*}\right) \tag{5.2}$$

where M_t is the initial target mass. We set the range of γ to be between 0.01 and 1.

By considering values of $\gamma = M_{LRF}/M_t > 0.5$ we include the effects of cratering, ie. disruptive collisions that aren't truly catastrophic, as more than 50% of the primary remains after the collision.

In our simulations we adopt the results of *Benz and Asphaug* (1999) for collisions of water-ice bodies with relative velocities of $v_{rel} = 0.5$ km/s, which is similar to the true impact velocities of KBOs (*Dell'Oro et al.* 2001). These as well as other adopted parameter values are presented in Table 5.1.

We assume that the distribution of collisional fragments is a power-law, and is given by $dN/dr = Ar^{-q_D}$ where q_D is the logarithmic slope. While this is likely not the true distribution, little is known about the true fragment distribution from the disruption of large icy planetesimals. Thus, we choose the power-law as a simple, scale free, two parameter representation that avoids incorporating the unknown physics of fragmentation into the model.

Under the assumption that the density of planetesimals is constant for all sizes, from Equation 5.2 we see that the radius of the largest remaining fragment is

$$r_{LRF} = r_t \gamma^{1/3} \tag{5.3}$$

where r_t is the radius of the target body. Assuming the fragmentation distribution continues to the smallest radii, the normalization of the fragment distribution, A can be found from

$$\int_0^{r_{LRF}} \frac{4}{3}\pi r^3 A r^{-q_D} dr = \frac{4}{3}\pi r_t^3. \tag{5.4}$$

Solving the above, we find $A = (4 - q_D)\gamma^{(q_D-4)/3} r_t^{q_D-1}$ where $q_D \neq 4$. Thus, the number of fragments added to bin j by the disruption of a larger object in bin i is

$$N_{frag}(r_i, r_j) = \frac{(4-q_D)\,\gamma^{(q_D-4)/3} r_i^{q_D-1}}{1-q_D}\left((r_j + fr_j)^{1-q_D} - (r_j - fr_j)^{1-q_D}\right) \tag{5.5}$$

where $q_D \neq 1$.

5.2.2 Collision Rate

From simple collisional cross-section arguments, it can be shown that, if objects from bin i are passing through the swarm of objects from bin j, the number of collisions between the objects from bins i and j, in time-step Δt is

$$N_{coll_{i,j}} = \frac{\pi r_i^2 v_{rel} \Delta t}{V} N_i N_j \tag{5.6}$$

where v_{rel} is the relative encounter velocity, and V is the volume occupied by the swarms of particles. If the collision energy is larger than the disruption condition set by Equations 5.1 and 5.2, then this determines the number of objects removed from size bin i, with a maximum N_i removed per time step.

Because a single disruptive collision will remove an object from a bin, Equation 5.6 does not represent the true number of collisions between bins i and j. One must also consider disruptions of bin i from bin $k \neq j$ for $k \leq i$ as well as disruptions of objects from bin j. We adopt a probabilistic approach. We set the probability that an object from bin i is disrupted by an object from bin j, $P_{i,j}$, as the probability that the disruption of the target i was from an impactor from bin j, $P_{D_{i,j}}$, times the probability that an object j was available to cause the disruption, P_j.

$P_{D_{i,j}}$ is simply given by the number of collisions of objects from bin i by those from bin j, from Equation 5.6, divided by the number of objects in bin i. That is $P_{D_{i,j}} = \frac{N_{coll_{i,j}}}{N_i}$.

The probability that impactor j is available can be found by setting $P_j = 1 - \bar{P}_j$

where $\bar{P}_j$ is the probability that an object j has a disruptive collision with objects from any bin $k \neq i$, for k larger and smaller than j. That is, $P_j = 1 - \frac{\sum_{k\neq i} N_{coll_{j,k}}}{N_j}$. The true number of disruptive collisions from bin i by bin j is then

$$N_{disrupt_{i,j}} = N_i P_{D_{i,j}} \left(1 - \bar{P}_j\right) . \tag{5.7}$$

5.2.3 Model Parameters and Initial Conditions

To define a particular simulation, initial conditions and model parameters must be defined. For the calculations we present here, we wish to estimate the evolution of the observed size distribution for a range of Kuiper belt densities. Thus, we vary the initial size distribution and number of KBOs. We set other model parameters to match those typical of KBOs and save discussion of their effects for a future work. All model parameters are summarized in Table 5.1.

To study the current KBO collisional evolution, we define an initial Kuiper belt which mimics the observed size distribution. *Fraser and Kavelaars* (2008b) present a measure of the Kuiper belt luminosity function, from which they infer that $q_1 \sim 4.8$ and turns over to $q_2 \sim 2$ at $D_{b,1} \sim 60$ km. From accretion simulations, the size distribution turns-up again at diameters of a few 100 m to a collisional cascade of slope $q_{eq} \sim 3.5$, in which the number of objects of a given size disrupted is replaced by fragments from disruptions of larger objects (see for example *Kenyon* 2002).

Inspired by these results, we consider size distributions that exhibit roll-overs spanning the 1-sigma uncertainty range of the size distribution presented by *Fraser and Kavelaars* (2008b). We choose three separate initial size distribution S1, S2, and S3 with breaks given by: $(D_b, q_2) = (50 \text{ km}, 0)$, $(D_b, q_2) = (65 \text{ km}, 2)$, and $(D_b, q_2) = (90 \text{ km}, 3.5)$ respectively. The measured uncertainty on the large object slope parameter, q_1, reported by *Fraser et al.* (2008) is small compared to that of D_b and q_2. Thus we set $q_1 = 4.8$ for all of our simulations as the majority of the size distribution evolution will occur at smaller size, where the current observations are most uncertain.

Trujillo et al. (2001) inferred from their ecliptic Kuiper belt survey that the number of objects with radius $r > 100$ km, $N(r > 100) \sim 5 \times 10^4 - 5 \times 10^5$ in the Kuiper belt. Their estimate was based off a large object size distribution almost identical to that observed by *Fraser et al.* (2008), and thus still represents a reasonable estimate for the number extant large KBOs. In our simulations we consider three initial KBO densities: N1, N2, and N3, corresponding to $N(r > 100) = 4.5 \times 10^4$, $N(r > 100) = 4.5 \times 10^5$, and $N(r > 100) = 4.5 \times 10^6$ objects with $r > 100$ km respectively.

The simulations of *Benz and Asphaug* (1999), provide estimates of the strengths of icy bodies and the fragment distribution from a disruption event. Hence, we use their results as calibration to Equation 5.1, and the largest remaining fragment size, r_{lrf}, given by Equations 5.2 and 5.3. They found $(Q_o, B, a, b, X, Y) = (7.0 \times 10^7, 2.1, -0.45, 1.19, \frac{7}{6}, \frac{2}{3})$ provides a good fit to the simulation results, where Q_o and B are in units of ergs g^{-1} and ergs cm ^{3} g^{-2}. We assume these parameter values for models. Note: values of X and Y were not explicitly presented by *Benz and Asphaug* (1999) but were instead chosen as suitable parameters to fit the relation presented in Figure. 9 of that work.

For our models, we assume that the Kuiper belt swarm uniformly occupies a cylindrical shape with inner and outer edges of 30 and 60 AU, with a total height of 40 AU which gives a total swarm volume, $V = 3.4 \times 10^5$ AU^3. While this assumption does not accurately reflect the true KBO orbital distribution, or radial extent, it is a sufficient approximation for the simple cross-sectional collision rates we calculate here.

Dell'Oro et al. (2001) calculate the average relative collision velocity for Kuiper belt objects. They found that v_{rel} depended on the dynamical classes of the colliding bodies, and ranged from ~ 0.5 to 3 km s^{-1}. For our models, we set $v_{rel} = 1$ km s^{-1}.

Finally, for our models we set the size bin width ratio as $f = 1.075$, the time step as $\Delta t = 2.5 \times 10^{-3}$ Myr, and the minimum bin-size as $r_{min} = 0.1$ cm. These parameters were chosen as a compromise between maintaining accuracy in the size distribution results, and keeping the simulation run-times from being excessively long. We also set $\rho = 2$ g cm^{-2} as typical for ice bodies. We introduce the notation NiSj to refer to a simulation with the parameters described above, the initial size distribution Sj, and large object density Ni.

5.3 Model Behavior

To demonstrate the general results of our simulations, we present model N3S3 after 100 Myr in Figure 5.1. From this figure, four separate regions in the evolved size distribution are apparent. The first is for the largest objects with $r \gtrsim 10$ km, where few disruptive collisions have occurred, approximately preserving the initial size distribution. For objects with $0.01 \lesssim r \lesssim 10$ km, a wave-like structure similar to that predicted by *O'Brien and Greenberg* (2003) is produced. Such 'waves' are produced for objects larger than a radius at which a sharp change in the size distribution slope occurs.

The third region is found when the number of collisions for objects in a bin in a time-step is equal to the number of objects in that bin. In this region, the results of these simulations cannot be trusted. To understand the evolution of objects at a particular size, a time-step must be chosen such that the number of collisions in a bin per time-step is a small fraction of the population for the bin-size of interest. The fourth region is found where the slope of the size distribution turns up near the r_{min}. The turn-up is caused by the artificial cut-off of the objects at the minimum size, and therefore an artificial cut-off in the available colliders.

To determine the effects of varying the non-physical model parameters, f, r_{min}, and Δ_t, we consider five instances of the N3S3 simulation. In each of the instances we vary one of f, Δt, or r_{min} and run the simulation for 100 Myr. We present the end-result of these simulations in Figures 5.2 and 5.3. As can be seen from Figure 5.2, increasing r_{min} has no substantial effect on objects with $r > 0.1$ km, but does modify the distribution below this point. As well, we find no substantial difference in the size distribution when the bin-size is doubled.

From Figure 5.3, the evolution of the size distribution is strongly dependent on the choice of Δt. The resultant size distribution is not modified after 10 Myr for $r \gtrsim 5$ km when the time-step is reduced by a factor of 10. The size at which this statement is valid will depend on the length of the simulation, as well as the size distribution of the objects. For the simulations with low densities (N1 and N2) we conclude that the results of our simulations accurately estimate the evolution of the size distribution for $r > 5$ km, with this radius being larger for high density simulations. Below this size, only the general behavior of the size distribution can be trusted, and conclusions about the specific shape of the size distribution must be avoided.

5.4 Simulation Results

In Figures 5.4, 5.5, 5.6, 5.7, 5.8, 5.9, 5.10, 5.11, 5.12 we present the results of the simulations at 0, 250, 500, 750, and 1000 Myr. We also present a comparison of the 1-sigma range of the inferred roll-over parameters, q_2 and D_b, from *Fraser and Kavelaars* (2008b) with our simulations. As can be seen from these results, for large objects above the initial break radius, only a few have been disrupted over 1 Gyr, and thus the initial large object slope q_1 is effectively preserved over the age of the simulations. For smaller objects however, if the number of disruptors is high enough, a significant amount of collisional processing occurs.

For the N1 simulations which are the simulations which has the minimum number of Kuiper belt objects consistent with observations, we see that minimal disruption of kilometer and larger sized bodies has occurred, even after 1 Gyr. After 1 Gyr, the results of all N1 simulations demonstrate that the size distribution is still consistent (or nearly so) with that inferred from *Fraser et al.* (2008). Only simulation N1S3, which has the steepest size distribution, and hence the largest number of bodies capable of disrupting kilometer sized bodies, displays collisional disruption for objects as large as 10 km. This produces a kink in the distribution at ~ 25 km, beyond which, the size distribution for objects $1 \lesssim r \lesssim 15$ km has a slope very similar to the initial size distribution break slope q_2. Simulation N1S1 demonstrates slightly opposite behavior, in that, so few disruptive collisions occur for ~ 1 km objects, that a build-up of fragments from the sporadic disruption of larger objects occurs, lifting the slope steeper than the initial value.

The N1 simulations demonstrate that if the size distribution breaks to the small object slope $q_2 \sim 3$ at radii $\sim 20 - 40$ km, collisional evolution would occur in the current Kuiper belt at non-neglibible rates ($\sim 5 \times 10^{-3}$ yr^{-1}) for objects $10 \lesssim r \lesssim 30$ km, and can last for more than 1 Gyr without producing a size distribution inconsistent with that observed. If the roll-over occurs to shallower slopes $q_2 \lesssim 2$, then the size distribution for radii to which current observations are sensitive ($r \gtrsim 10$ km) undergoes minimal modification, and is preserved for longer than 1 Gyr.

For the N2 simulations, which have an order of magnitude larger initial number of KBOs than in the N1 simulations, we find the large objects, while more numerous still experience minimal collisional disruption. In all of the simulations, objects smaller than the initial break radius experience rapid collisional evolution. After 500 Myr, the resultant size distributions of the N2 simulations have evolved substantially. Indeed, the N2S1 simulation is only marginally consistent with the observations at 500 Myr, and is inconsistent with the observations at the end of the simulation. These results suggest that if the current Kuiper belt contained as many as 5×10^5 objects larger than 100 km and has a break slope q_2 steeper than 0, enough collisional depletion of objects similar in size to the initial break would occur over a timescale less than a billion years such that the size distribution would only be consistent with the observations if the uncertainty range of the observations is re-normalized.

For the N3 simulations, which have 2 orders of magnitude larger initial numbers of KBOs than in the N1 simulations, we find objects as large 100 km undergo substantial collisional evolution over the age of the solar system, and the resultant size distributions are inconsistent with the observations, regardless of the initial size distribution. Thus we conclude that the Kuiper belt cannot have as many as 10^6 objects larger than 100 km in the volume presented.

5.5 Discussion

Our findings have demonstrated that the number of large ($r \gtrsim 100$) KBOs must be $\lesssim 5 \times 10^5$, consistent with the findings of *Trujillo et al.* (2001). Otherwise collisional evolution over a period much shorter than the age of the Solar system would produce a size distribution different than what we observed. If the number of KBOs larger than 100 km is $\sim 5 \times 10^5$, then the size distribution must be very flat for $r \lesssim 25$ km to preserve a size distribution consistent with observations.

These results also demonstrate that the current KBO density is too low to produce the observed break. Indeed, only when the number of large $r > 100$ km objects is $\sim 10^6$ is evolution rapid enough to substantially alter the break location on timescales shorter than the age of the solar system. This suggests that the knee was produced by collisional evolution in an environment in which KBOs, and hence collisions were more numerous. Once the size distribution was similar to what we observe today, some event must have depleted most of the initial mass, effectively halting collisional evolution. What we are left with is the small remaining population, with an observable size distribution that has been effectively unaltered since the mass depletion event. With the current observed density in the Kuiper belt, the size distribution can remain as it is for time-scales similar to the age of the Solar system.

When the mass of the Kuiper belt is of order 30 $M_\oplus$ - about that required to form Pluto sized KBOs (*Stern and Colwell* 1997a, *Kenyon* 2002) - the timescale for the break diameter to evolve from $\sim$ 60 km to larger sizes is a few 100 Myr. It is likely that the timescale to evolve *to* this size is the same order of magnitude. This implies that the mass depletion took of order a few 100 Myr, leaving just enough time to produce the current size distribution, before the mass was too low for collisional evolution to occur.

The mass depletion timescale of the Kuiper belt is similar to that found by *Bottke et al.* (2005) for the asteroid belt. They found that the current observed break in the asteroid size distribution ($D_b \sim$ 120 km) could be produced if the asteroid belt underwent orbital excitation from interactions with Jupiter. The dynamical excitation depleted more than 95% of the initial asteroid belt mass after nearly 100 Myr, at which point collisional evolution of the large asteroids was halted.

It is attractive to think that the asteroid belt and the Kuiper belt underwent similar formation scenarios, ie. a short period of accretion, followed by a dynamical excitation and mass depletion from interactions with a gas giant (Jupiter for the asteroids, Neptune for KBOs) during which, the size distribution of the belts undergoes substantial collisional evolution. This is then followed by a quiescent state where collisions of large planetesimals are extremely rare.

The similarity of the depletion timescales for both belts suggests that the depletion events of the asteroid and Kuiper belts are coupled. This is a conceivable notion, as the dynamics of Jupiter and Neptune are coupled. Consider the Neptune migration scenario. For Neptune to experience outward migration, planetesimals must first transfer momentum to Neptune during a scattering event. A second scattering with Jupiter throws these planetesimals out of the Solar system, preventing further scatterings with Neptune. The result is that Neptune migrates outward, while Jupiter migrates inward. In this scenario, the depletion of the two belts is coupled with the migration timescale, and hence both belts have similar depletion timescales. This scenario however, is likely not the only one in which the depletion timescales of the asteroid and Kuiper belts are similar or coupled.

It is interesting to note that in none of our simulations in which substantial large object evolution occurs do we produce results like that of *Kenyon and Bromley* (2001), *Kenyon* (2002), *Kenyon and Bromley* (2004), ie. a size distribution that exhibits a smooth roll-over between two well defined power-laws. Instead our results are similar to those from *Stern and Colwell* (1997a) who predict a size distribution that is reasonably well represented by a power-law for large objects, but demonstrates a wavy structure at smaller sizes. Our simulations suggest that the size distribution for objects small enough to have undergone substantial collisional processing is not a power-law at all, but rather a function whose shape depends on the amount of evolution that has occurred for these objects. It is likely however, that until substantially deeper and more numerous observations of KBOs are made, in which distance and size can be disentangled, the wavy signature of the size distribution will be washed out, resulting in an apparent power-law for the observed size distribution.

This work has shown the necessity of the use of a short time-step to generate trustworthy size distributions. More desirably, in our future works, we will adapt this model to make use of an adaptive time-step that varies with the percentage number of collisions in a size bin. This will ensure accurate results over the entire size range. Additional improvements can be made with an accurate prescription of small object removal by radiation pressure and Poynting-Robterson drag which can remove 0.1 mm sized dust grains from the Kuiper belt region in a few 10's of Myr. This would ensure a reliable estimate of the behavior of the small object distribution. Additional simulations should also be run that probe a range of strength models, and relative velocities to study their effects on the resultant size distribution.

At the end of the simulations, the N1, N2, and N3 models have ~ 4, ~ 34, and ~ 120 Earth masses of material in the size range we simulate. This mass is large enough such that, at least for the N2, and N3 simulations, accretion should occur *Kenyon* (2002). *Arakawa and Tomizuka* (2004) has demonstrated that the typical ejecta velocity of an impact cratering event is similar to the relative impact velocity. Thus, accretion (not cratering) is possible only for objects with an escape velocity similar to, or greater than the relative impact velocity. With $v_{rel} \sim 1\text{km s}^{-1}$ typical for the Kuiper belt, the minimum size where accretion can occur is $r \sim 1000$ km. Accretion can only occur for impactors ~ 1 order of magnitude smaller than the parent body, otherwise disruption is the outcome. Thus, we expect that accretion in the modern day Kuiper belt will allow Pluto-sized objects to grow by collision of objects larger than the break radius, where disruption is not a frequent occurrence, and with $r \lesssim 100$. In our future works, accretion will be included as a possible collisional outcome.

5.6 Conclusions

We have developed a probabilistic collision model that, based on simple cross section arguments, calculates the disruptive collision rates as a function of object size. We have included a realistic strength model of icy planetesimals, and have used this model to estimate the time-dependent evolution of different size distributions consistent with that observed for the Kuiper belt.

We find that, for the range of KBO densities observed, the size distribution does not evolve appreciably on billion year timescales. Some evolution of the observable population ($r \gtrsim 5$ km) can occur on these timescales if the roll-over at $r \sim 30$ km observed in the Kuiper belt size distribution (*Bernstein et al.* 2004, *Fuentes and Holman* 2008, *Fraser and Kavelaars* 2008b) changes to a steep $q_2 \sim 3.5$ slope.

We find that, even for KBO densities 1-2 orders of magnitude higher than that

Table 5.1: Adopted Simulation Parameters. Y and X are chosen as nominal parameters which well represent the fit presented in Figure 9 of *Benz and Asphaug* (1999). Parameter values given are the values chosen for the nominal model.

	Planetesimal Strength Parameters	
Q_o	material strength normalization	7×10^7 erg g^{-1}
a	material strength slope	-0.45
b	gravitational strength slope	1.19
B	gravitational strength normalization	2.1 erg cm^{3}g$^-$2
	Fragment Distribution Parameters	
Y	r_{lrf} parameter	$\frac{7}{6}$
X	r_{lrf} parameter	$\frac{2}{3}$
q_D	fragment distribution slope	2.0
	Planetesimal Swarm Parameters	
V	swarm total Volume	3.4×10^5 AU^3
v_{rel}	relative interaction velocity	1 kms^{-1}
	Simulation Parameters	
f	size bin width ratio	1.075
Δt	simulation time-step	2.5×10^{-3} Myr
r_{min}	minimum size bin	0.1 cm

currently observed, catastrophic collisions of larger objects are sporadic and infrequent. Thus, the size distribution of objects larger than the roll-over diameter is preserved on billion year timescales This demonstrates that the large object slope currently observed in the Kuiper belt is primordial, and presumably leftover from accretion.

Finally, we find that our model does not produce a size distribution that breaks to a power-law below the roll-over diameter, but rather a wavy function, the shape of which depends on the simulation parameters. This wavy signature might be observed with much more substantial efforts in determining the KBO size distribution.

Table 5.2: Initial Size Distributions and Densities. For all simulations, the large object size distribution is $q_1 = 4.8$, and all size distributions turn up to small object slope $q_3 = 3.5$ at $r = 100$ m.

Simulation	Break Radius r_b (km)	Break Slope q_2
S1	25	0
S2	32	2
S3	45	3.5

Initial Number	$(N > 100)$ km
N1	4.5×10^4
N2	4.5×10^5
N3	4.5×10^6

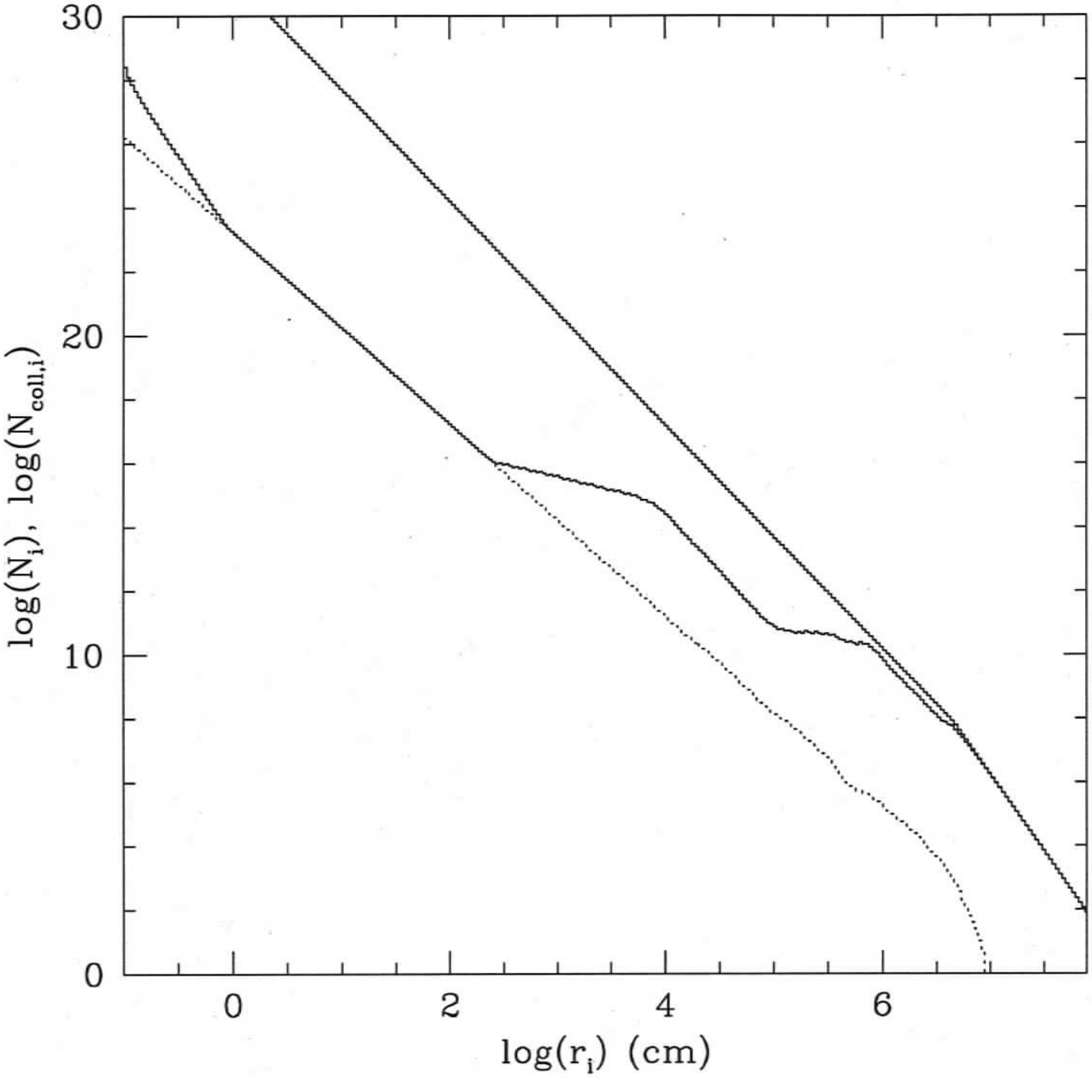

Figure 5.1: The initial size distribution (solid line) and evolved size distribution (wavy solid line) and the number of collisions per time-step for the N3S3 simulation after 100 Myr. A wave-like structure is produced where a significant fraction of the initial population has been collisionally disrupted. Model results are inaccurate when the number of collisions per time-step is similar to the number of objects per time-step, ie. at the intersection of the solid and dotted lines.

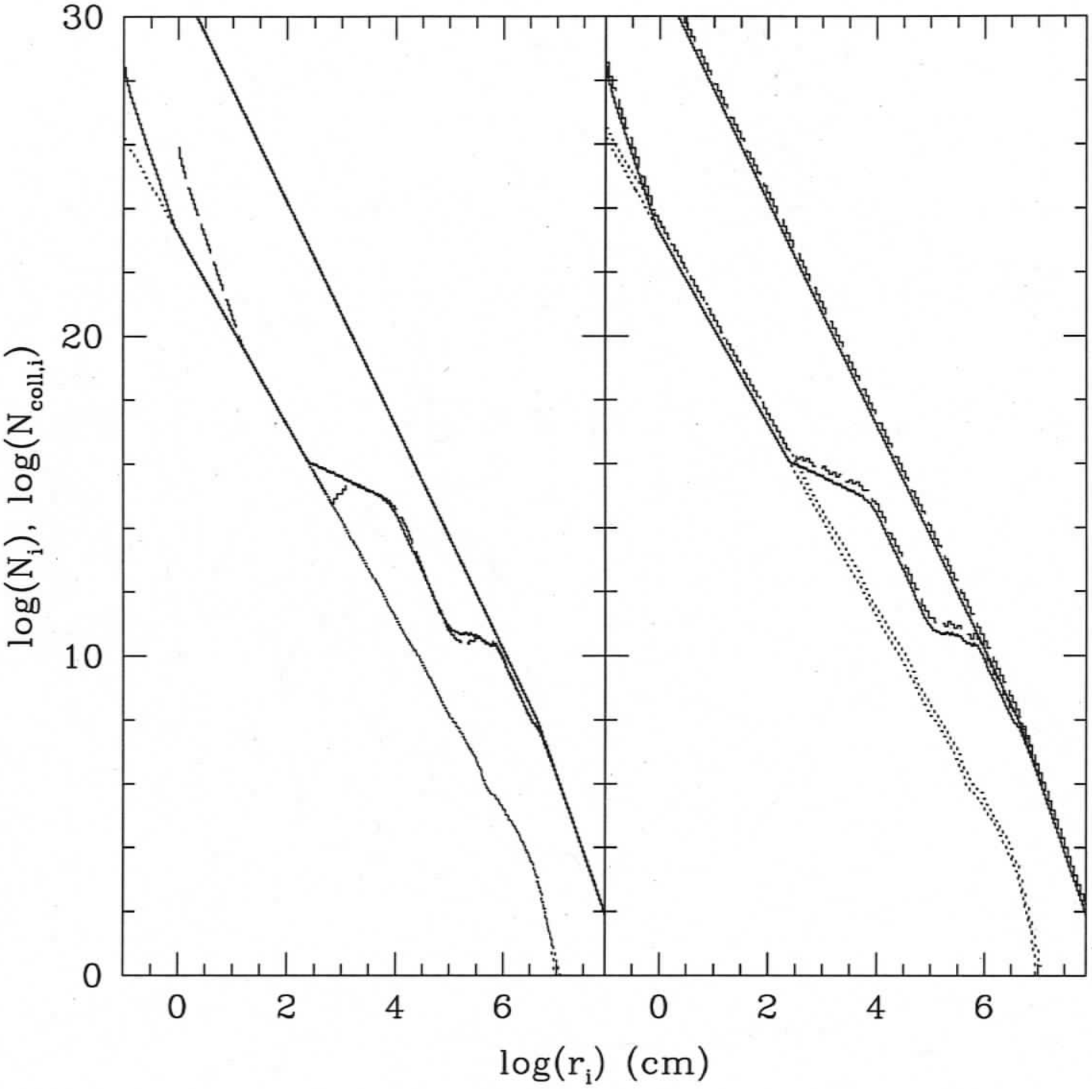

Figure 5.2: *Left:* As Figure 5.1. Dashed line is the N3S3 simulation, but with a r_{min} a factor of 10 larger. *Right:* As Figure 5.1. Dashed line is the N3S3 simulation, but with $f = 1.15$. The initial number of objects in these simulations is the same.

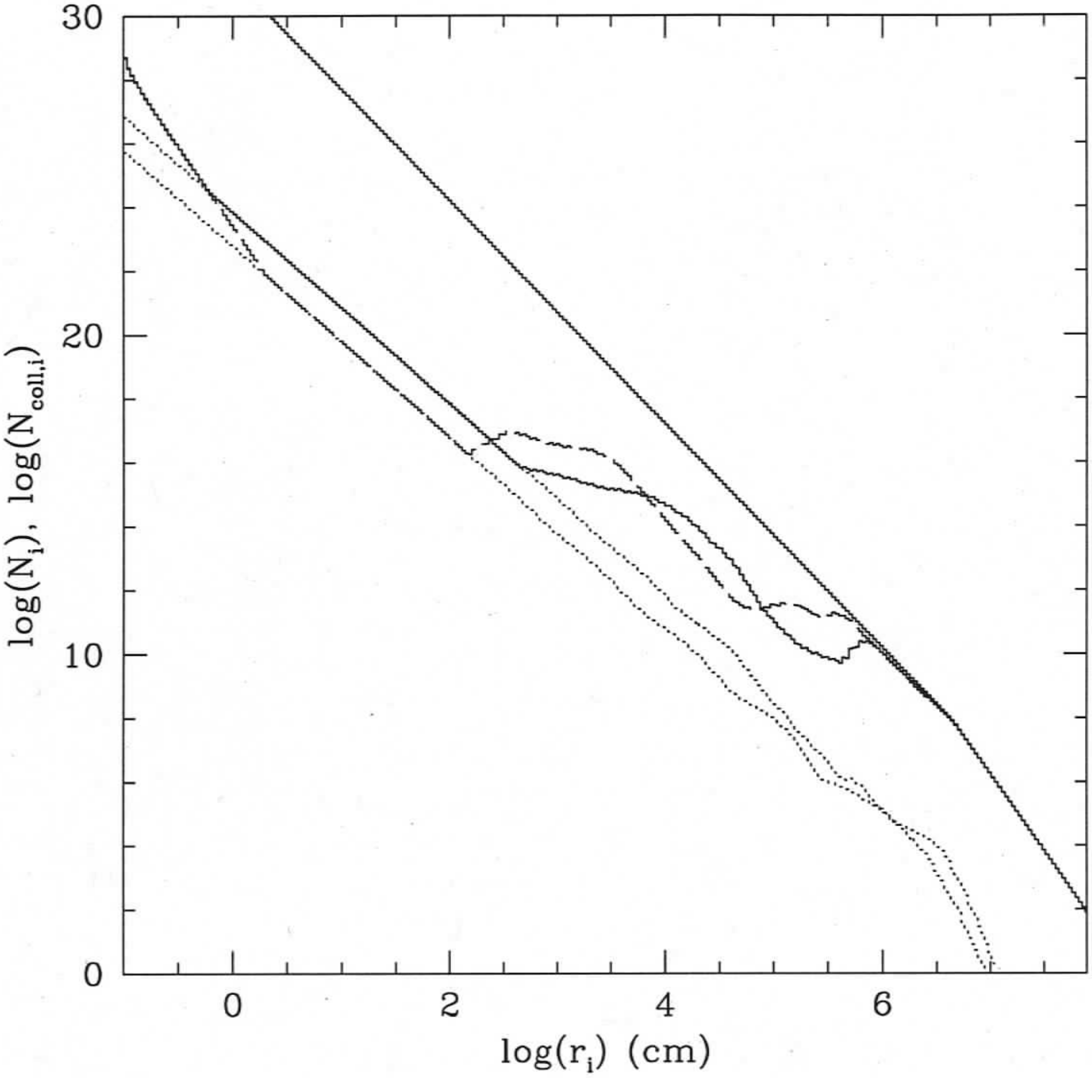

Figure 5.3: As Figure 5.1 after 10 Myr. Dashed line is the N3S3 simulation, but with $\Delta t = 2.5 \times 10^{-2}$, ie. a factor of 10 smaller then in the N3S3 simulation. The simulations with different time-steps produce the same results for $r \gtrsim 10^{5.9}$.

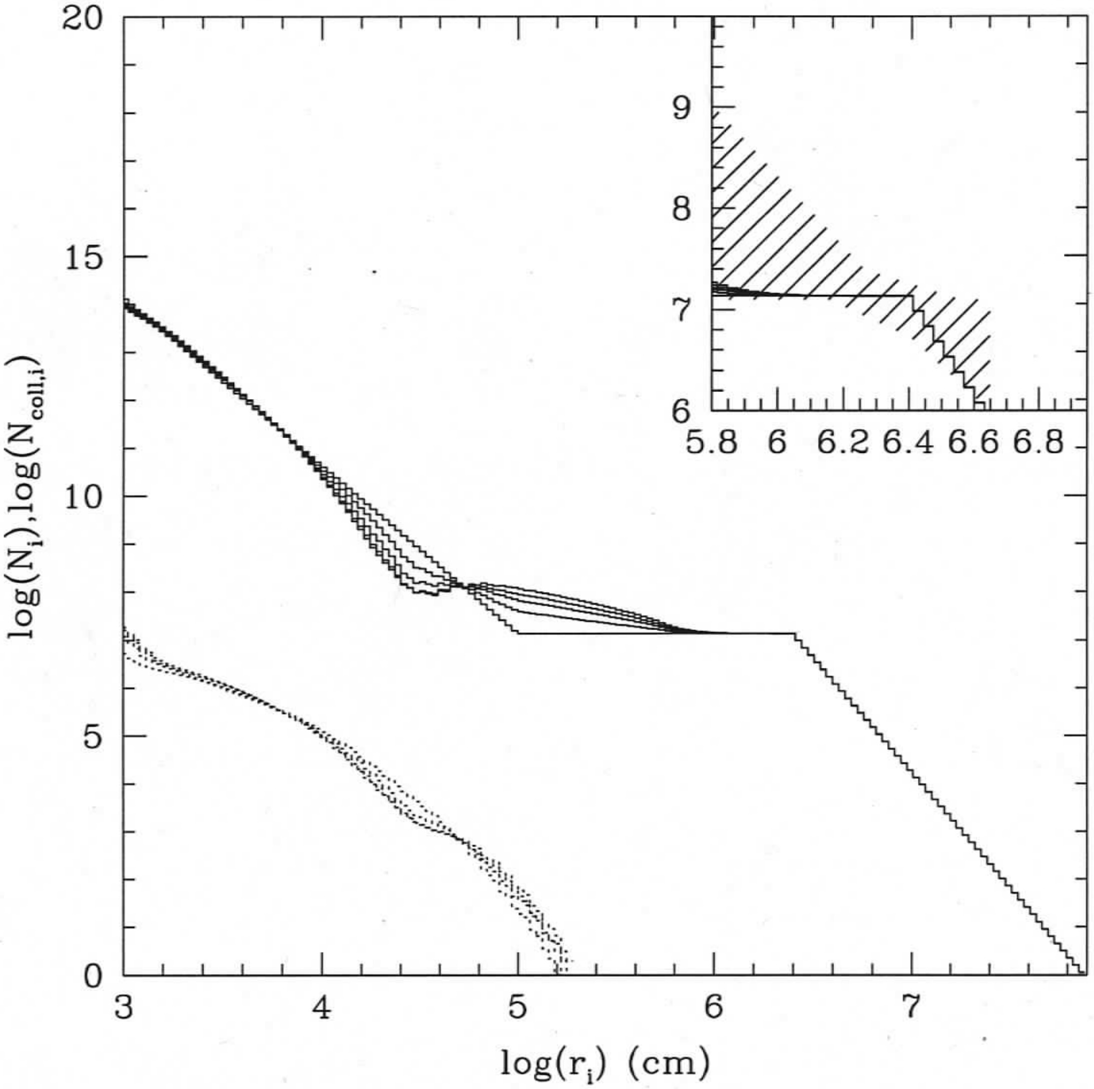

Figure 5.4: Results of simulation N1S1. Presented is the size distribution (solid lines), and number of collisions per time-step per bin (dotted lines) at simulation time 0, 250, 500, 750, and 1000 Myr. Inset is a zoom of the region of the size distribution where current observations are sensitive to (*Fraser and Kavelaars* 2008b). The dashed region in the inset, marks the 1-sigma range of the break slope, q_2, and the break diameter, D_b, observed by *Fraser et al.* (2008).

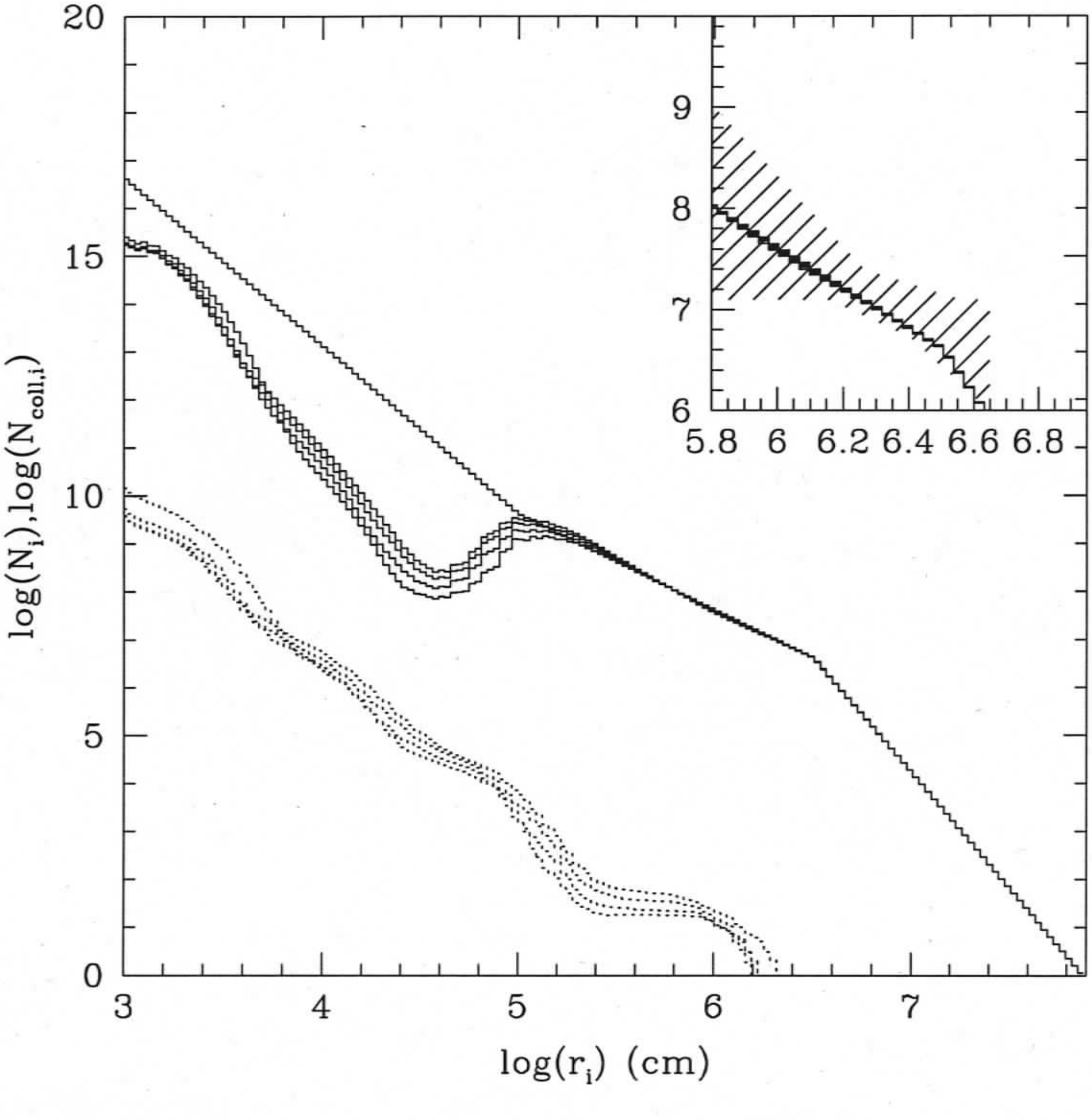

Figure 5.5: Results of simulation N1S2. Presented is same as in Figure 5.4.

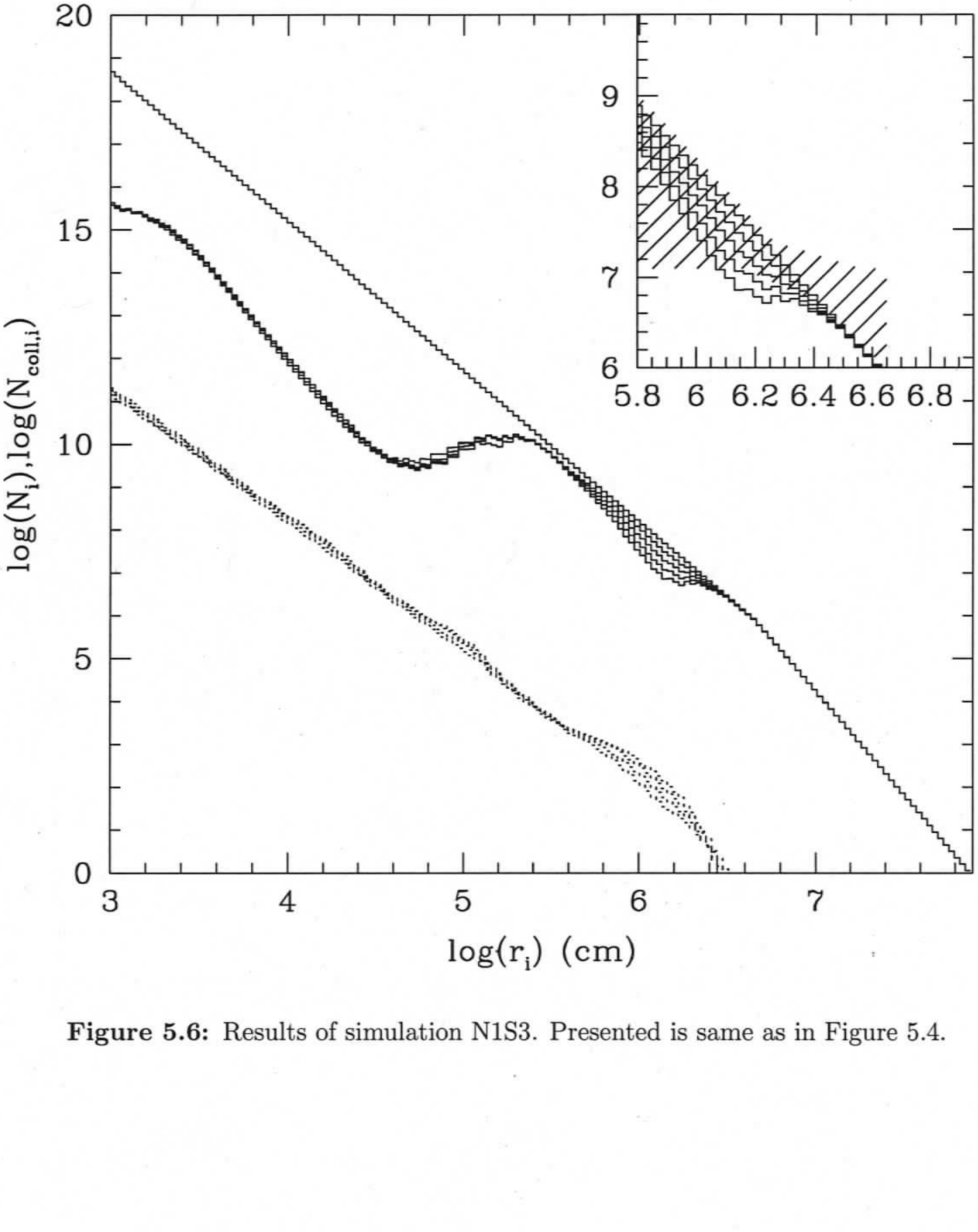

Figure 5.6: Results of simulation N1S3. Presented is same as in Figure 5.4.

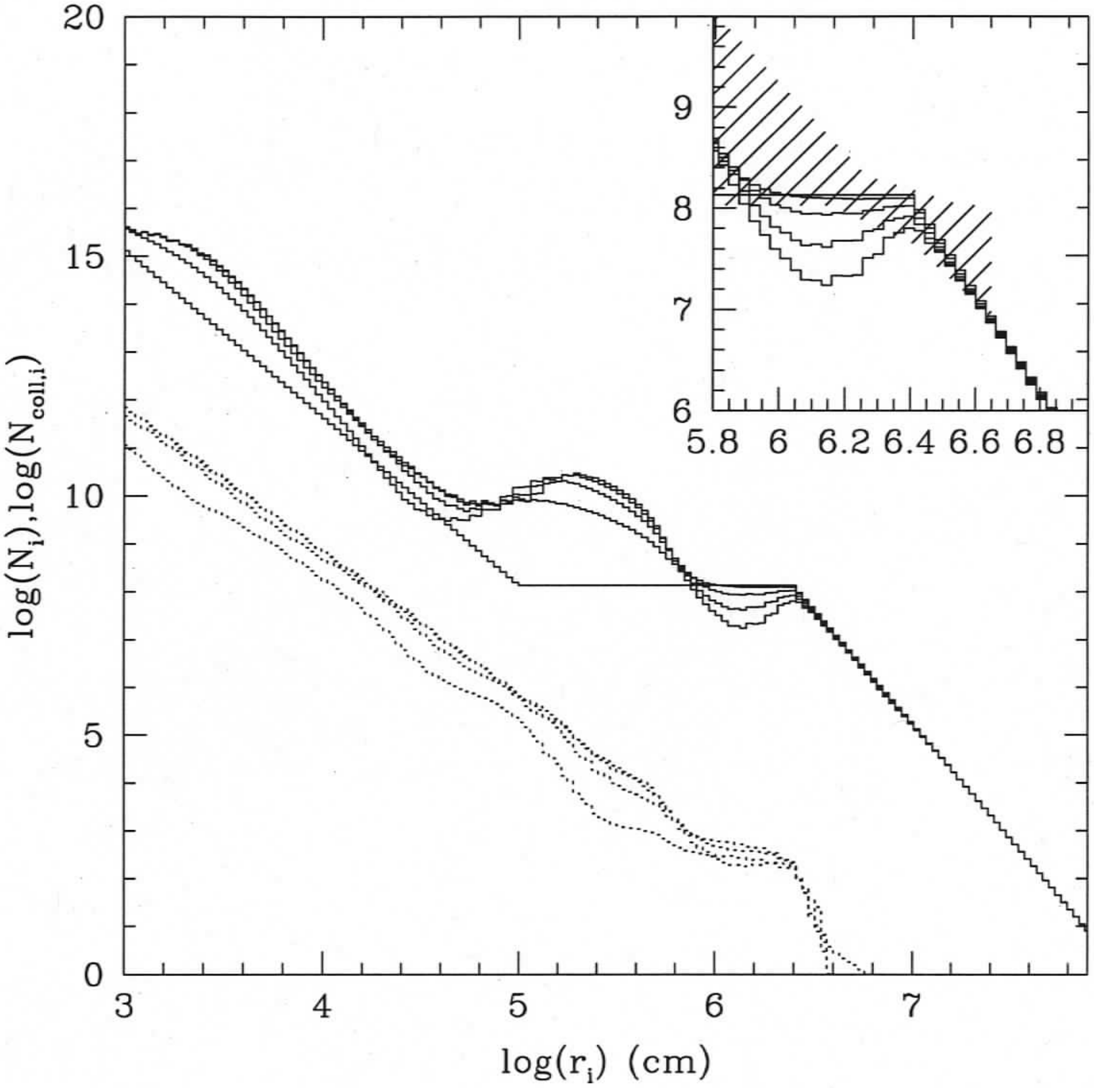

Figure 5.7: Results of simulation N2S1. Presented is same as in Figure 5.4. The dashed region in the inset, has been scaled vertically to match the initial size distribution.

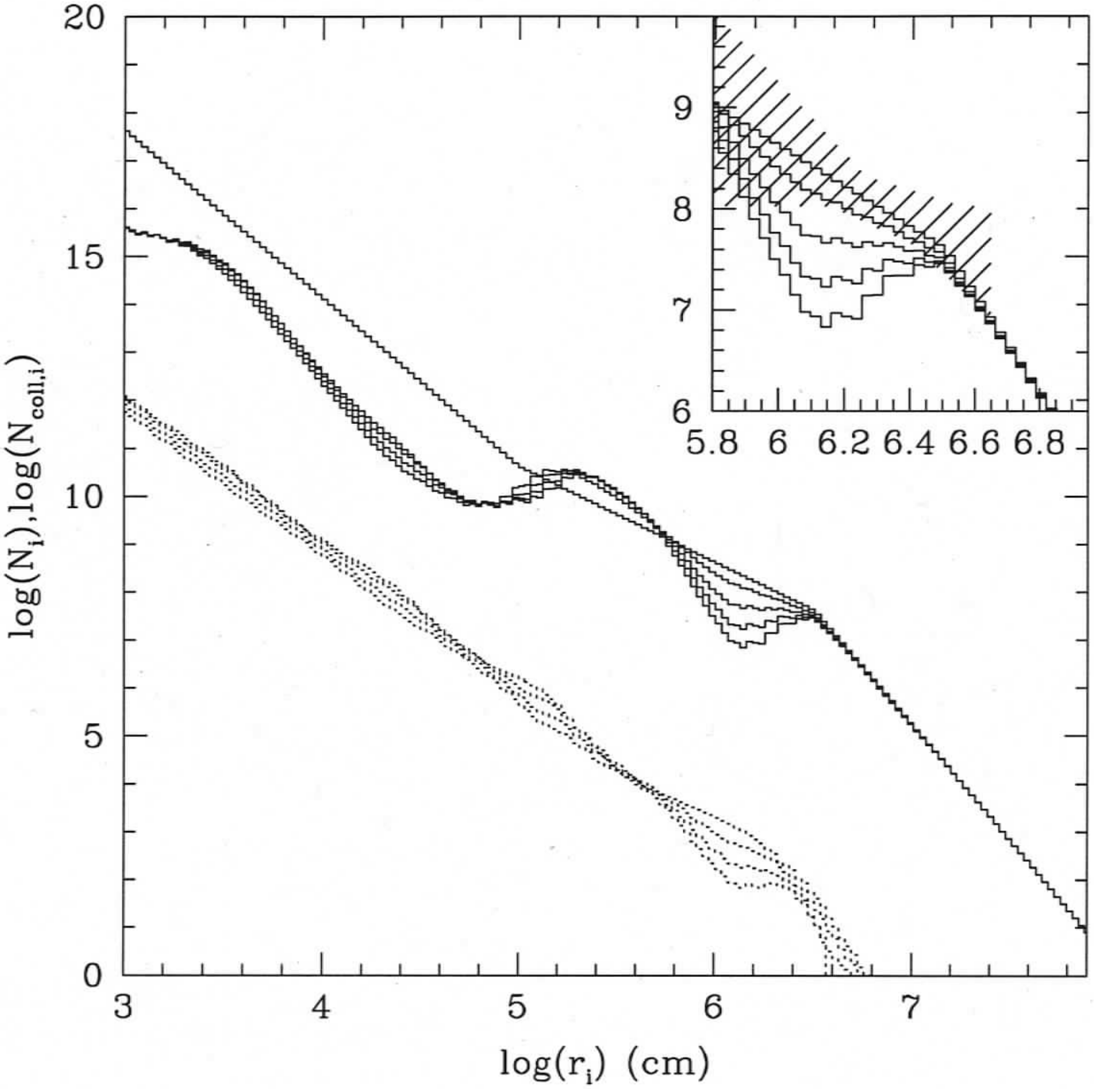

Figure 5.8: Results of simulation N2S2. Presented is same as in Figure 5.4. The dashed region in the inset, has been scaled vertically to match the initial size distribution.

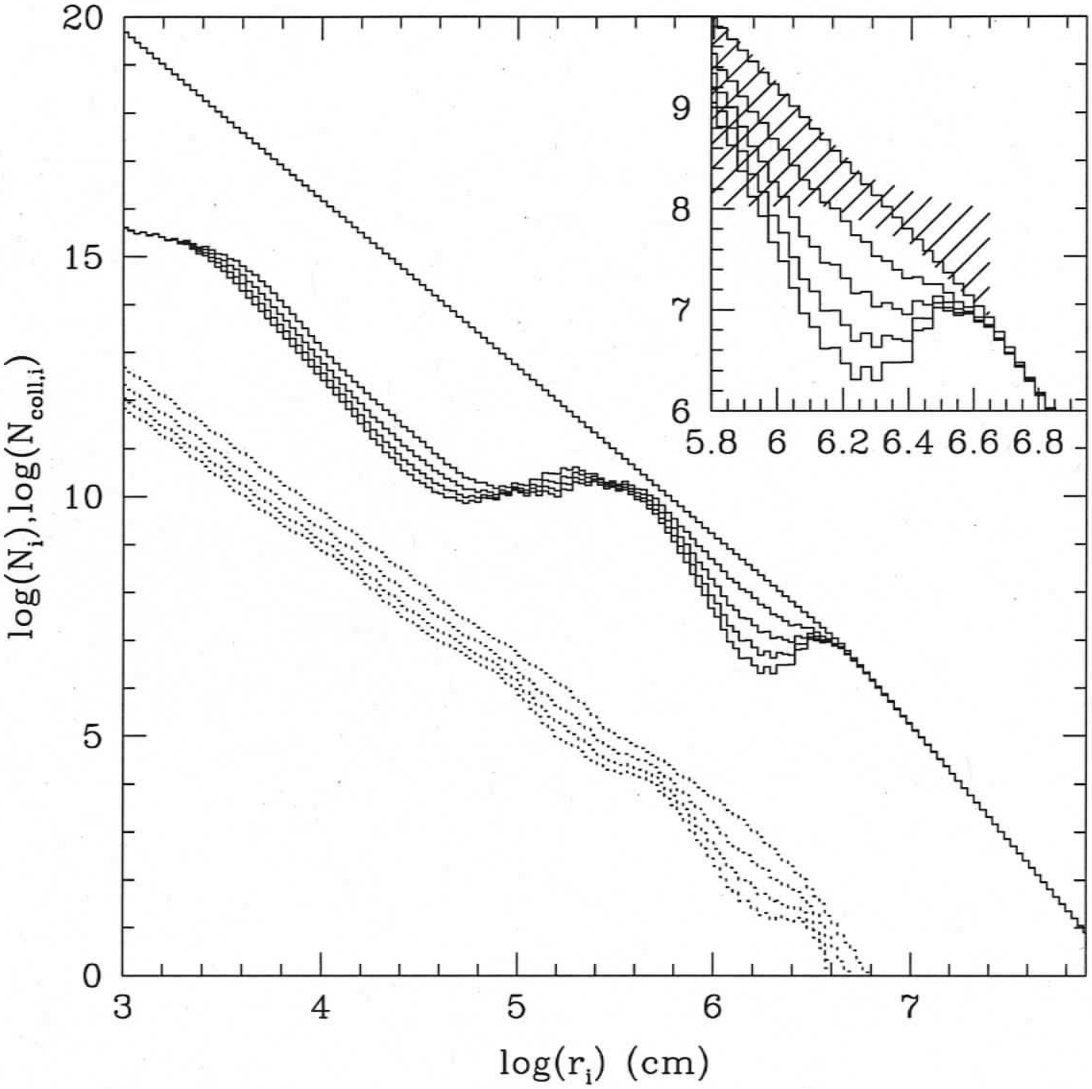

Figure 5.9: Results of simulation N2S3. Presented is same as in Figure 5.4. The dashed region in the inset, has been scaled vertically to match the initial size distribution.

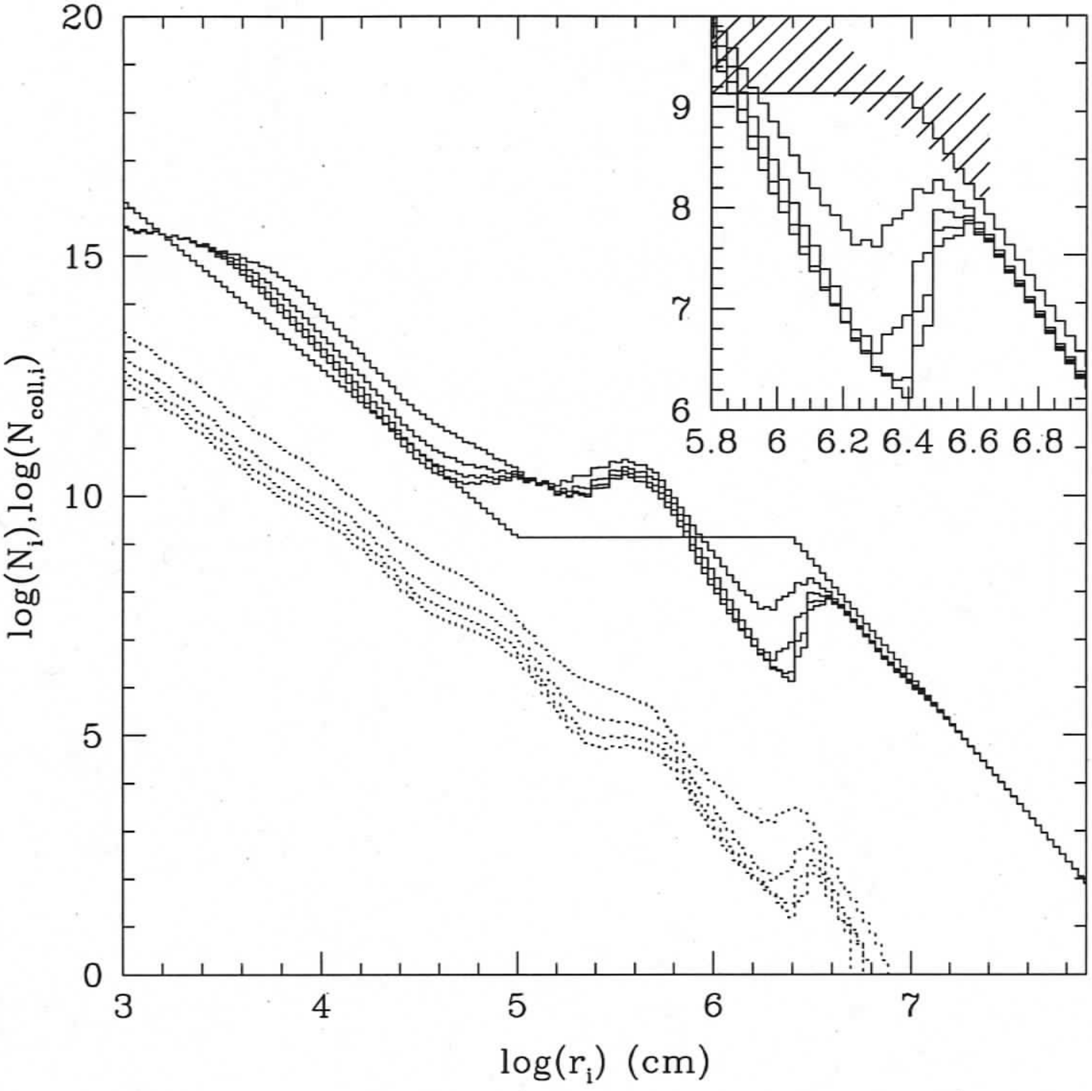

Figure 5.10: Results of simulation N3S1. Presented is same as in Figure 5.4. The dashed region in the inset, has been scaled vertically to match the initial size distribution.

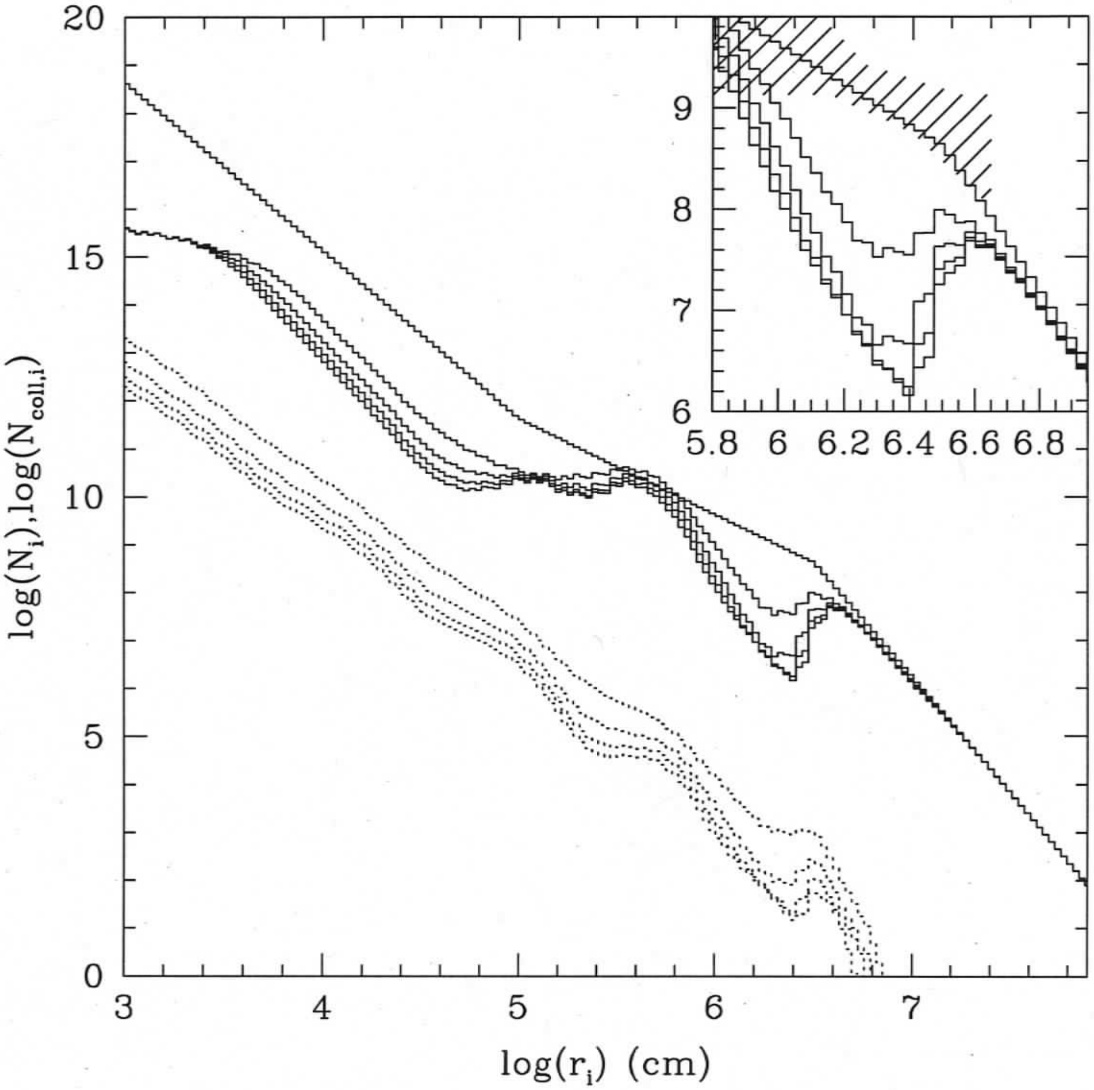

Figure 5.11: Results of simulation N3S2. Presented is same as in Figure 5.4. The dashed region in the inset, has been scaled vertically to match the initial size distribution.

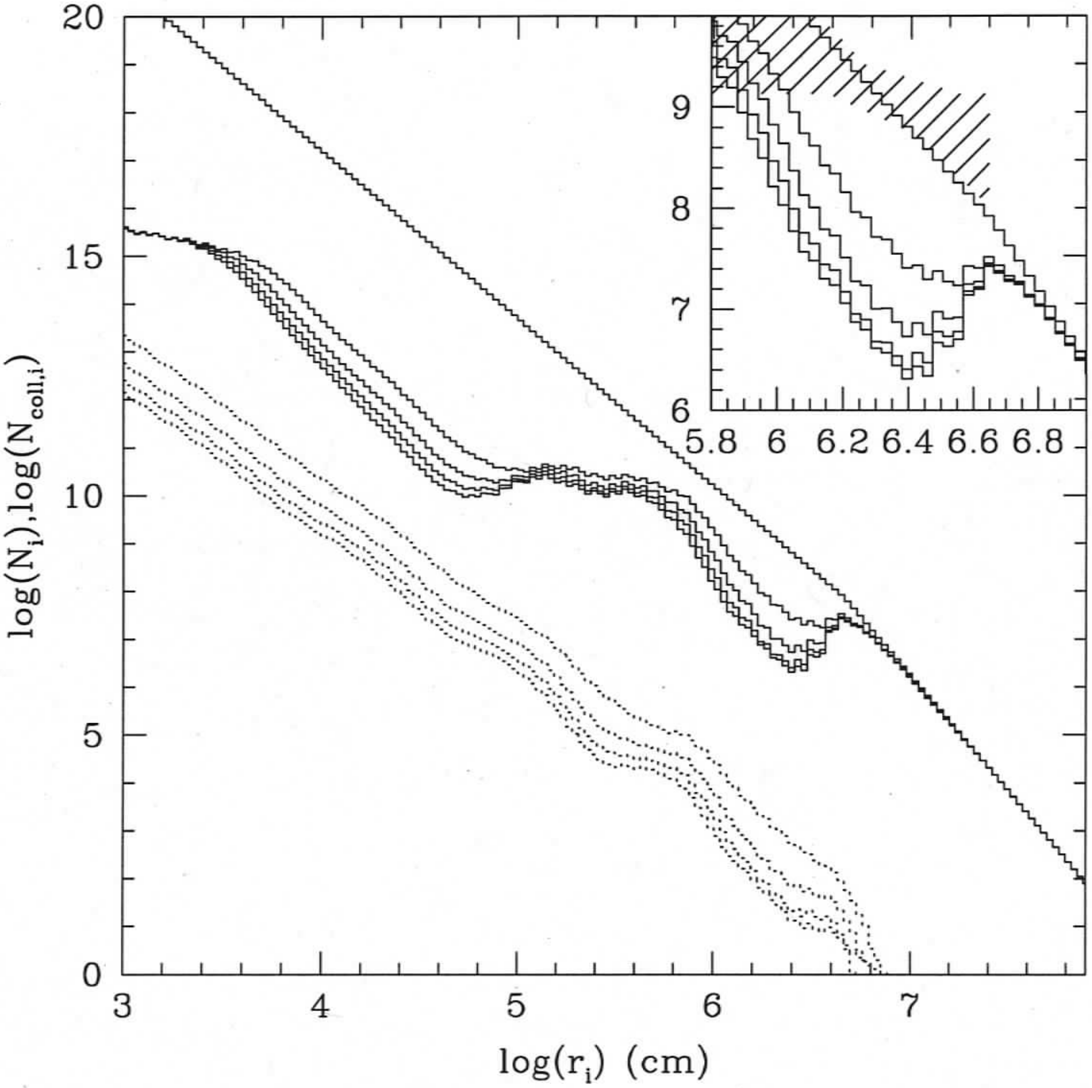

Figure 5.12: Results of simulation N3S3. Presented is same as in Figure 5.4. The dashed region in the inset, has been scaled vertically to match the initial size distribution.

Chapter 6

Conclusions and Future Work

In the previous chapters, we have described our efforts in determining the size distribution of the Kuiper belt. With observations sensitive to Kuiper belt objects (KBOs) with $m(R) \sim 21-27$ we have measured the luminosity function over that range, and have inferred from this, that the KBO size distribution is a power-law with slope $q_1 \sim 4.8$ for large objects, that breaks to a shallower slope $q_2 \sim 2$ for small objects, at break diameter $D_b \sim 60$ km, assuming 6% albedos.

Our findings have confirmed the existence of a break in the luminosity function and size distributions. We have developed a new functional representation of the KBO luminosity function that provides a direct comparison with the size distribution, and with this new form, have shown that the observed luminosity function is consistent with that produced from an underlying broken power-law size distribution. We have demonstrated that, for the observable KBOs, a state of collisional equilibrium has not been achieved, and conclude that the large object size distribution is a left over relic of the end of planetesimal accretion in the early Solar system. The observed slope is consistent with a short accretion time of a few 100 Myr.

We have found that the observed break diameter is too large to be consistent with accretion models that simulate planetesimal growth in the Kuiper belt region. Using a collisional evolution model, we have demonstrated that, for KBO densities similar to that observed, the observable size distribution would not evolve significantly on billion year timescales. We conclude that the large object break must have been created in a denser environment than in the modern Kuiper belt. This finding is in agreement with collisional evolution simulations which demonstrate that the primordial Kuiper belt must have been significantly denser for objects as large as Pluto to accrete in the age of the Solar system.

The observations we have made, have provided significant insight into the formation and subsequent collisional evolution of the Kuiper belt. Significant questions however, still remain:

- What is the size distribution of small KBOs? Can we improve the measurement of D_b and q_2, and at what size is collisional equilibrium reached?
- How different is the size distributions of the excited and cold populations, and are the size distributions of the different dynamical classes the same?
- What was the primordial Kuiper belt mass?
- How long did the enhanced collisional evolution occur before mass loss was complete?
- How strong are KBOs?

Future surveys should be designed with the first two items in mind, as these would provide strong constraint on accretion and dynamical models which attempt to explain the current state of the Kuiper belt. For instance, Neptune migration models, such as that from *Levison et al.* (2008) suggest that the excited population should exhibit a more evolved size distribution than the cold population. A confirmation of this would lend great strength to the believability of the Neptune migration scenarios. Improved measurements of the size distribution to ever smaller sizes will improve the constraints these observations have on the various processes that have molded and sculpted the Kuiper belt over the age of the Solar system.

All three properties, the initial Kuiper belt mass, length of collisional evolution, and KBO strength have an impact on the KBO size distribution. Substantial modeling work is required however, before the specific effects of each individual property can be understood, and before constraints on them can be made. Accretion, and collisional modeling in different plausible dynamical scenarios (Neptune migration, rogue planet scattering, etc.) should be performed to determine which, if any of these scenarios can produce the KBO size distribution we have observed.

Much work is required before we truly understand the full history and evolution of planetesimals in the outer Solar system. The outlook for future research of the Kuiper belt appears bright and prosperous, with many new realizations yet to be made.

Bibliography

Alard, C. (2000), Image subtraction using a space-varying kernel, *A&AS*, *144*, 363–370.

Allen, R. L., G. M. Bernstein, and R. Malhotra (2001), The Edge of the Solar System, *ApJ*, *549*, L241–L244, doi:10.1086/319165.

Allen, R. L., G. M. Bernstein, and R. Malhotra (2002), Observational Limits on a Distant Cold Kuiper Belt, *AJ*, *124*, 2949–2954, doi:10.1086/343773.

Arakawa, M., and D. Tomizuka (2004), Ice-silicate fractionation among icy bodies due to the difference of impact strength between ice and ice-silicate mixture, *Icarus*, *170*, 193–201, doi:10.1016/j.icarus.2004.02.009.

Astier, P., et al. (2006), The Supernova Legacy Survey: measurement of Ω_M, Ω_Λ and w from the first year data set, *A&A*, *447*, 31–48, doi:10.1051/0004-6361:20054185.

Benz, W., and E. Asphaug (1999), Catastrophic Disruptions Revisited, *Icarus*, *142*, 5–20, doi:10.1006/icar.1999.6204.

Bernstein, G. (2008), Minor planet center orbit data base, http://www.cfa.harvard.edu/iau/MPCORB.html.

Bernstein, G., and B. Khushalani (2000), Orbit Fitting and Uncertainties for Kuiper Belt Objects, *AJ*, *120*, 3323–3332, doi:10.1086/316868.

Bernstein, G. M., D. E. Trilling, R. L. Allen, M. E. Brown, M. Holman, and R. Malhotra (2004), The Size Distribution of Trans-Neptunian Bodies, *AJ*, *128*, 1364–1390, doi:10.1086/422919.

Bernstein, G. M., D. E. Trilling, R. L. Allen, M. E. Brown, M. Holman, and R. Malhotra (2006), Erratum: "The Size Distribution of Trans-Neptunian Bodies" AJ, 128, 1364 [2004]), *AJ*, *131*, 2364–2364, doi:10.1086/503194.

Bertin, E., Y. Mellier, M. Radovich, G. Missonnier, P. Didelon, and B. Morin (2002), The TERAPIX Pipeline, in *Astronomical Data Analysis Software and Systems XI*, *Astronomical Society of the Pacific Conference Series*, vol. 281, edited by D. A. Bohlender, D. Durand, and T. H. Handley, pp. 228–+.

Bertoldi, F., W. Altenhoff, A. Weiss, K. M. Menten, and C. Thum (2006), The trans-neptunian object UB_{313} is larger than Pluto, *Nature*, *439*, 563–564, doi: 10.1038/nature04494.

Bottke, W. F., D. D. Durda, D. Nesvorný, R. Jedicke, A. Morbidelli, D. Vokrouhlický, and H. Levison (2005), The fossilized size distribution of the main asteroid belt, *Icarus*, *175*, 111–140, doi:10.1016/j.icarus.2004.10.026.

Brown, M. E. (2001), The Inclination Distribution of the Kuiper Belt, *AJ*, *121*, 2804–2814, doi:10.1086/320391.

Brown, M. E., and M. Pan (2004), The Plane of the Kuiper Belt, *AJ*, *127*, 2418–2423, doi:10.1086/382515.

Brown, M. E., E. L. Schaller, H. G. Roe, D. L. Rabinowitz, and C. A. Trujillo (2006), Direct Measurement of the Size of 2003 UB313 from the Hubble Space Telescope, *ApJ*, *643*, L61–L63, doi:10.1086/504843.

Chiang, E. I., and M. E. Brown (1999), Keck Pencil-Beam Survey for Faint Kuiper Belt Objects, *AJ*, *118*, 1411–1422, doi:10.1086/301005.

Dell'Oro, A., F. Marzari, P. Paolicchi, and V. Vanzani (2001), Updated collisional probabilities of minor body populations, *A&A*, *366*, 1053–1060, doi:10.1051/0004-6361:20000492.

Dohnanyi, J. W. (1969), Collisional models of asteroids and their debris, *J. Geophys. Res.*, *74*, 2531–2554.

Elliot, J. L., et al. (2005), The Deep Ecliptic Survey: A Search for Kuiper Belt Objects and Centaurs. II. Dynamical Classification, the Kuiper Belt Plane, and the Core Population, *AJ*, *129*, 1117–1162, doi:10.1086/427395.

Fraser, W. C., and J. Kavelaars (2008a), A Derivation of the Luminosity Function of the Kuiper Belt from a Broken Power-Law Size Distribution, *Submitted to Icarus.*

Fraser, W. C., and J. Kavelaars (2008b), The Size Distribution of Kuiper belt objects for $D \gtrsim 10$ km., *Submitted to the Astronomical Journal.*

Fraser, W. C., J. J. Kavelaars, M. J. Holman, C. J. Pritchet, B. J. Gladman, T. Grav, R. L. Jones, J. Macwilliams, and J.-M. Petit (2008), The Kuiper belt luminosity function from $m_R = 21 to 26$, *Icarus*, *195*, 827–843, doi:10.1016/j.icarus.2008.01.014.

Fuentes, C. I., and M. J. Holman (2008), a SUBARU Archival Search for Faint Trans-Neptunian Objects, *AJ*, *136*, 83–97, doi:10.1088/0004-6256/136/1/83.

Gladman, B., and C. Chan (2006), Production of the Extended Scattered Disk by Rogue Planets, *ApJ*, *643*, L135–L138, doi:10.1086/505214.

Gladman, B., J. J. Kavelaars, P. D. Nicholson, T. J. Loredo, and J. A. Burns (1998), Pencil-Beam Surveys for Faint Trans-Neptunian Objects, *AJ*, *116*, 2042–2054, doi: 10.1086/300573.

Gladman, B., J. J. Kavelaars, J.-M. Petit, A. Morbidelli, M. J. Holman, and T. Loredo (2001), The Structure of the Kuiper Belt: Size Distribution and Radial Extent, *AJ*, *122*, 1051–1066, doi:10.1086/322080.

Gladman, B., B. G. Marsden, and C. Vanlaerhoven (2008), *Nomenclature in the Outer Solar System*, pp. 43–57, The Solar System Beyond Neptune.

Grundy, W. M., K. S. Noll, and D. C. Stephens (2005), Diverse albedos of small trans-neptunian objects, *Icarus*, *176*, 184–191, doi:10.1016/j.icarus.2005.01.007.

Gwyn, S. D. J. (2008), MegaPipe: The MegaCam Image Stacking Pipeline at the Canadian Astronomical Data Centre, *PASP*, *120*, 212–223, doi:10.1086/526794.

Hahn, J. M., and R. Malhotra (2005), Neptune's Migration into a Stirred-Up Kuiper Belt: A Detailed Comparison of Simulations to Observations, *AJ*, *130*, 2392–2414, doi:10.1086/452638.

Hainaut, O. R., and A. C. Delsanti (2002), Colors of Minor Bodies in the Outer Solar System. A statistical analysis, *A&A*, *389*, 641–664, doi:10.1051/0004-6361:20020431.

Hayashi, C. (1981), Structure of the Solar Nebula, Growth and Decay of Magnetic Fields and Effects of Magnetic and Turbulent Viscosities on the Nebula, *Progress of Theoretical Physics Supplement*, *70*, 35–53.

Holman, M. J., et al. (2004), Discovery of five irregular moons of Neptune, *Nature*, *430*, 865–867, doi:10.1038/nature02832.

Ida, S., J. Larwood, and A. Burkert (2000), Evidence for Early Stellar Encounters in the Orbital Distribution of Edgeworth-Kuiper Belt Objects, *ApJ*, *528*, 351–356, doi:10.1086/308179.

Jewitt, D., and J. Luu (1993), Discovery of the candidate Kuiper belt object 1992 QB1, *Nature*, *362*, 730–732, doi:10.1038/362730a0.

Jewitt, D., J. Luu, and C. Trujillo (1998), Large Kuiper Belt Objects: The Mauna Kea 8K CCD Survey, *AJ*, *115*, 2125–2135, doi:10.1086/300335.

Kavelaars, J., L. Jones, B. Gladman, J. W. Parker, and J.-M. Petit (2008), *The Orbital and Spatial Distribution of the Kuiper Belt*, pp. 59–69, The Solar System Beyond Neptune.

Kavelaars, J. J., et al. (2004), The discovery of faint irregular satellites of Uranus, *Icarus*, *169*, 474–481, doi:10.1016/j.icarus.2004.01.009.

Kenyon, S. J. (2002), Planet Formation in the Outer Solar System, *PASP*, *114*, 265–283.

Kenyon, S. J., and B. C. Bromley (2001), Gravitational Stirring in Planetary Debris Disks, *AJ*, *121*, 538–551, doi:10.1086/318019.

Kenyon, S. J., and B. C. Bromley (2004), The Size Distribution of Kuiper Belt Objects, *AJ*, *128*, 1916–1926, doi:10.1086/423697.

Kenyon, S. J., and J. X. Luu (1998), Accretion in the Early Kuiper Belt. I. Coagulation and Velocity Evolution, *AJ*, *115*, 2136–2160, doi:10.1086/300331.

Kotz, S., and N. Johnson (1983), *Encyclopedia of Statistical Sciences*, John Wiley and Sons Ltd.

Landolt, A. U. (1992), UBVRI photometric standard stars in the magnitude range 11.5-16.0 around the celestial equator, *AJ*, *104*, 340–371, doi:10.1086/116242.

Levison, H. F., and A. Morbidelli (2003), The formation of the Kuiper belt by the outward transport of bodies during Neptune's migration, *Nature*, *426*, 419–421.

Levison, H. F., A. Morbidelli, and L. Dones (2004), Sculpting the Kuiper Belt by a Stellar Encounter: Constraints from the Oort Cloud and Scattered Disk, *AJ*, *128*, 2553–2563, doi:10.1086/424616.

Levison, H. F., A. Morbidelli, C. Vanlaerhoven, R. Gomes, and K. Tsiganis (2008), Origin of the structure of the Kuiper belt during a dynamical instability in the orbits of Uranus and Neptune, *Icarus*, *196*, 258–273, doi:10.1016/j.icarus.2007.11.035.

Loredo, T. J. (2004), Accounting for Source Uncertainties in Analyses of Astronomical Survey Data, in *American Institute of Physics Conference Series*, *American Institute of Physics Conference Series*, vol. 735, edited by R. Fischer, R. Preuss, and U. V. Toussaint, pp. 195–206, doi:10.1063/1.1835214.

Magnier, E. A., and J.-C. Cuillandre (2004), The Elixir System: Data Characterization and Calibration at the Canada-France-Hawaii Telescope, *PASP*, *116*, 449–464, doi:10.1086/420756.

Malhotra, R. (1993), The Origin of Pluto's Peculiar Orbit, *Nature*, *365*, 819–+, doi: 10.1038/365819a0.

Meyer, M. R., et al. (2006), The Formation and Evolution of Planetary Systems: Placing Our Solar System in Context with Spitzer, *PASP*, *118*, 1690–1710, doi: 10.1086/510099.

Miyazaki, S., et al. (2002a), Subaru Prime Focus Camera – Suprime-Cam, *PASJ*, *54*, 833–853.

Miyazaki, S., et al. (2002b), Subaru Prime Focus Camera – Suprime-Cam, *PASJ*, *54*, 833–853.

Morbidelli, A., H. F. Levison, and R. Gomes (2008), *The Dynamical Structure of the Kuiper Belt and Its Primordial Origin*, pp. 275–292, The Solar System Beyond Neptune.

Newberry, M. V. (1991), Signal-to-noise considerations for sky-subtracted CCD data, *PASP*, *103*, 122–130.

O'Brien, D. P., and R. Greenberg (2003), Steady-state size distributions for collisional populations:analytical solution with size-dependent strength, *Icarus*, *164*, 334–345, doi:10.1016/S0019-1035(03)00145-3.

Ouchi, M., et al. (2004), Subaru Deep Survey. V. A Census of Lyman Break Galaxies at z˜=4 and 5 in the Subaru Deep Fields: Photometric Properties, *ApJ*, *611*, 660–684, doi:10.1086/422207.

Pan, M., and R. Sari (2005), Shaping the Kuiper belt size distribution by shattering large but strengthless bodies, *Icarus*, *173*, 342–348, doi: 10.1016/j.icarus.2004.09.004.

Petit, J.-M., M. J. Holman, B. J. Gladman, J. J. Kavelaars, H. Scholl, and T. J. Loredo (2006), The Kuiper Belt luminosity function from m_R= 22 to 25, *MNRAS*, *365*, 429–438, doi:10.1111/j.1365-2966.2005.09661.x.

Press, W. H. (2002), *Numerical recipes in C++ : the art of scientific computing*, Numerical recipes in C++ : the art of scientific computing by William H. Press. xxviii, 1,002 p. : ill. ; 26 cm. Includes bibliographical references and index. ISBN : 0521750334.

Pritchet, C. J. (2005), SNLS – The Supernova Legacy Survey, in *Observing Dark Energy*, *Astronomical Society of the Pacific Conference Series*, vol. 339, edited by S. C. Wolff and T. R. Lauer, pp. 60–+.

Safronov, V. S., and E. V. Zvjagina (1969), Relative Sizes of the Largest Bodies during the Accumulation of Planets, *Icarus*, *10*, 109–+.

Smith, J. A., et al. (2002), The u'g'r'i'z' Standard-Star System, *AJ*, *123*, 2121–2144, doi:10.1086/339311.

Stansberry, J., W. Grundy, M. Brown, D. Cruikshank, J. Spencer, D. Trilling, and J.-L. Margot (2007), Physical Properties of Kuiper Belt and Centaur Objects: Constraints from Spitzer Space Telescope, *ArXiv Astrophysics e-prints*.

Stern, S. A. (1995), Collisional Time Scales in the Kuiper Disk and Their Implications, *AJ*, *110*, 856–+, doi:10.1086/117568.

Stern, S. A. (1996), On the Collisional Environment, Accretion Time Scales, and Architecture of the Massive, Primordial Kuiper Belt., *AJ*, *112*, 1203–+, doi: 10.1086/118091.

Stern, S. A., and J. E. Colwell (1997a), Accretion in the Edgeworth-Kuiper Belt: Forming 100-1000 KM Radius Bodies at 30 AU and Beyond., *AJ*, *114*, 841–+, doi:10.1086/118518.

Stern, S. A., and J. E. Colwell (1997b), Collisional Erosion in the Primordial Edgeworth-Kuiper Belt and the Generation of the 30-50 AU Kuiper Gap, *ApJ*, *490*, 879–+, doi:10.1086/304912.

Stern, S. A., M. W. Buie, and L. M. Trafton (1997), HST High-Resolution Images and Maps of Pluto, *AJ*, *113*, 827–+, doi:10.1086/118304.

Stetson, P. B. (1989), Advanced school of astrophysics universidade de sao paolo.

Thommes, E. W., M. J. Duncan, and H. F. Levison (2002), The Formation of Uranus and Neptune among Jupiter and Saturn, *AJ*, *123*, 2862–2883, doi:10.1086/339975.

Tody, D. (1993), IRAF in the Nineties, in *Astronomical Data Analysis Software and Systems II, Astronomical Society of the Pacific Conference Series*, vol. 52, edited by R. J. Hanisch, R. J. V. Brissenden, and J. Barnes, pp. 173–+.

Tombaugh, C. W. (1946), The Search for the Ninth Planet, Pluto, *Leaflet of the Astronomical Society of the Pacific*, *5*, 73–+.

Trujillo, C. A., and M. E. Brown (2001), The Radial Distribution of the Kuiper Belt, *APJ*, *554*, L95–L98, doi:10.1086/320917.

Trujillo, C. A., D. C. Jewitt, and J. X. Luu (2001), Properties of the Trans-Neptunian Belt: Statistics from the Canada-France-Hawaii Telescope Survey, *AJ*, *122*, 457–473, doi:10.1086/321117.

Yagi, M., N. Kashikawa, M. Sekiguchi, M. Doi, N. Yasuda, K. Shimasaku, and S. Okamura (2002), Luminosity Functions of 10 Nearby Clusters of Galaxies. II. Analysis of the Luminosity Function, *AJ*, *123*, 87–99, doi:10.1086/324732.

Yoshida, F., and T. Nakamura (2007), Subaru Main Belt Asteroid Survey (SMBAS)—Size and color distributions of small main-belt asteroids, *Planet. Space Sci.*, *55*, 1113–1125, doi:10.1016/j.pss.2006.11.016.

Young, E. F., R. P. Binzel, and K. Crane (2001), A Two-Color Map of Pluto's Sub-Charon Hemisphere, *AJ*, *121*, 552–561, doi:10.1086/318008.

Appendix A

The Magnitude and Standard Filter Systems

The "magnitude", is an inverse logarithmic flux unit chosen to mimic the human eye's response to starlight. In this system, the magnitudes, m_1 and m_2 of two sources with fluxes, f_1 and f_2, are given by

$$m_2 - m_1 = 2.5 \log \left(\frac{f_1}{f_2} \right) . \tag{A.1}$$

As can be seen, an increase of 1 magnitude corresponds to a factor ~ 2.5 *decrease* in flux. Similarly, a factor 10 increase in flux corresponds to a decrease of 2.5 in magnitudes.

Various broadband filter-sets have been created in which a part of the spectrum of light (eg. visible, infrared) is broken up into smaller wave-length ranges. A modern example is the *ugri* filter-set, the throughput and filter widths of which are presented in Figure A.1. This filter-set has four filters, labeled, u, g, r, and i spanning the visible spectrum. Other filter systems exist, which have been developed for specific purposes or surveys eg. the Johnson UVBRI system (see *Landolt* 1992, and references therein) and the Sloan Digital Sky Survey *ugriz* filter-set (see *Smith et al.* 2002, and references therein).

To set a zeropoint flux, the magnitudes of the A0 type star Vega, as measured through all filters of a filter-set are set to zero. The magnitudes set with this reference are commonly referred to as "Vega-magnitudes" and is the type of magnitude used throughout this manuscript. Note: An alternate, and less commonly used magnitude exists called an AB-magnitude, in which magnitudes are calibrated to energy flux rather than apparent visual flux.

A bolometric magnitude is the magnitude of a source over the entire spectrum. Most quoted magnitudes however, are those measured over a specific wavelength range, or through a specific filter. For example, the magnitude of a source through the r-filter is denoted r, and is referred to as an "r-magnitude".

A source's i-j colour is denoted as $(i - j)$ and is the difference between the magnitudes of a source in the i and j filters. As no two filter-sets are exactly the same, conversions of magnitudes between filter-sets on different instruments, or conversions between different filter systems are necessitated. The conversions are usually of the linear form

$$i' = i + C(i - j) \tag{A.2}$$

where magnitudes i and j are in one filter-set, i' is in another, and C is the so-called colour-term, which is a constant that is a function of the wavelength dependent throughput of filter i' compared to that of filters i and j. In very rare circumstances is it necessary to have a quadratic magnitude conversion.

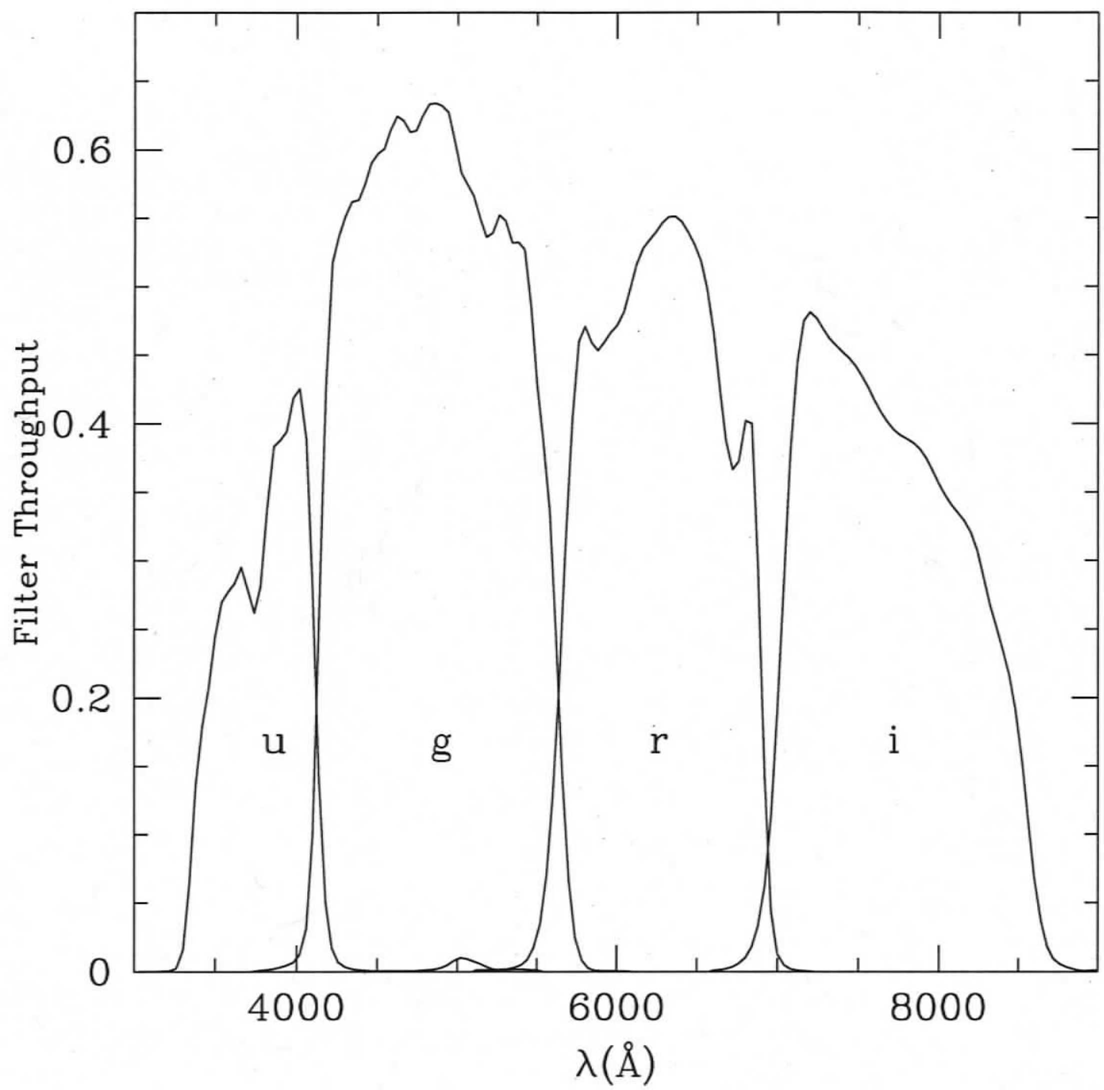

Figure A.1: The ugri filter set throughput from MegaCam on the Canada-France-Hawaii Telescope.

Appendix B

Apparent Rate of Motion Near Opposition

Here we derive the apparent motion of a planetesimal or Kuiper belt object (KBO) at opposition, on a circular orbit, in the ecliptic plane. The Kuiper belt object is located at heliocentric distance r and geocentric distance Δ both in AU, and has an inclination i. The KBO is at an elongation α and has an Observer-Sun-Target angle θ. Therefore, the target has a phase angle of $\pi - \theta - \alpha$. The Earth has a motion vector at an angle $\pi - \gamma$ from the line of sight to the KBO. The geometry of this scenario is presented in Figure B.1.

The rate of motion of the KBO is given by Kepler's third law, and can be broken up into directions parallel and perpendicular to the ecliptic (x and y-axes respectively). The rates of motion in radians per year of the KBO perpendicular to the line of sight are given by

$$\begin{aligned} \delta_{KBO,x} &= -\frac{2\pi}{r^{3/2}} \cos i \cos(\alpha + \theta) && \text{(B.1)} \\ \delta_{KBO,y} &= \frac{2\pi}{r^{3/2}} \sin i && \text{(B.2)} \end{aligned}$$

where we have used the relation that $\cos(\pi - \alpha - \theta) = -\cos(\alpha + \theta)$.

The motion of the Earth is by definition, in the ecliptic plane. Thus, the Earth has no rate of motion in the y-axis, and its rate of motion in the x-axis perpendicular to the line of sight is given by

$$\delta_{\oplus,x} = -2\pi \cos\alpha \tag{B.3}$$

where we have used the relations $\gamma + \alpha + \pi = 2\pi$ and $\cos(\pi - \alpha) = -\cos\alpha$. The motion of the Earth in the frame of the KBO and perpendicular to the ecliptic is in the opposite sense of the Earth's true motion, and is proportional to $1/\Delta$. The apparent rate of motion of the KBO - the rate of motion as observed on the sky - is the sum of the intrinsic rates of the KBO and the projected rate of the Earth, and is given by

$$\begin{aligned} \delta_{App,x} &= 2\pi \left(\frac{\cos\alpha}{\Delta} - \frac{\cos i \cos(\alpha + \theta)}{r^{3/2}} \right) & \text{(B.4)} \\ \delta_{App,y} &= \frac{2\pi}{r^{3/2}} \sin i. & \text{(B.5)} \end{aligned}$$

If we assuming the objects is at opposition, then $\cos\alpha + \theta = \cos\alpha = -1$. If we assume that the object is on a low inclination orbit, then its motion is dominantly in the x-direction. Finally, noting that 2π radians per year is equivalent to 147.94 arcseconds per hour, we see the *westward* rate of motion of the planetesimal is approximately given by

$$\delta_{App} \sim 148 \left[\frac{1}{\Delta} - \frac{1}{r^{3/2}} \right] \text{ '' hr}^{-1} \tag{B.6}$$

where r and Δ are in AU.

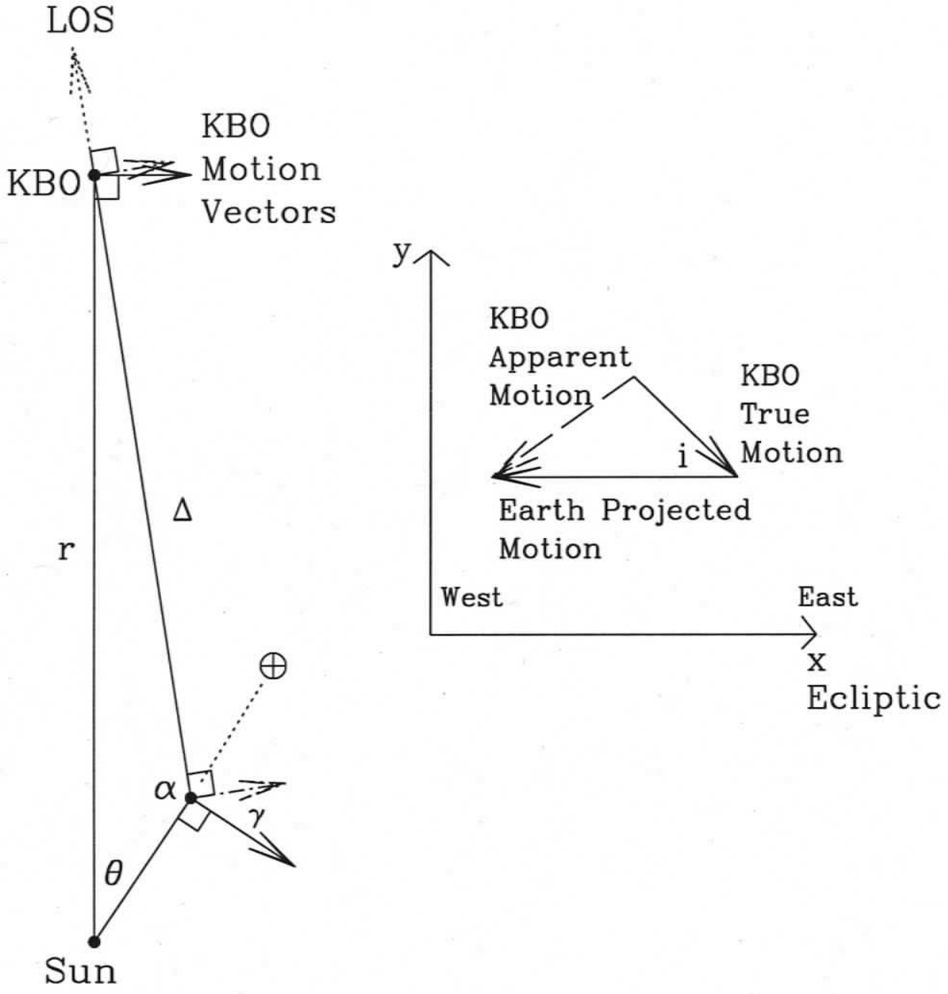

Figure B.1: Overview of the motion of the Earth and a KBO at heliocentric distance r and geocentric distance Δ. *Left:* Ecliptic overhead view. *Right:* View in plane of sky. α - KBO elongation angle. θ - Observer-Sun-KBO angle. LOS (dotted vector) - line of sight vector. True planetary velocity vectors (Earth and KBO) are represented by the solid arrows. Velocity vectors (Earth and KBO) perpendicular to line of sight are represented by dot-dashed arrows. Apparent KBO motion vector represented by dashed line.

Appendix C

Psfmatch3

Psfmatch3 is a subtraction routine that compensates for variations between the image quality of the template image and that of individual images. A description of the basic algorithm follows.

Consider an observed image O_{ij} (i, j refer to pixel row and column), and a suitably chosen reference image I_{ij}. We define an $n_k \times n_k$ convolution kernel K_{ij} such that the convolution $K * I$ provides some "best" (in a least-squares sense) estimator, $\tilde{O}$, of O; that is, the optimal kernel K is the one that minimizes $\sum_{i,j}(O_{ij} - \tilde{O}_{ij})^2$. Differentiating with respect to each kernel element K_{ij} yields a system of $M = n_k^2$ linear equations

$$\begin{pmatrix} \sum_{i,j} I_{i-1,j-1} I_{i-1,j-1} & \sum_{i,j} I_{i-2,j-1} I_{i-1,j-2} & \cdots & \cdots & \cdots \\ \cdots & \sum_{i,j} I_{i-2,j-2} I_{i-2,j-2} & \cdots & \cdots & \cdots \\ \cdots & \cdots & \cdots & \cdots & \cdots \\ \cdots & \cdots & \cdots & \sum_{i,j} I_{i-M+1,j-M+1} I_{i-M+1,j-M+1} & \cdots \\ \cdots & \cdots & \cdots & \cdots & \sum_{i,j} I_{i-M,j-M} I_{i-M,j-M} \end{pmatrix} * \begin{pmatrix} K_1 \\ K_2 \\ \cdots \\ K_{M-1} \\ K_M \end{pmatrix} = \begin{pmatrix} \sum_{i,j} O_{ij} I_{i-1,j-1} \\ \cdots \\ \cdots \\ \cdots \\ \cdots \end{pmatrix} \tag{C.1}$$

which can be solved for the n_k^2 kernel elements.

This basic procedure can be improved considerably by adding an extra term for sky differences, viz.

$$\tilde{O} = K * I + \Delta s,$$

where Δs is a constant denoting the difference in sky between the two images. Weighting by errors is easily included by minimizing $\frac{\sum_{i,j}(O_{ij}-\tilde{O}_{ij})^2}{\sigma_{ij}^2}$. Perhaps most important is allowing for spatial variations in the kernel (and sky background); this is accomplished simply by solving for polynomial coefficients representing the spatial variation of each kernel coefficient.

There are a number of features and advantages to this method of matching the point spread function on two images.

- The kernel K has arbitrary form; it does not need to be symmetric, and can handle PSF variations that may not always be handled by methods involving a basis set of functions to represent the kernel. The kernel can even be solved to perform deconvolution (which is the case when the reference image is erroneously chosen to have worse seeing), though this results in noise amplification.
- K is not necessarily normalized to unity; this automatically takes out transparency fluctuations.
- The method automatically removes small shifts (even spatially variable shifts) between two images.
- As noted above, the method can easily be adapted to include background differences, spatially variable backgrounds, and spatially variable kernels.

Appendix D

Background-limited Magnitude Measurement Uncertainty Derivation

The magnitude m of a source, as observed through a telescope and measured from a circular aperture of radius r, is given by

$$m = Z - 2.5 \log \left(\frac{n}{t} \right) \tag{D.1}$$

where n is the number of atomic data units (ADU) from the source in the aperture, t is the telescope exposure time, and Z is the telescope zeropoint. The number of source photons observed is given by $N = gn$ where g is the telescope gain in photons per ADU.

From Equation D.1, the uncertainty in the magnitude measure Δm, from an uncertainty in the source brightness Δn, is given by

$$\Delta m = \frac{2.5}{\ln 10} \frac{\Delta n}{t} 10^{\frac{m-Z}{2.5}}. \tag{D.2}$$

The uncertainty in a flux measurement of an astronomical source made by a charge-coupled device (CCD) is dominated by the photon-noise from the source, the photon-noise from the background, and the read-noise from the CCD electronics. Summing these effects in quadrature, the noise in the aperture in units of photons is

$$\Delta N = \left(S_{sky} t \pi r^2 + S_{source} t + \pi r^2 R_o^2\right)^{1/2} \tag{D.3}$$

where S_{sky} is the sky surface brightness in photons per pixel per second, S_{source} is the source flux in the aperture in photons per second, and R_o is the read-noise in photons. Thus, the noise in ADU is

$$\Delta n = \left(\frac{s_{sky} t \pi r^2}{g} + \frac{s_{source} t}{g} + \pi r^2 r_o^2\right)^{1/2} \tag{D.4}$$

where s_{sky} is the sky surface brightness in ADU per pixel per second, s_{source} is the source flux in ADU per second in the aperture, and r_o is the read-noise in ADU. Substituting this in Equation D.2, we find

$$\Delta m = \frac{2.5}{\ln 10} \left(\frac{s_{sky} \pi r^2 + s_{source}}{gt} + \frac{\pi r^2 r_o^2}{t^2}\right)^{1/2} 10^{\frac{m-Z}{2.5}}. \tag{D.5}$$

For background limited measurements, ie. where $s_{sky} \pi r^2 >> s_{source}$ and $s_{sky} t >> g r_o^2$, this simplifies to

$$\Delta m = \frac{2.5}{\ln 10} \sqrt{\frac{\pi r^2 s_{sky}}{gt}} 10^{\frac{m-Z}{2.5}}. \tag{D.6}$$

Appendix E

Field Divisions from *Trujillo et al.* (2001)

Table E.1: Field Details.

Field	R.A. (hrs.)	Ecliptic Latitude (^{o})	Area (Sq. ^{o})	# Objects	Efficiency
TE1G	8 - 9	-0.5 - 0.5	7.59	15	Good
TE1M	8 - 9	-0.5 - 0.5	3.3	4	Medium
TE2G	10 - 11	0	4.35	11	Good
TE3G	11 - 12.5	0	6.27	12	Good
TE3M	11 - 12.5	0	2.31	4	Medium
TE4G	~21-23	0	2.64	4	Good
TE4M	~21-23	0	2.97	3	Medium
TE5G	~23 - 1	0	0.66	0	Good
TE5M	~23 - 1	0	4.39	7	Medium

Table E.2: *Trujillo et al.* (2001) pointings included in each field division.

Field	Pointings
TE1G	476727o, 476728o, 476729o, 476848o, 476849o, 476850o, 476851o, 476852o, 476853o, 476854o, 476855o, 476856o, 476857o, 476858o, 476859o, 476984o, 476985o, 476986o, 476987o, 476988o, 476989o, 476990o, 476991o
TE1M	476717o, 476718o, 476719o, 476720o, 476721o, 476992o, 476993o, 476994o, 476995o, 476996o
TE2G	476885o, 476886o, 476887o, 476888o, 476889o, 476890o, 476891o, 476892o, 476893o, 476894o, 476895o, 476896o,476924o
TE3G	476758o, 476759o, 476760o, 476761o, 476762o, 476763o, 476764o, 476765o, 476766o,476767o, 476768o, 476769o,476795o, 476796o, 476797o, 527174o, 527305o, 527458o, 527461o
TE3M	476798o, 476799o, 527175o, 527306o, 527307o, 527459o, 527460o
TE4G	502047o, 502048o, 502049o, 502183o, 502184o, 502215o, 502217o, 502218o
TE4M	502050o, 502051o, 502052o, 502182o, 502185o, 502186o, 502214o, 502216o, 502374o
TE5G	502102o, 502139o
TE5M	502098o, 502099o, 502100o, 502101o, 502103o, 502136o, 502137o, 502138o, 502140o, 502248o, 502249o, 502250o, 502426o

Appendix F

Derivation of the Broken Power-law Luminosity Function assuming $dN/dr \propto r^{-c}$

As an approximation to the true Kuiper belt radial distribution, we assume that $R(r) \propto r^{-c}$ and $r_1 \le r \le r_2$. Making the substitution $\gamma = (1-c)/10$, and after collecting like terms, the coefficients of Eq. 3.11 become

$$a_1(m) = A\frac{r_2^{10(\gamma-\alpha_1)} - r_1^{10(\gamma-\alpha)}}{50\alpha(\gamma-\alpha)}10^{-\alpha K}, \tag{F.1}$$

$$b_1(m) \sim -A\frac{D_b^{5(\alpha_2-\alpha_1)}}{50\alpha_2\left(\gamma-\alpha_2\right)}r_1^{10(\gamma-\alpha_2)}10^{-K\alpha_2}, \tag{F.2}$$

$$b_2(m) \sim A\frac{r_2^{10(\gamma-\alpha_1)}}{50\alpha_1(\gamma-\alpha_1)}10^{-\alpha_1 K}, \tag{F.3}$$

$$b_3(m) \sim A\frac{(\alpha_2-\alpha_1)}{(\gamma-\alpha_1)\left(\gamma-\alpha_2\right)}\frac{D_B^{5(\gamma-\alpha_1)}}{50\gamma}10^{\gamma(m-K)} \tag{F.4}$$

$$c_1(m) = A\frac{r_2^{10\gamma} - r_1^{10\gamma}}{10\gamma}D_b^{-5\alpha_1}\left(\frac{\alpha_2-\alpha_1}{5\alpha_1\alpha_2}\right), \tag{F.5}$$

and

$$c_2 = A\frac{r_2^{10(\gamma-\alpha_2)} - r_1^{50(\gamma-\alpha_2)}}{50\alpha_2(\gamma-\alpha_2)} D_b^{5(\alpha_2-\alpha_1)} 10^{-\alpha_2 K}. \tag{F.6}$$

where $\gamma \neq \alpha_1$, $\gamma \neq \alpha_2$, $\alpha_1 \neq 0$, and $\alpha_2 \neq 0$, or equivalently $3 - 2q_1 - c \neq 0$, $3 - 2q_2 - c \neq 0$, $1 - q_1 \neq 0$, and $1 - q_2 \neq 0$ and we have dropped the negligible terms from the coefficients.